INVERTED BASE PAVEMENT STRUCTURES

A Thesis
Presented to
The Academic Faculty

by

Douglas D. Cortes Avellaneda

In Partial Fulfillment
of the Requirements for the Degree of
Doctor in Philosophy in the
School of Civil and Environmental Engineering

Georgia Institute of Technology
December 2010

INVERTED BASE PAVEMENT STRUCTURES

Approved by:

Dr. J. Carlos Santamarina, Advisor
School of Civil and Environmental Engineering
Georgia Institute of Technology

Dr. David Frost
School of Civil and Environmental Engineering
Georgia Institute of Technology

Dr. Susan Burns
School of Civil and Environmental Engineering
Georgia Institute of Technology

Dr. Guillermo Godsztein
School of Mathematics
Georgia Institute of Technology

Dr. Shane Buchanan
Vulcan Materials Company

Dr. Paul Mayne
School of Civil and Environmental Engineering
Georgia Institute of Technology

Date Approved:

A German y Maria
la semilla y la tierra

ACKNOWLEDGEMENTS

The culmination of this work is a testament to the love and dedication of my parents German and Maria, the support of my siblings Lynda, Glen and Howard, and the resilience that defines my extended family's character. Theirs is the light that shines through the darkest moments and the compass of my steps.

The contributions of my thesis committee have enriched this manuscript. To Dr. Burns, Dr. Buchannan, Dr. Frost, Dr. Goldsztein, and Dr. Mayne my most sincere appreciation. I would like to especially acknowledge the role of my advisor Dr. Santamarina. From the time I joined his research group as an undergraduate, Carlos has always guided me with implacable patience. I feel privileged to have spent these years learning from such an exceptional scientist, lecturer, and human being. His mentorship has permanently influenced my life.

Thanks to Brett, Sami and Jaime, the good friends with whom I sailed into this journey, and my friends in the geosystems group from whom I have learned so many valuable lessons. My gratitude to Tae-Sup, Hosung, Maria Cristina, Pierre, Veronica, Nico, Jong-Won, Jaewon, Minsu and Ba-Te. To Andy and Mike, thanks for their collaboration in the development of devices. Thanks also to the Colombian community at Georgia Tech for so many wonderful moments. My appreciation to Joan, Johanna, Paola, Lina, Palomita, Yuley, Manuel, Will, Ricardo, Jaime, Alejandro, Mario-Camilo, Lucio, Fernando, Cesar, Seunghee, and Sheng.

Finally, I would like to humbly express my immense gratitude and love to Sara, the ballerina whose motion harmoniously turned harsh winters into appeasing springs.

TABLE OF CONTENTS

LIST OF TABLES

LIST OF FIGURES

SUMMARY

An inverted base pavement is a new pavement structure that consists of an unbound aggregate base between a stiff cement-treated foundation layer and a thin asphalt cover. Unlike conventional pavements which rely on upper stiff layers to bear and spread traffic loads, the unbound aggregate inter-layer in an inverted base pavement plays a major role in the mechanical response of the pavement structure. Traditional empirical pavement design methods rely on rules developed through long-term experience with conventional flexible or rigid pavement structures. The boundaries imposed on the unbound aggregate base in an inverted pavement structure change radically from those in conventional pavements. Therefore, current empirically derived design methods are unsuitable for the analysis of inverted base pavements. The present work documents a comprehensive experimental study on a full-scale inverted pavement test section built near LaGrange, Georgia. A detailed description of the mechanical behavior of the test section before, during and after construction provides critically needed understanding of the internal behavior and macro-scale performance of this pavement structure. Given the critical role of the unbound aggregate base and its proximity to the surface, a new field test was developed to characterize the stress-dependent stiffness of the as-built layer. A complementary numerical study that incorporates state-of-the-art concepts in constitutive modeling of unbound aggregates is used to analyze experimental results and to develop preliminary guidelines for inverted base pavement design. Simulation results show that an inverted pavement can deliver superior rutting resistance compared to a conventional flexible pavement structure with the same fatigue life. Furthermore, results show that an

inverted base pavement structure can exceed the structural capacity of conventional flexible pavement designs for three typical road types both in rutting and fatigue while saving up to 40% of the initial construction costs.

CHAPTER 1

INTRODUCTION

1.1. Motivation and Significance

The U.S. public road system comprises over 4 million miles of roads and highways (FHWA 2009). Georgia has 88000 miles of paved roads, 99% of which are flexible pavement structures. Commissioning new roads and retrofitting existing ones are multi-million dollar decisions. The aggregate base in both rigid and flexible pavement structures is considered a weak layer that needs to be protected from service traffic induced stresses by either a thick Portland cement concrete layer or a thick asphalt concrete layer.

Inverted base pavements consist of an unbound aggregate base confined by a stiff cement-treated foundation layer and a thin asphalt cover. The thin asphalt cover and the proximity of the unbound aggregate layer to the surface make the granular layer a critical structural element. Unlike conventional pavement sections which rely on the upper stiff layers to bear and spread the traffic loads, the unbound aggregate inter-layer in an inverted base pavement plays a major role in the mechanical response of the pavement structure. Success stories in South Africa and test sections in the U.S.A. confirm the viability of this alternative pavement structure (Barksdale 1984; Tutumluer 1995; Tutumluer and Barksdale 1995; Rasoulian et al. 2000; Rasoulian et al. 2001; Terrell 2002; Terrell et al. 2003; Titi et al. 2003).

Traditional empirical pavement design methods rely on rules developed through long-term experience. The application of empirical design methods is limited to the type

of pavement structure, materials, construction practices, and site dependent environmental conditions considered to develop the design procedure. The boundaries imposed on the unbound aggregate base in an inverted pavement structure change radically from those of either flexible or rigid pavements. Therefore, empirically derived design methods used for conventional flexible pavement structures are unsuitable for the analysis of inverted base pavements. In order to overcome empirical design limitations, research efforts have focused on the development of mechanistic design techniques in which the pavement section is treated as a structure, and its mechanical behavior is evaluated using analytical/numerical tools from mechanics.

Mechanistic pavement analysis requires a profound understanding of the behavior of the materials in the pavement structure. In this context, the resilient response of unbound aggregate bases, sub-bases, and subgrade is a key input property in mechanistic-empirical pavement design procedures, i.e., NCHRP 1-37A. Inaccuracies in the determination of the resilient behavior contribute to erroneous predictions of overall pavement response (Witczak 2004).

Unbound aggregates exhibit a stress dependent non-linear elastic response under cyclic loading (Morgan 1966; Monismith et al. 1967; Hicks and Monismith 1971; Allen and Thompson 1974; Barksdale 1984; Adu-Osei 2000; Lekarp et al. 2000). In an inverted pavement section, the thinner asphalt concrete layer combined with the stiffer cement treated foundation leads to the development of large stresses within the unbound aggregate under service loading. Larger fluctuations in the state of stress exacerbate the non-linear response of the unbound aggregate base in an inverted structure. Therefore, the mechanical response of the unbound aggregate base, both under construction and during

its service life, must be thoroughly characterized and clearly understood before predictive inverted pavement design methods can emerge.

The present work documents a comprehensive experimental, analytical and numerical study centered on a full-scale inverted pavement test section built in the state of Georgia. A detailed description of the mechanical behavior of the test section before, during and after construction provides critically needed information to enhance our understanding of the internal behavior and macro-scale performance of this pavement system. A complementary analytical and numerical study that incorporates the state-of-the-art in constitutive modeling of unbound aggregates is used to extrapolate experimental results and to develop preliminary guidelines for inverted base pavement design.

1.2. Thesis Organization

The study presented in this dissertation centers on the fundamental understanding of unbound aggregate bases in the context of inverted base pavement structures. The information is organized as follows:

Chapter 2 documents the full-size field study of an inverted base pavement test section constructed in LaGrange, Georgia. This is the second of its kind in the U.S.A. and the first one to be fully tested, documented, and analyzed. Members of the Particulate Media Research Laboratory participated in the extensive field test program.

Chapter 3 explores the limitations of available laboratory and field unbound aggregate base stiffness characterization methods and presents a novel test alternative for as-built characterization.

Chapter 4 offers a comprehensive review of unbound aggregate behavior and available constitutive models, addresses model selection in detail, and implements a calibration method based on robust physical principles and concepts from information theory.

Chapter 5 documents the numerical implementation of the selected constitutive model, explores the effect of modeling assumptions and presents the predicted mechanical response of an inverted base pavement structure. Dr. H.S. Shin helped implement the model in ABAQUS.

Chapter 6 summarizes a simulation study of inverted base pavement structures and recommends preliminary guidelines for design.

Chapter 7 summarizes salient conclusions and identifies potential areas for future research.

The chapters in the thesis are written as self-contained documents; therefore, the reader will find some repetition particularly among the introductory sections for the different chapters.

CHAPTER 2

THE LAGRANGE CASE STUDY

2.1. Introduction

The need for improved road performance, optimal use of resources, superior cost efficiency, budget constraints, and energy efficiency prompt the analysis of alternative pavement structures. The use of inverted base pavements in the U.S.A. has been hindered by the lack of field experiments and related research required to investigate the mechanical response of this pavement structure under local conditions, construction practices, and required quality control and performance. A full-scale field study was conducted in LaGrange, Georgia, with support of the Georgia Department of Transportation (GDOT). The laboratory and field studies conducted as part of this pilot project advance both the current state of knowledge on the behavior of inverted base pavement systems and the state of the practice in terms of construction processes and quality assurance.

The investigation was designed to gather detailed information before, during and after the construction of the inverted base pavement test section in order to gain critically needed understanding of the internal behavior and macro-scale performance of this pavement structure through complementary analytical and numerical studies. The results of this investigation will help identify the potential benefits and limitations of inverted base pavement structures, and will allow for the calibration of numerical models that can later be used for optimal design.

2.2. Project Description

The test section is part of an industrial parkway intended to serve the growing car manufacturing industry in south-west Georgia. The inverted base pavement test section is a two-lane 1036m long stretch of the south LaGrange loop. It was designed to sustain an initial one-way annual average traffic of 7000 vehicles per day projected to grow to 11700 by the end of its service life. Truck traffic was estimated at 7% and consisted of 3% multi-unit (truck tractor semi-trailers and full trailer combination vehicles) and 4% single-unit (two and three axle trucks and busses having six tires). Pavement structures selected to satisfy the projected traffic demand are presented in figure 2.1. GDOT designed the rigid pavement following the AASHTO (1972) interim pavement design guide; the inverted base pavement was designed using empirical guidelines from the South African experience. The structural comparison between the conventional rigid pavement and the inverted section could not be made a priori.

The test section cuts across residual soils from the Georgia Piedmont geologic formation. Figure 2.2 shows the original topography and the built longitudinal cross section. Material removed from the cut sections was transported and compacted in the two fill sections. Construction of the subgrade took place from January 7 to February 19, 2008. The upper 0.15m of the subgrade were stabilized by mixing in crushed stone (figure 2.3) and compacting. Stabilization work began on July 23, 2008 and was completed on July 30, 2008.

The construction of the cement-treated base took place between July 30 and August 5, 2008. Cement and aggregate were mixed in a pug mill and hauled 3.2km to the construction site. Spreading and compaction operations started at station 280+00 and

moved along the westbound lane towards station 314+00. The eastbound lane was constructed on the way back, from station 314+00 towards station 280+00. Construction issues near the bridge approach (station 314+00) lead to a short gap in the test section near the bridge. The mix contained 4% cement by weight and was compacted to 98% of Proctor. Progress was monitored from the time the cement treated aggregate left the pug mill until the final bituminous seal coat was placed (figure 2.4).

The placement and compaction of the unbound aggregate base started August 11, 2008 and lasted 18 days. The asphalt concrete layer was placed in two lifts. The first was a 19mm NMS 0.05m thick layer built shortly after the completion of the unbound aggregate base in October 16, 2008. The riding surface was a 12.5mm NMS, 0.04m thick added on April 18, 2009.

2.3. Laboratory and Field Material Characterization

The layers were carefully monitored during construction, including extensive material characterization in the laboratory and in the field.

2.3.1. Subgrade

Thirty five subgrade samples were collected from the test section and used to determine grain size distribution, specific surface, liquid limit, bulk density, water content, complex permittivity, electrical conductivity, suction, and P-wave velocity in the laboratory. The field characterization of the subgrade included dynamic cone penetrometer, helical probe test and surface waves. Test results are summarized in table 2.1, the main findings follow:

- The mean grain size distribution is characterized by D_{10}≈0.2mm, D_{50}≈0.5mm, coefficient of uniformity C_u≈6, and coefficient of curvature C_c≈1.3, which are characteristic of well graded granular materials. The fraction of fines (d<75μm) ranged from 1% (at station 299+00) to 36% (at station 306+00). The high specific surface of the fine fraction suggested the presence of clay minerals (7 to 30 $m^2 \cdot g^{-1}$), and susceptibility to changes in water content and/or pore fluid chemistry.
- The recovered in-situ water content data fall within the range of optimum water content established by Proctor compaction tests carried out by GDOT. Measured liquid limit values are plotted in figure 2.5 for reference.
- The mean laboratory-measured bulk density was 1700kg·m^{-3} while GDOT field-measured density averaged 1900kg·m^{-3}. The subgrade bulk density is intimately related to its grain size distribution and particle shape. Variations in density also reflect the relative proportions and specific gravities of the minerals that make the solid particles, the porosity of the granular packing, and the water content at the time the measurement is made. The bulk density results can be used in conjunction with water content data to calculate the dry density of the material; estimated porosity values are plotted in figure 2.6.
- Complex permittivity was monitored over the frequency range from 0.2 to 13GHz. Data reported in table 2.1 correspond to a frequency of 0.5GHz. At high frequencies, permittivity is determined by the polarizability of free water; thus, the real permittivity of the wet soil increases with increasing water content. Outlier water content data at stations 298+00 and 299+00 corroborate this observation.

- The measured electrical conductivity values lay in the range from 0.004 to 0.06 $S \cdot m^{-1}$. Since conductivity through the mineral itself is comparatively low (kaolinite: $3.1 \times 10^{-8} S \cdot m^{-1}$; quartz: $5 \times 10^{-15} S \cdot m^{-1}$), the electrical conductivity of the tested soil samples is controlled by the pore fluid. The conductivity of the electrolyte varies with the concentration and mobility of electrical charges within the material (electrons, ions, polar molecules). However, conductivity is also enhanced by surface conduction which becomes significant in high specific surface soils (Revil and Glover 1997).
- Total suction data gathered at the in-situ water content fall between 200 and 1500kPa. Similar results are observed in the matric and osmotic suction measurements. Even higher suctions are anticipated at lower water contents under dry climate conditions. In any case, the measured suction levels anticipate a high moisture-dependent response of the subgrade.
- The P-wave velocity in unsaturated sediments is practically unaffected by the bulk stiffness of the fluid when the degree of saturation S≤95%. Instead, it reflects the stiffness of the soil skeleton which is in part controlled by capillary forces, i.e. suction (Santamarina et al. 2001). Measured P-wave velocities for the subgrade are in the range from 300 to 800 $m \cdot s^{-1}$, in agreement with the high measured suction values, which suggest that capillarity controls the subgrade stiffness. It should be noted that only samples that satisfied the test geometrical constraints where used to determine V_p. Since the soil samples that fulfilled this requirement where for the most part very well compacted blocks, the measurement is biased to stiffer values and does not necessarily represent the average stiffness of the subgrade.

- The field-measured surface wave velocities range from V_R = 150 to 200m·s^{-1} (figure 2.7).
- The measured helical probe torque and dynamic cone penetration resistance are positively correlated to both the total suction and the dry density; no evident correlation with bulk density or porosity was observed.
- An overall increase in surface wave velocity was observed in the stabilized subgrade as evidenced by data plotted in figure 2.7. The properties of the stabilized layer are summarized in table 2.2.

2.3.2. Cement-Treated Base

The off-site mixing, transport, spreading, and compaction of the cement-treated base were carefully monitored to assess hydration prior to compaction. Construction times are summarized in figure 2.4. Electrical properties of curing cementitious materials vary as a function of hydration, pore fluid composition, moisture, and temperature (Monfore 1968; Christensen et al. 1994; Fam and Santamarina 1996; McCarter 1996; McCarter et al. 1996; Wang et al. 2003; Rajabipour and Weiss 2007). As the cement paste cures in a mortar mixture there is a reduction in the ionic concentration of the pore fluid which leads to measurable changes in electrical resistivity. Therefore, electrical resistivity data can be used to assess the curing evolution of Portland cement mixtures. Curing of the compacted material was monitored using an electrical resistivity probe developed as part of this study. Different locations near the spreader were selected and tested in order to assess spatial variability and to detect heterogeneities. Results show no significant resistivity difference from location to location, suggesting homogeneity in the construction process. After collection of spatial variability data, the electrical resistivity

monitoring equipment was fixed at a given location to monitor the time evolution of electrical resistance with time, which can be used as an index of curing progress. Resistivity measurements started approximately 20 to 30 minutes after the cement was first exposed to water in the mixer. Field data show noticeable changes in conductivity starting at 100min (figure 2.8).

Characterization of the hardened cement-treated base properties was done on 7-day cores recovered from the site and tested for laboratory P-wave velocity and compressive strength; a summary of results is presented in table 2.3. A primary concern with the construction of the inverted base pavement structure is the mechanical response of the cement-treated base during the compaction of the unbound layer above and its long-term integrity. Copper wire loops were installed within the cement-treated base surface at selected locations. A 6.35mm thick groove was cut 12.7mm into the sub-base as shown in figure 2.9. Then, a thin polyurethane coated copper wire d= 0.3mm was placed in the grove and bonded to the sub-base using mortar mix. The resistance between the two ends was measured immediately after the installation of the wire to verify its integrity. The resistance at each of the three instrumented stations was measured following the construction of the unbound aggregate base; no changes from the pre-construction values were observed. These results show that the cement-treated base sustained no significant damage during the compaction of the unbound aggregate and the asphalt concrete layers. This was later confirmed in a forensic study through visual inspection.

2.3.3. Unbound Aggregate Base

The unbound aggregate base is the central component of the inverted base pavement structure. Therefore, special attention was devoted to identify changes in the aggregate base properties caused by compaction over the stiff cement treated base. We recovered aggregate samples pre and post compaction at three locations to determine grain size distribution in an effort to establish if crushing was taking place during compaction. Findings of the gradation tests are summarized in figure 2.10. Overall the data remain inconclusive as to the extent and significance of particle crushing.

The development of inherent anisotropy in the unbound aggregate layer as a result of compaction induced particle alignment was assessed via a forensic study. Trenches were dug through the asphalt layer uncovering the unbound aggregate and allowing us to take a look inside the unbound aggregate base and photograph the grain skeleton. Digital image analysis results presented in figure 2.11 show that particles preferentially align with their major axis parallel to the horizontal plane. Note that only the coarser visible particles are considered in this analysis.

The unbound aggregate non-linear stiffness-stress response is critical to the mechanical response of an inverted pavement structure. The as-built unloaded stiffness of the unbound aggregate base was determined using spectral analysis of surface waves (SASW) prior to the construction of the asphalt concrete layer (figure 2.7). The stiffness-stress relationship of the unbound aggregate is determined using a novel laboratory and field procedure (details are presented in chapter 3). Results of the stiffness-stress characterization under zero-lateral-strain loading indicate that the relationship between

the resilient modulus in the vertical E_{Rz} and horizontal E_{Rh} directions and the mean stress are given by:

$$E_{Rh} = 71.3MPa\left(\frac{p}{1kPa}\right)^{0.36} \quad ; \quad E_{Rz} = 102MPa\left(\frac{p}{1kPa}\right)^{0.36} \qquad 2.1$$

Unbound aggregate test results are summarized in table 2.4.

2.3.4. Asphalt Concrete

The characterization of the asphalt layer focused on the determination of elastic parameters, namely the elastic modulus and the Poisson's ratio. This was accomplished through field measurements of surface waves and laboratory P-wave velocity measurements in samples recovered during the forensic investigation. Characterization test results are summarized in table 2.5.

2.4. Discussion

Dynamic cone penetration data can be used in conjunction with density, liquid limit, and water content to estimate the resilient modulus of the subgrade; for example:

$$E_R = a_o (PR)^{a_1}\left[\gamma_{dry}^{a_2} + \left(\frac{LL}{w_c}\right)^{a_3}\right] \qquad 2.2$$

where PR is the dynamic cone penetration rate, γ_{dry} is the dry unit weight, LL is the liquid limit, w_c is the water content, and a_i are fitting parameters. Resilient modulus data estimated based on this correlation developed by George and Uddin (2000) yield a mean value E_R= 250MPa with a standard deviation of 100MPa. Surface wave velocity data are

used to estimate the constrained modulus using theory of elasticity and assuming isotropic response:

$$M \approx 2\rho\left(\frac{V_R}{0.9}\right)^2 \frac{(1-\nu)}{(1-2\nu)} \qquad 2.3$$

Measured bulk densities ρ and field velocity V_R data are used to calculate the constrained modulus M for the different layers (Figure 2.12). Poisson's ratio v was assumed to be 0.2 for the unbound layers, 0.25 for the cement-treated base and 0.3 for the asphalt concrete layer (confirmed with V_p and V_R data). The stiffness profile of the as-built pavement structure (without load) range between 30000MPa at the asphalt concrete and 140MPa at the subgrade.

2.5. Conclusions

The average measured specific surface and coefficient of uniformity of the subgrade at LaGrange indicate that its mechanical behavior is strongly influenced by electrical interactions and capillarity; therefore, it is susceptible to changes in water content and pore fluid chemistry. The measured suction values indicate strong capillarity, i.e., high equivalent effective stress. This explains the high P-wave velocity values measured as part of this study.

The as-built inverted base pavement stiffness profile exhibits pronounced contrast among successive layers; 30000MPa at the asphalt concrete, 500MPa for the unbound aggregate base (unloaded), 22000MPa for the cement-treated base, and 150MPa for the compacted subgrade. However, the unbound aggregate base stiffness is a non-linear function of the state of stresses. The stiffness-stress relationship has been determined

based on P-wave velocity measurements in a zero-lateral-strain cell, and shows a power law dependency between stiffness and stress.

The off-site mixing, transport, spreading, and compaction of the cement-treated base resulted in a homogeneously compacted layer. No early settling of the cement mixture was observed. The 7-day cured cement-treated base withstood compaction of the overlaying layers without cracking under the loading imposed by heavy equipment and construction operations.

Pre and post compaction gradation test results do not offer a clear assessment of the extent and significance of particle crushing in the unbound aggregate layer during compaction over the stiff cement-treated base. Digital image analysis confirmed particle-shape/compaction induced anisotropy in the as-built unbound aggregate base. Yet, the results of laboratory non-linear stiffness stress response show that stiffness anisotropy is primarily caused by the anisotropic state of stresses and that there is a unique stiffness-stress relationship in the directions of principal stresses. Therefore, while there is evidence that suggest inherent anisotropy caused by preferential particle alignment, stiffness anisotropy is primarily controlled by stress anisotropy.

Table 2.1 Subgrade characterization

Parameter		Parameter	
Coefficient of Uniformity C_u [ ]	6	Degree of Saturation S [ ]	0.3 ~ 0.9
Coefficient of Curvature C_c [ ]	1.3	Bulk Density ρ_{bulk} [kg·m^{-3}]	1700
Fraction smaller than 75μm [ ]	0.012 ~ 0.36	Dry Density ρ_{dry} [kg·m^{-3}]	1540
D_{10} [mm]	0.09 ~ 0.25	Porosity n [ ]	0.3 ~ 0.5
D_{30} [mm]	0.25 ~ 0.7	Complex Permittivity κ' [ ]	5 ~ 35
D_{60} [mm]	0.27 ~ 1.75	Electrical Conductivity σ_{DC} [s·m^{-1}]	0.004 ~ 0.06
Specific Surface S_s [m^2·g^{-1}]	7 ~ 30	Total Suction h_T [kPa]	200 ~ 1500
Liquid Limit LL [%]	50 ~ 100	Matric Suction h_M [kPa]	50 ~ 500
Water Content w [%]	15 ~ 40	Osmotic Suction h_π [kPa]	100 ~ 1000
Penetration Rate PR [mm·blow^{-1}]	4 ~ 15	P-wave Velocity V_p [m·s^{-1}]	300 ~ 800
Torque (HPT) T [N·m]	5 ~ 12	Surface Waves V_R [m·s^{-1}]	150 ~ 200
Constrained Modulus M [MPa]	100 ~ 200	Resilient Modulus M_{rDC} [MPa]	100 ~ 300

Table 2.2 Stabilized subgrade characterization

Parameter	
Surface Waves V_R [m·s^{-1}]	200 ~ 300
Constrained Modulus M [MPa]	200 ~ 500

Table 2.3 Cement-treated base characterization

Parameter	
Electrical Resistivity $\rho_{electric}$ [Ω·m]	800 ~ 5000
P-wave Velocity V_p [m·s^{-1}]	2900 ~ 3400
Surface Waves V_R [m·s^{-1}]	1400 ~ 1900
Poisson's ratio v [ ]	0.251
Constrained Modulus M [MPa]	18000 ~ 24000
Compressive Strength σ [MPa]	3 ~ 5

Table 2.4 Unbound aggregate base characterization

Parameter	
Surface Waves V_R [m·s^{-1}]	200 ~ 400
Constrained Modulus M [MPa]	300 ~ 700

Table 2.5 Asphalt concrete characterization

Parameter	
Surface Waves V_R [m·s^{-1}]	1000 ~ 2400
P-wave Velocity V_p [m·s^{-1}]	3500 ~ 4100
Constrained Modulus M [MPa]	10000 ~ 40000
Poisson's ratio v [ ]	0.307

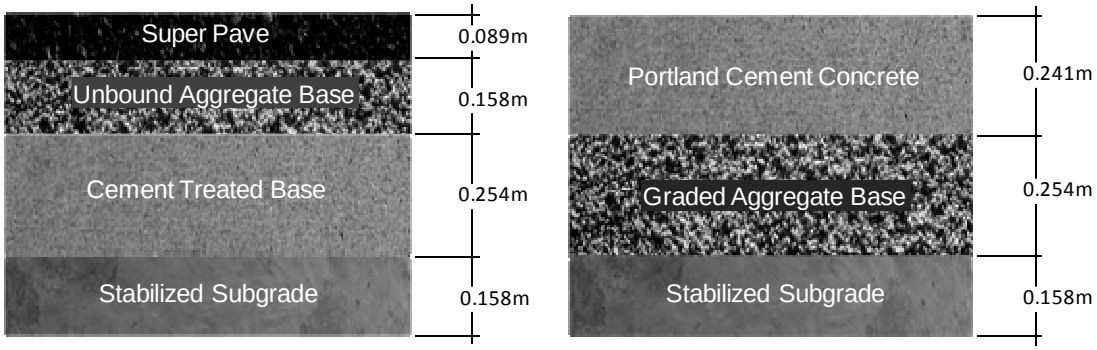

Figure 2.1 Designed inverted and conventional base sections. The upper 0.15m of the subgrade were stabilized with unbound aggregate base material in order to satisfy the design requirements.

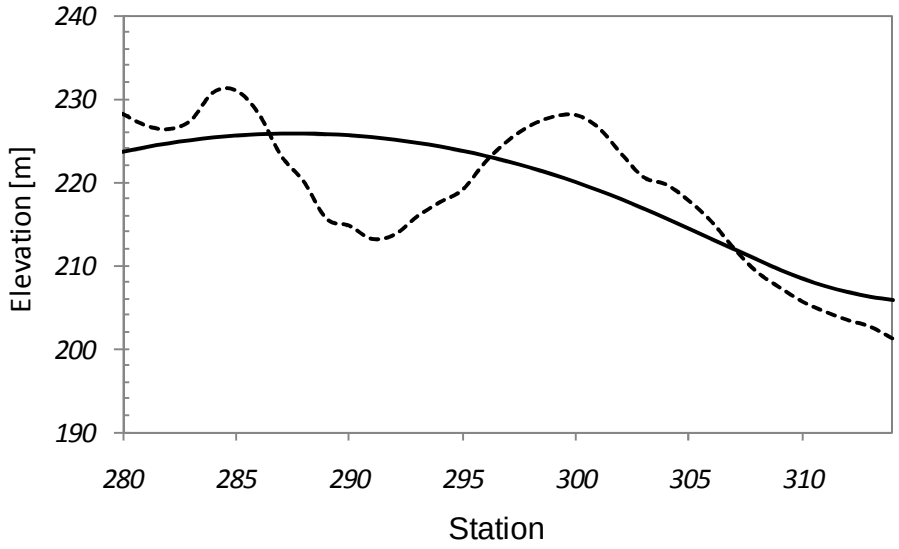

Figure 2.2 Test section original topography (dashed) overlaid by the as-built longitudinal cross section. Laboratory test samples are recovered at every station.

Figure 2.3 Stabilization of the subgrade upper 0.15m through addition of unbound aggregate base and re-compaction.

Figure 2.4 Cement-treated base construction monitoring from the time water is added to the mix to the final bituminous cover.

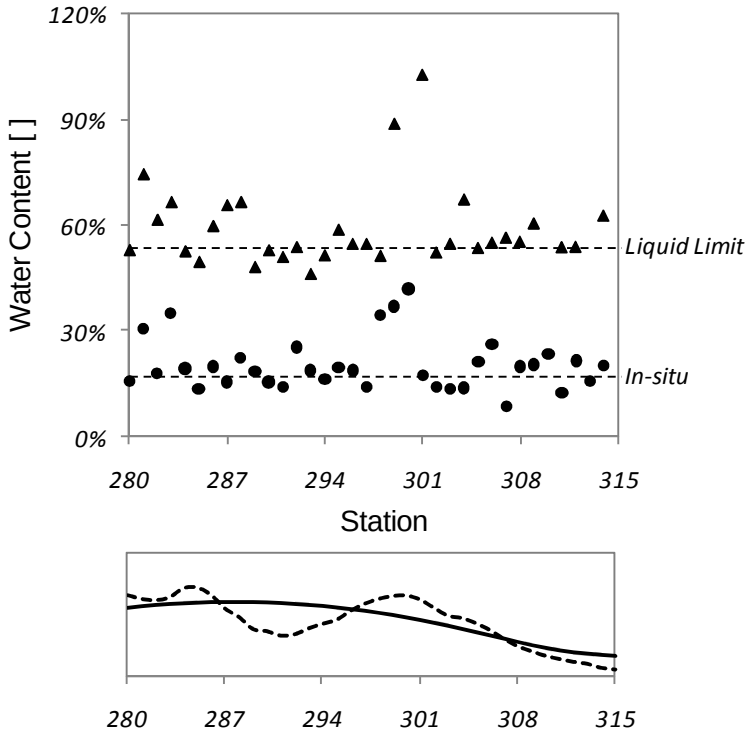

Figure 2.5 In-situ water content and liquid limit of tested soil samples. The lower plot shows the sampling locations relative to cut and fill sections.

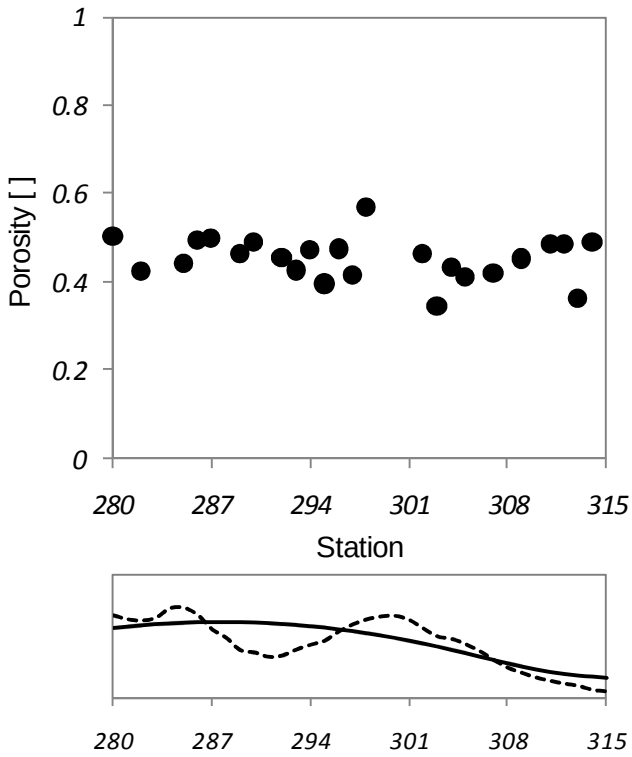

Figure 2.6 Porosity data computed from density measurements. The lower figure shows sampling locations relative to cut and fill sections.

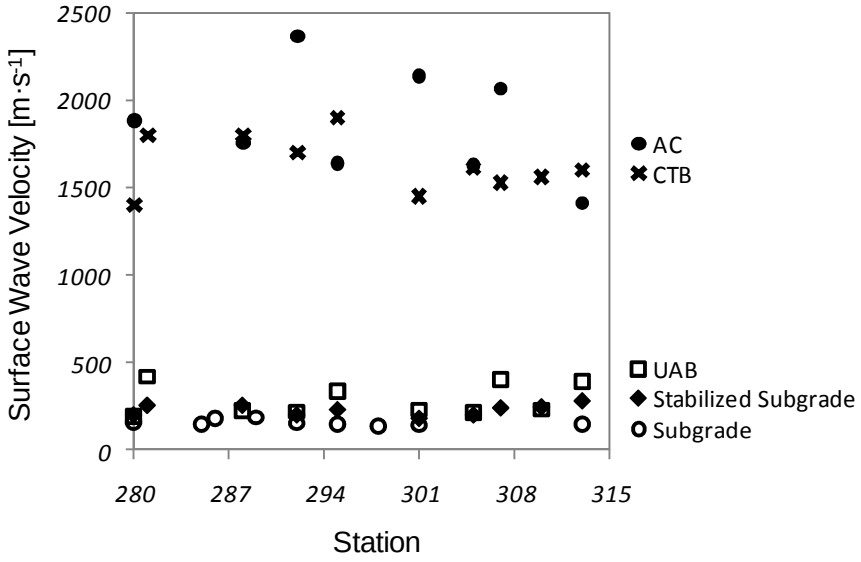

Figure 2.7 Surface wave test results for all layers.

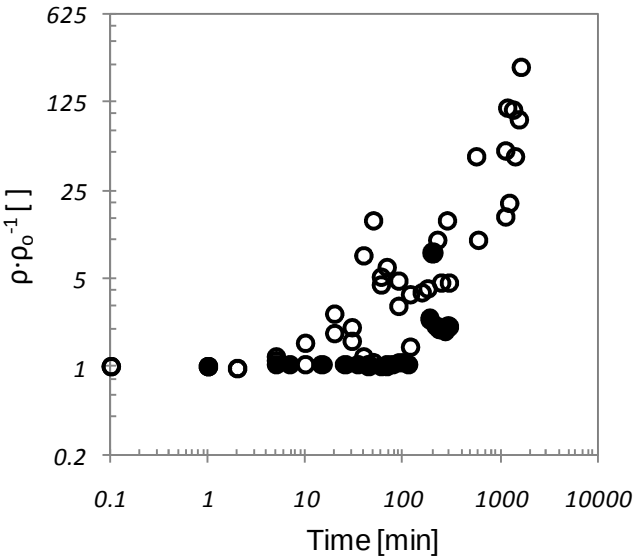

Figure 2.8 Comparison of field and laboratory normalized resistivity data. Field data (filled circles) show an increase in resistivity starting at 100min; laboratory specimens exhibit resistivity increases as soon as 20min (hollow circles).

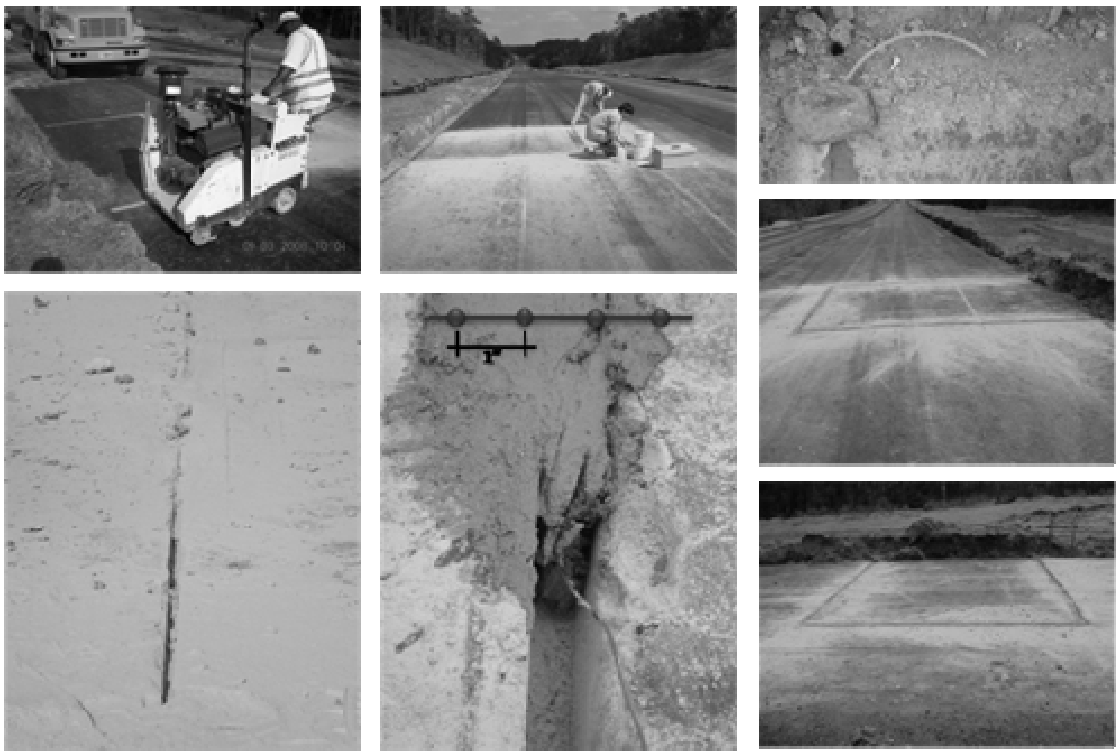

Figure 2.9 Cement-treated base integrity assessment. GDOT bridge crew cut a 6mm wide 12mm deep groove on the hardened surface which extended from the center line to the shoulder in a rectangular section. A 0.3mm diameter copper wire was buried in the groove

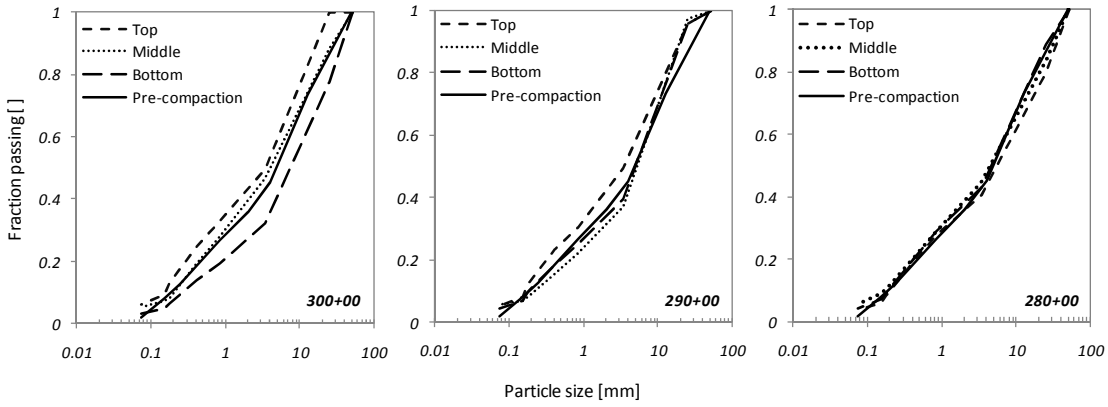

Figure 2.10 Grain size distribution of sample recovered at station 300+00, 290+00, and 280+00.

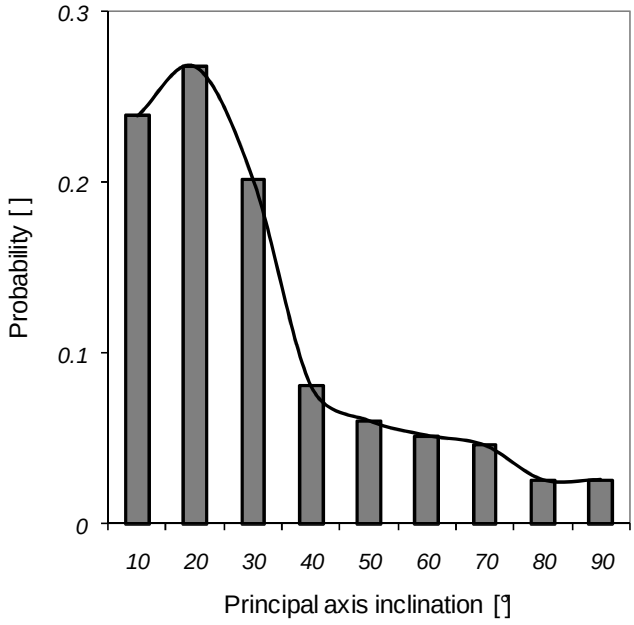

Figure 2.11 Particle orientation anisotropy from digital image processing of photographs taken during the forensic investigation

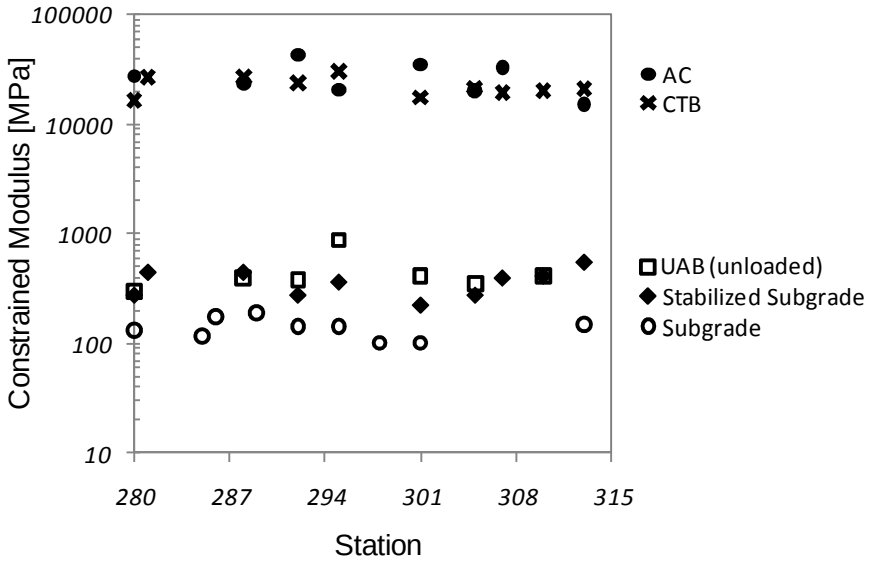

Figure 2.12 Constrained modulus calculated from surface wave velocity data.

CHAPTER 3

NEW FIELD TEST

3.1. Introduction

The stress-dependent resilient behavior of the unbound aggregate base and of the subgrade plays a critical role on the pavement response (ERES 2004; Witczak 2004). However, laboratory cyclic triaxial characterization methods are still considered complex and remain expensive for routine practice. In addition, the validity of laboratory measured moduli to represent in-situ conditions remains under scrutiny (Puppala 2008).

The in-situ assessment of stress-dependent stiffness could overcome difficulties encountered with laboratory procedures. A limited number of field studies have attempted to capture the in-situ stress-dependent stiffness of unbound aggregate layers in pavements structures. In particular, miniaturized versions of cross-hole and down-hole seismic tests were installed during the construction of an inverted base pavement structure to characterize the stiffness-stress response of the unbound aggregate base (Terrell 2002; Terrell et al. 2003). Results show a clear change in stiffness with increasing effective stress (from 180MPa unloaded, to 660MPa under a 200kPa vertical stress). However, the parameters required to appropriately capture the non-linear cross isotropic unbound aggregate behavior cannot be resolved using this or any other in-situ characterization method currently available.

Laboratory and field difficulties identified above are aggravated by reproducibility issues, the need for specially trained personnel for data analysis, and the lack of correlation between laboratory and in-situ measured stiffness. Consequently, most

state transportation agencies do not measure the resilient modulus either in the laboratory or in the field. Instead, they favor indirect methods and empirical correlations to estimate the resilient moduli of subgrade and unbound aggregate layers (Puppala 2008). The purpose of this chapter is to present a comprehensive methodology to assess the non-linear stiffness-stress response of granular bases in-situ. The method is based on the concept of stress tomography. A detailed literature review is presented first.

3.2. Review of Available Characterization Methods

3.2.1. Laboratory Methods

Laboratory tests used to evaluate the resilient behavior of unbound aggregate materials include cyclic triaxial, resonant column, simple shear, hollow cylinder, and multi-axial cubical triaxial tests. All these tests are limited by specimen size to particle size considerations.

Cyclic-load triaxial tests are most frequently used. Multiple test protocols have been proposed. The current laboratory characterization standard for resilient modulus (AASHTO T-307) emerged in an effort to develop a unique repeatable protocol. Cyclic triaxial tests are generally conducted under constant confining pressure. Variable confining pressure triaxial tests require changing the confinement in phase with the vertical load to recover data for a variety of stress paths (Andrei 1999; Adu-Osei 2000). Typically, the triaxial test is run under undrained conditions. Pore pressure data are not available in most undrained tests (even for subgrade materials) and data reduction is made using total stress analysis (Konrad 2006). Boundary effects and friction at the soil-

platen interface are reduced using a 2:1 cylindrical geometry specimen. The specimen diameter must be at least ten times larger than the maximum grain size. Since the maximum standard triaxial specimen size in practice is 0.15m, this geometric constraint limits the maximum particle size of the tested aggregate to 0.015m. However, unbound bases often contain maximum size aggregates larger than 0.025m which violates geometric constrains for a standard 0.15m cell. Thus a compromise has been made to use standard cells for unbound aggregate base materials after removing particles larger than 0.025m (Witczak 2004). Laboratory measured resilient moduli are often reported as averages with no information given about the variance in the collected data leading to a false sense of certainty in the measurement.

Early numerical studies invoked anisotropic material properties that were assumed but not measured (Barksdale et al. 1989; Tutumluer and Barksdale 1995). ICAR developed a protocol to measure anisotropic material properties using three triaxial stress regimes (triaxial compression, triaxial extension, and triaxial shear) with ten static stress states each in order to determine stress sensitivity and the level of anisotropy. Data reduction and analysis of the test results is conducted by a system identification algorithm that uses all the applied stresses and corresponding strains to invert the five cross-isotropic elastic material properties (Adu-Osei 2000).

3.2.2. Field Methods

The most common field test used to determine the resilient modulus of unbound layers is the falling weight deflectometer (Puppala 2008). The falling weight deflectometer provides an indirect assessment of the material stiffness without sampling. The less common seismic pavement analyzer uses the spectral analysis of surface waves

technique to estimate the stiffness profile of the pavement structure (Nazarian et al. 1995). The main disadvantage of the falling weight deflectometer and the seismic pavement analyzer is the need for a formal inversion to recover the unknown parameters. The information that can be extracted is limited by the amount of information embodied in the measured data. When insufficient information is available, the analysis yields non-unique solutions, and vastly different parameters can be extracted for the same data set.

3.2.3. Summary of Observations

The analysis of inverted base pavement structures requires an accurate representation of the stress-dependent stiffness of the unbound aggregate base. The stress states used in current test protocols was dictated by representative field loading conditions that unbound aggregates experience in conventional pavement structures. The unbound aggregate base in an inverted pavement structure is subjected to considerably higher stresses. Therefore, the mechanical response must be analyzed using material parameters recovered from the proper state of stress rather than by extrapolation. Standard in-situ methods used in practice cannot assess the stress-dependent stiffness of unbound layers; thus, the measurements do not provide enough information to recover constitutive parameters needed to appropriately model the behavior of these layers. Such information is critical in inverted pavements where the granular layer plays a key structural role. It becomes evident that the proper analysis of inverted base pavements requires new test protocols to capture the non-linear stiffness-stress response of the as-built unbound aggregate base.

3.3. Determination of Stiffness-Stress Parameters – Test Design

The P-wave velocity reflects the stiffness of the soil skeleton in unsaturated sediments. The proposed test involves two linear arrays of piezopads which are used for P-wave sources and receivers (figure 3.1). Each measurement consists of P-waves emitted from a single sensor in the source array and simultaneously recorded in tomographic mode at all sensors in the receiver array. Thus, horizontal and diagonal travel paths are involved.

3.3.1. Test Design – Physical Considerations

Constraints imposed by the maximum aggregate size D_{90}, the thickness of the layer *h*, the proximity to stiff layers P, separation between arrays *s*, and the wave length λ of the emitted signal must be taken into consideration for proper test design. Preliminary guidelines include:

1. $s > 10D_{90}$ (spatial averaging considerations)
2. $s < h$ (to emphasize direct arrival)
3. $\frac{V_1}{V_2} \leq \frac{(L-3P)}{(L-2P)}$ (to prevent refracted path)
4. $s > 4\lambda$ (far field considerations)
5. $\lambda >> D_{50}$ (equivalent continuum assumption – note that Brillouin limits $\lambda=2D_{50}$)

The physical constraints imposed by these expressions cannot be simultaneously satisfied; thus, a compromise must be made and consequences must be clearly understood. The most challenging condition to meet is the one imposed by the ratio between the wave length and the aggregate size. A maximum aggregate size D_{max}=0.038m requires $\lambda \approx 0.38$m which would in turn force the separation between arrays to be $s \geq 1.52$m. In the field, the proximity of the stiff asphalt concrete and cement-treated

base limits the source receiver separation to $s < 0.152$m. The type of sensor places an additional constraint on the maximum allowable distance between source and receiver forcing a violation of the continuum assumption $\lambda >> D_{50}$. Paradoxically, the continuum assumption is still needed to analyze the P-wave data.

Taking into consideration the described physical constraints, a compromise inter-array spacing $s = 0.1$m was selected. The P-wave velocities measured in preliminary laboratory testing of a well-graded crushed granite aggregate (D_{50}=0.005m) range between 260 and 740m·s^{-1}. The frequency for the recorded waves is in the order 10kHz; thus, the wave length ranges between $\lambda \approx 0.026$ and 0.074m. Considering that the aggregate is well graded, D_{50} is a good indicator of particle size. Then, the selected sensor separation satisfies condition 1, condition 2 for unbound aggregate bases thicker than 0.1m, and condition 3. Condition 4 is not fully satisfied; however, the ratio $\lambda / D_{50} \approx 5$ to 15 exceeds the Brillouin filter.

3.3.2. Sensor Installation

The installation of sensors is critical for the in-situ characterization of the non-linear stiffness-stress response of unbound aggregate bases. Our goal in this study was to identify optimal drilling procedures to penetrate through the asphalt concrete layer and into the aggregate base while minimizing the disturbance of the layer. We sought to drill the smallest borehole that would allow the installation of high energy sensors to facilitate wave detection in noisy environments. After considering and testing multiple alternatives we opted for using 0.013m diameter piezopads and a borehole diameter of 0.016m drilled dry using a rebar cutter and a diamond core bit (figure 3.2). Two boreholes separated 0.1m are drilled to house the source and receiver arrays which are placed facing each

other. The boreholes are filled with dry fine Ottawa sand tamped with a rod to a dense state. The sand fill acts as the coupling medium for wave propagation and provides lateral support to the granular base.

3.4. Test Results

3.4.1. Laboratory Prototype – Zero-Lateral-Strain P-Wave Velocity Measurements

Preliminary test prototypes lead to the development of a laboratory procedure that permits the simultaneous determination of the vertical and radial stiffness-stress response. The unbound aggregate base material is mixed at the optimum water content, placed in a Proctor-type mold, and compacted in a vibratory table for 15 minutes under a 240N weight i.e., a vertical stress of 13kPa. The upper mold extension is removed and the material is leveled so that it occupies the full volume of the lower half of the mold (0.152m diameter and 0.116m height). Two boreholes are drilled though the compacted material. Then, the aluminum platen shown in figure 3.3-a is secured on top of the specimen with the small holes sitting directly on top of the boreholes to allow for the installation of the source and receiver arrays. The base of the Proctor mold is removed and replaced by the aluminum platen shown in figure 3.3-b. The center holes in the top and bottom platens house two Matec 9J104 piezocrystals that measure vertically propagating P-waves (figure 3.3-c). The instrumented cell is placed in the loading frame and the sensors are connected to the peripheral electronics. P-waves are generated by a wave form generator (Agilent 3320A) using square signals with 10V amplitude at a frequency between 20 and 120Hz. Signals picked up by the array of receivers are pre-

amplified and filtered to remove high frequency noise (Krohn-Hite 3364). The pre-conditioned signals are fed into a 4-channel oscilloscope (Agilent 54624A) and stored into a laptop computer via a GPIB card connection.

The specimen undergoes 25 cycles of preconditioning loading-and-unloading with vertical stress amplitude of 700kPa. The unloading after the final cycle is stopped at a vertical stress of 14kPa to simulate the overburden on the unbound aggregate base. The first measurements are made starting at 14kPa and every 80kPa until the vertical stress is 580kPa which is 83% of the maximum preconditioning vertical stress. Five signals are recorded at each load increment (Figure 3.3-c): vertical propagation (VV), horizontal propagation at mid-height and bottom (MM and BB), and two diagonal propagations at an angle of 24° with the horizontal (MB and BM).

Signals recorded at 8 different load increments during loading and unloading are plotted in figures 3.4 and 3.5 for different propagation directions. While there is clear stress dependency, the identification of the first arrival is rather complex in part due to concurrent travel paths along the steel shell but also because of the tight physical conditions and compromised geometry discussed earlier. Results for VV and BB propagation are summarized in figure 3.6.

3.4.2. Field P-Wave Velocity Measurements - Inverted Base Pavement Structure

The proposed field characterization of the stiffness-stress response of the unbound aggregate material was performed in a Lafarge quarry access road in Morgan County, Georgia. The road is an inverted base pavement section constructed in 2001 as part of a GDOT sponsored research project and has experienced uninterrupted high volume of heavy truck traffic for 9 years. Surveys conducted May 2008 showed the section had

serviced over 1.2 million ESALs after 7 years, about 75% of the designed service life without exhibiting signs of failure; in fact, there are still no signs of failure or changes in rideability at present (Lewis 2009). The original research on the haul section included a comprehensive characterization of the unbound aggregate base, details in (Terrell 2002; Terrell et al. 2003).

Boreholes were drilled through the asphalt layer and into the unbound aggregate base. Then, source and receiver arrays were placed inside the boreholes and these were backfilled with fine Ottawa sand. The peripheral electronics were the same as those used in the laboratory. The first set of P-wave measurements were performed in the absence of externally applied loads. After that, a loaded Caterpillar 769D water truck was used to load the pavement in order to measure the stiffness-stress response of the base. The tire applies a 552kPa distributed load over a quasi-circular area of radius r = 0.25m. The tire location at the time of the measurements is shown in figure 3.7. The tire load is represented by an equivalent circular contact area of radius r and a distributed load Q. A set of 4 P-wave measurements are performed for each tire location: 2 horizontal paths (MM and BB) and 2 diagonal paths (MB and BM at an angle of 24° with the horizontal); each measurement is repeated 3 times. Signal stacking is used to improve the signal to noise ratio (2048 signals). This situation precludes the continuous monitoring of the stiffness-stress response under a passing vehicle. The distance between the load centerline and the buried sensors varies between 0.325 and 0.98m (figure 3.7). The water truck tire passes 6 times over the marked locations and 4 sets of 3 signals are recorded for each tire location.

A set of recorded signals is presented in figure 3.8 for the 4 tire-sensor distances tested. Electromagnetic cross talk causes the false first arrival observed at $t \approx 0$sec. The first arrival is determined by subtracting ¾ of the period T from the first negative peak. Measured P-wave velocities as a function of the distance between the tire and the sensors are presented in figure 3.9.

3.5. Analysis and Discussion

The P-wave velocity in unsaturated unbound granular media is determined by the state of effective stress in the propagation direction (Kopperman et al. 1982; Hardin and Blandford 1989).

$$V_{pz} = \alpha\left(\frac{\sigma_z'}{1kPa}\right)^{\beta} \qquad 3.1$$

$$V_{pr} = \alpha\left(\frac{\sigma_r'}{1kPa}\right)^{\beta} = \alpha\left(\frac{K_o\sigma_z'}{1kPa}\right)^{\beta} = \alpha K_o{}^{\beta}\left(\frac{\sigma_z'}{1kPa}\right)^{\beta} \qquad 3.2$$

where V_{pr} is the velocity of waves propagating in the horizontal direction, V_{pz} is the velocity of waves propagating in the vertical direction, and K_o is the ratio of the effective horizontal to vertical stress. The α factor is the value of V_p when σ'=1kPa and β captures the stress sensitivity of P-waves.

The P-wave velocity is related to the constrained modulus M by $M = \rho\left(V_p\right)^2$, where ρ is the mass density of the compacted unbound aggregate. Then, the constrained modulus stress dependency is obtained from equations 3.1 and 3.2.

$$M_z = \rho\alpha^2\left(\frac{\sigma_z'}{1kPa}\right)^{2\beta} \qquad 3.3$$

$$M_r = \rho\alpha^2\left(\frac{K_o\sigma_z'}{1kPa}\right)^{2\beta} = \rho\alpha^2 K_o{}^{2\beta}\left(\frac{\sigma_z'}{1kPa}\right)^{2\beta} \qquad 3.4$$

or in terms of *k*-type model parameters:

$$M = k_1\left(\frac{\sigma'}{1kPa}\right)^{k_2} \text{ where } k_1 = \rho\alpha^2 \text{ and } k_2 = 2\beta \qquad 3.5$$

3.5.1. Determination of Stiffness-Stress Parameters from Laboratory Measurements

Vertical and horizontal P-wave velocities measured in the laboratory collapse onto a single trend for K_o= 0.38, and the full data set can be captured using α= 245m·s^{-1} and β= 0.18 (figure 3.10). For the same α and β values in the vertical and horizontal direction, $V_{pr} = mV_{pz}$, where $m = K_o^{\beta}$, and $M_r = m^2M_z$. Calculated constrained moduli are presented in figure 3.11 for the measured ρ= 2000kg·m^{-3} and the inverted values of K_o= 0.38, α= 245m·s^{-1} and β=0.18.

3.5.2. Determination of Stiffness-Stress Parameters from In-Situ Measurements

The recovery of material parameters from the field test requires a detailed analysis. The in-situ stress field is not uniform, stresses vary along the propagation path, the propagation direction is not necessarily aligned with a principal stress direction, and load conditions are not exactly zero-lateral-strain despite the fact that the stiff layers in the inverted pavement offer confinement for the unbound aggregate layer.

The experimentally measured P-wave travel time is an integral along the propagation path:

$$t_{\exp} = \int\frac{dl}{V_P} = \int\frac{\sqrt{\rho}}{\sqrt{M}}dl = \int\frac{dl}{\alpha\left(\frac{\sigma'}{1kPa}\right)^{\beta}} \qquad 3.6$$

The model parameters α, β, and K_o can be recovered through inversion using successive forward simulations (figure 3.12-a). For the purpose of this study, and given the loading configuration, we use stress conditions at the mid-point between the source and receiver arrays to invert the parameters (figure 3.12-b). Note that the limited number of measurements supports the extraction of a minimum set of material parameters rather than a full set for cross-isotropic stiffness parameters.

The material parameters recovered from the laboratory zero-lateral-strain cell experiment are used as input for a finite element model of the inverted base pavement structure that is used to estimate the stress for a fist order estimate of the constitutive parameters in-situ. Details on the finite element model can be found in chapter 5. The constitutive models and material parameters used in the FEM simulation are summarized in table 5.1.

The numerical simulation results were used to estimate the in-situ mean stress at the mid-point between the sensors for the multiple load configurations tested. This data allows us to invert the in-situ material parameters using error surface analysis. The in-situ stiffness-stress relationship is given by:

$$E_{Rh}[MPa] = 170\left(\frac{p}{1kPa}\right)^{0.12} \qquad 3.7$$

In-situ measured P-wave travel times (t_m) and the first iteration predictions based on zero-lateral-strain calibrated material parameters (t_p) for the four load configurations tested are presented in table 3.1.

3.6. Summary and Conclusions

The stress dependent stiffness of unbound aggregate layers determines the performance of inverted base pavement structures. Therefore, an accurate characterization of the stiffness-stress response is critical for inverted pavement design. Available laboratory protocols fail to reproduce the in-situ stress levels to which unbound aggregate bases are subjected to in an inverted pavement structure, and available in-situ measurements fail to gather sufficient information to extract the constitutive parameters required to appropriately model unbound aggregate behavior.

In an inverted pavement structure the unbound aggregate layer is confined by the stiff asphalt concrete and the cement-treated base. Thus, the highest load condition under the wheel can be better represented as a zero-lateral-strain K_o loading configuration.

A laboratory K_o test was prototyped for the characterization of the stiffness-stress response of unbound aggregate materials based on the concept of stress tomography. P-wave velocities measured in the vertical and horizontal directions collapse onto a unique trend for a single set of K_o, α, and β. Then, $V_{pr} = mV_{pz}$, where $m = K_o^{\beta}$.

The concept of P-wave stress tomography was applied in-situ to characterize as-built unbound aggregate bases. The test has been successfully used to measure the in-situ stiffness-stress response of an existing inverted pavement structure.

In-situ test results show that material models reported in the literature (developed from existing laboratory test protocols) under-predict the in-situ stress-dependent stiffness of the unbound aggregate base. Material parameters recovered from zero-lateral-strain stiffness measurements yield better predictions of in-situ performance; however, tend to over-predict the stiffness at higher stresses.

Table 3.1 Comparison between in-situ measured P-wave travel times (t_m) and the first iteration predictions based on zero-lateral-strain calibrated material parameters (t_p) for the four load configurations tested.

Distance [m]	p [kPa]	t_m [μs]	t_p [μs]
0.926	*2.7*	*292*	*319*
0.665	*3.7*	*285*	*308*
0.439	*17*	*269*	*240*
0.308	*76*	*253*	*195*

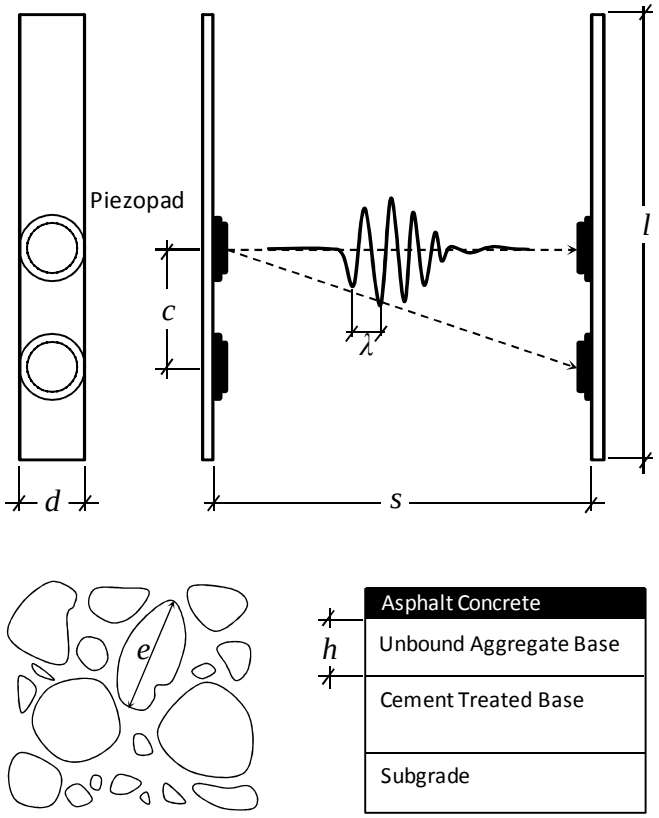

Figure 3.1 Graphical description of the designed sensors and relative scales that influence the selection of sensor size and positioning.

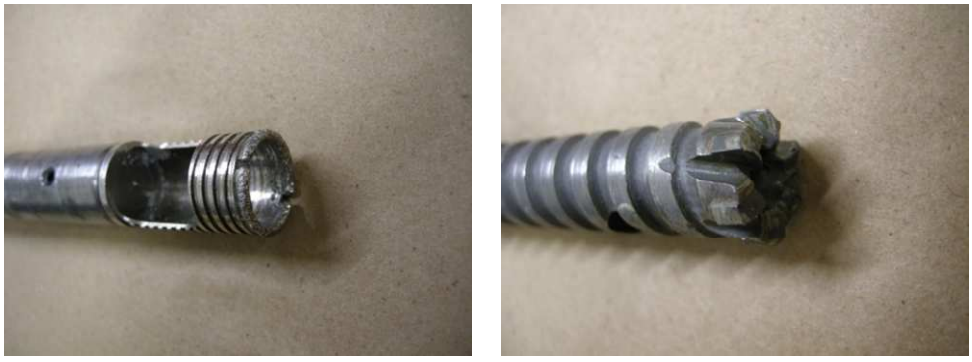

(a) (b)

Figure 3.2 Borehole drilling tools (a) diamond core bit and (b) rebar-cutter.

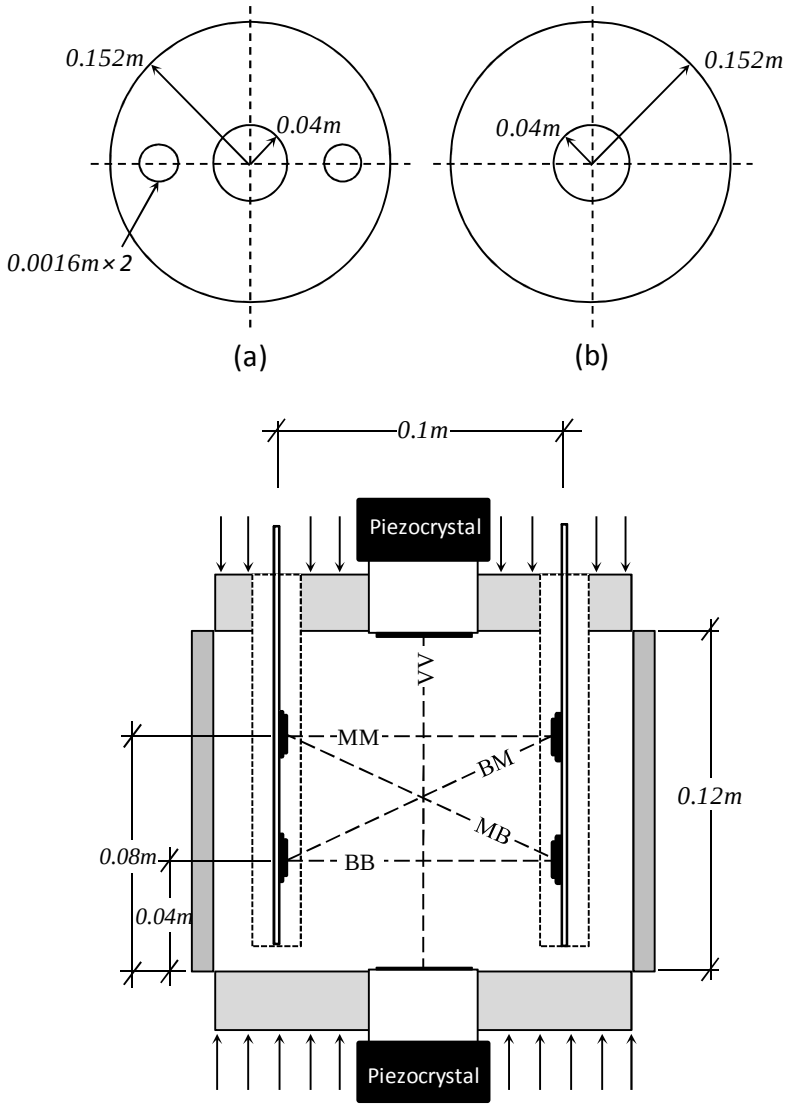

Figure 3.3 Instrumented laboratory zero lateral strain test cell: (a) upper platen used as a guide for borehole drilling and sensor installation, (b) lower platen, (c) fully instrumented cell.

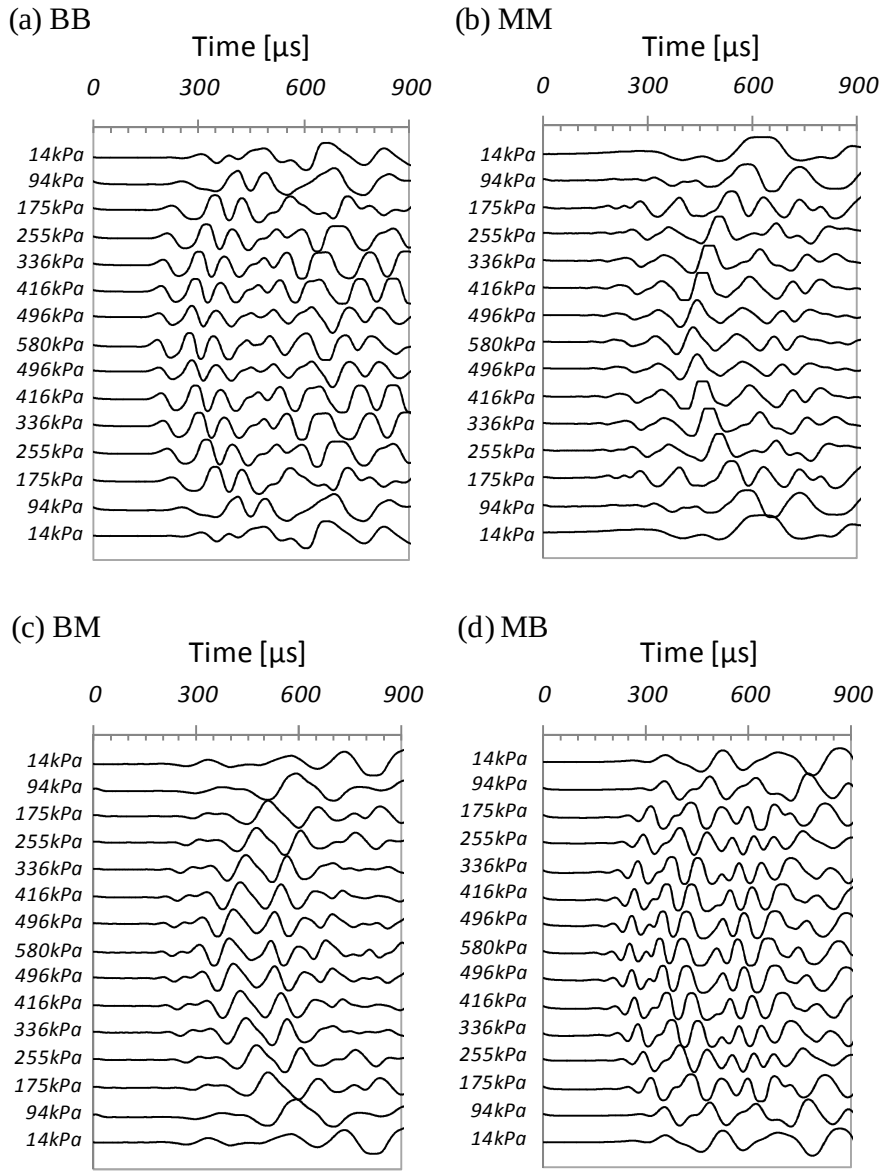

Figure 3.4 Laboratory test data results, signature cascades as a function of the applied vertical stress for horizontal and diagonal rays (a) bottom source-receiver pair BB, (b) middle source-receiver pair MM, (c) bottom-to-middle source-receiver pair BN, and (d) middle-to-bottom source receiver pair MB.

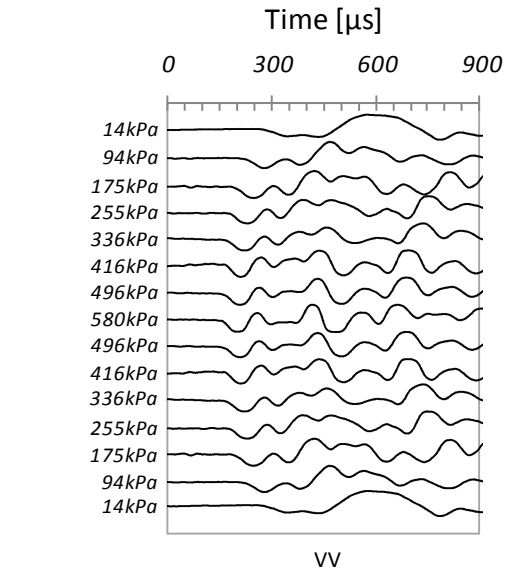

Figure 3.5 Laboratory test data results for waves propagating in the vertical direction VV. Signature cascade as a function of the applied vertical stress.

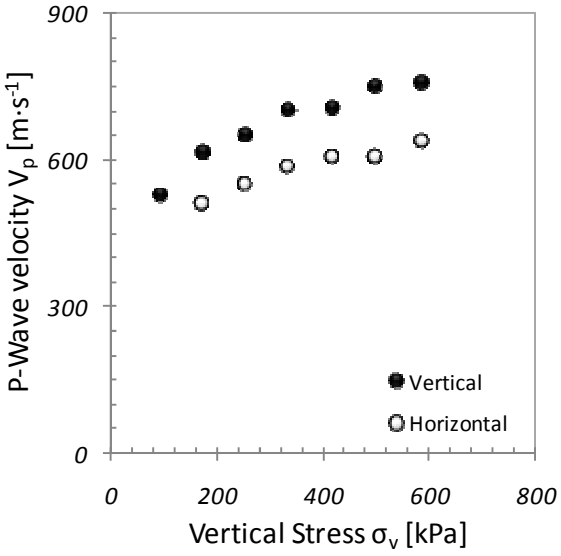

Figure 3.6 Vertical and horizontal P-wave velocities as a function of the applied vertical stress.

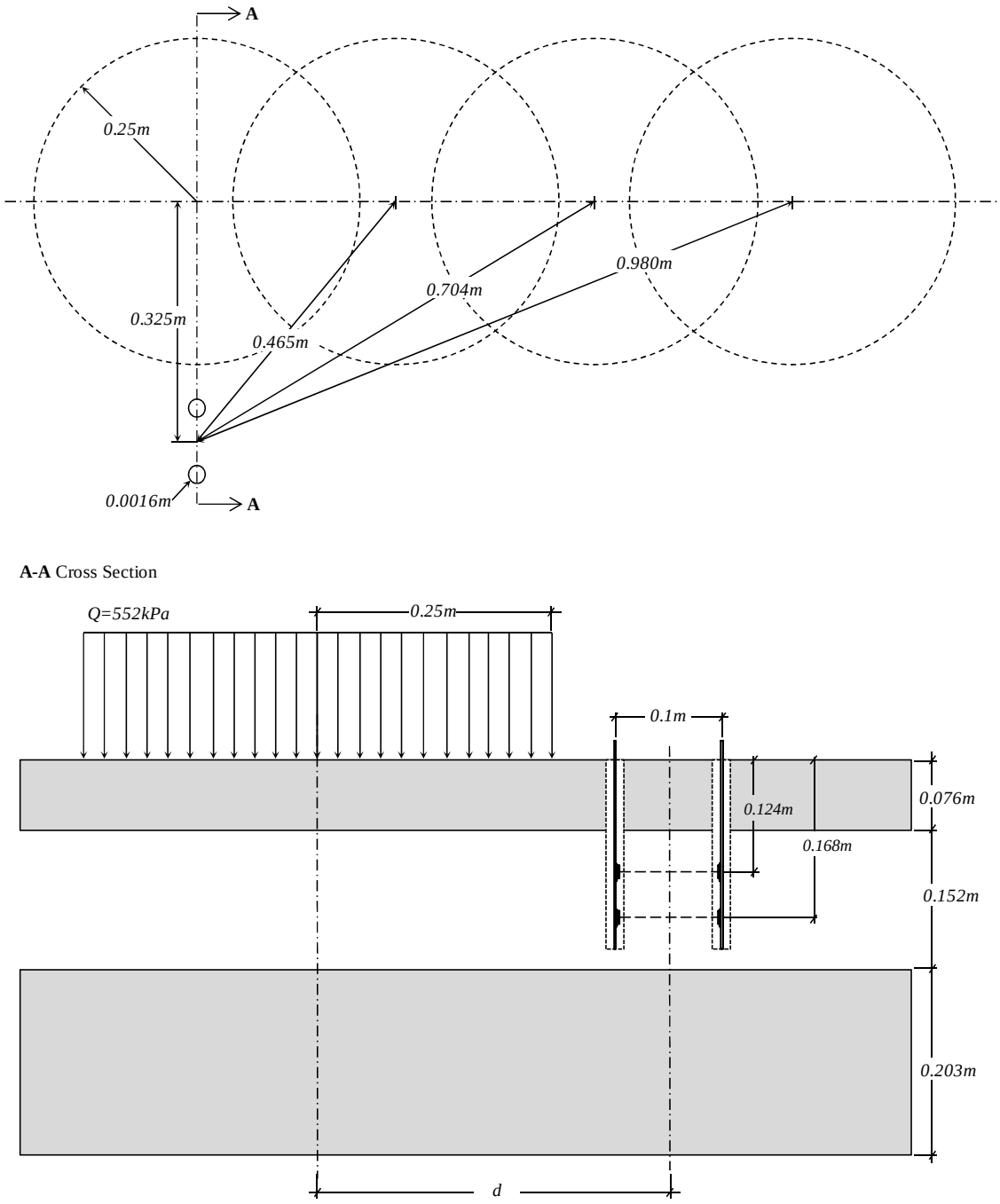

Figure 3.7 Field test loading configurations: plan view and cross section.

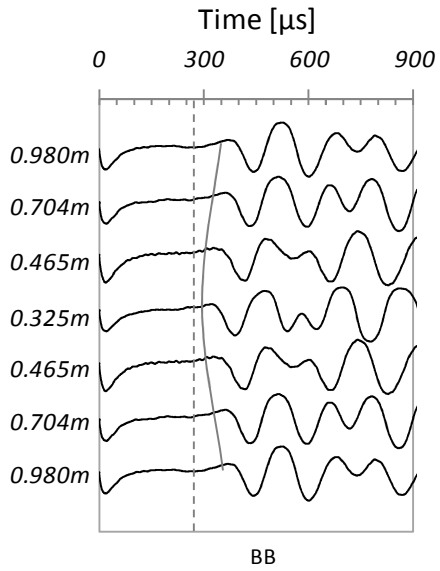

Figure 3.8 Field test data results for horizontally propagating waves between sensors buried at 0.17m (BB) from the pavement surface. Signature cascade as a function of the proximity to the loaded truck.

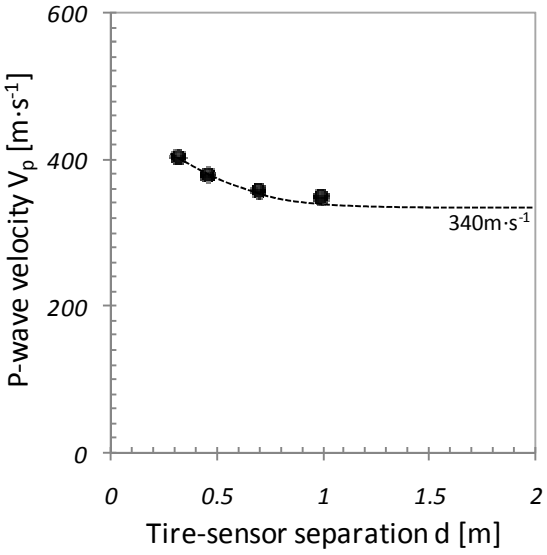

Figure 3.9 P-wave velocity as a function of the distance between the tire centerline and the mid-point between the source and receiver. The asymptotic trend captures the unloaded P-wave velocity.

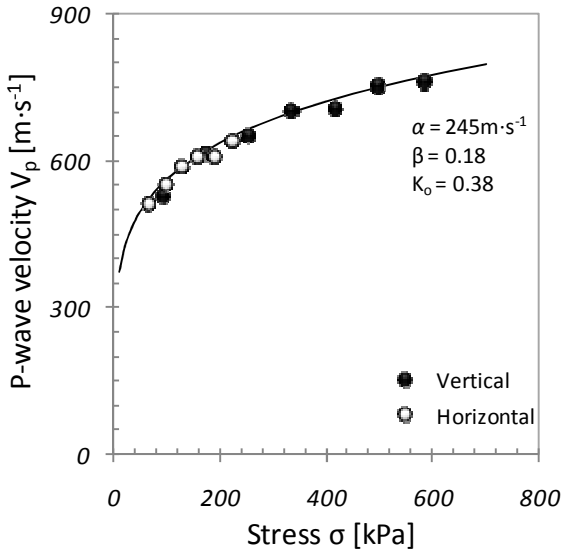

Figure 3.10 P-wave velocity as a function of the stress in the direction of wave propagation. The entire data set collapses under a single power law trend with a 245m·s^{-1} α coefficient, 0.18 β exponent for a K_o coefficient of 0.38.

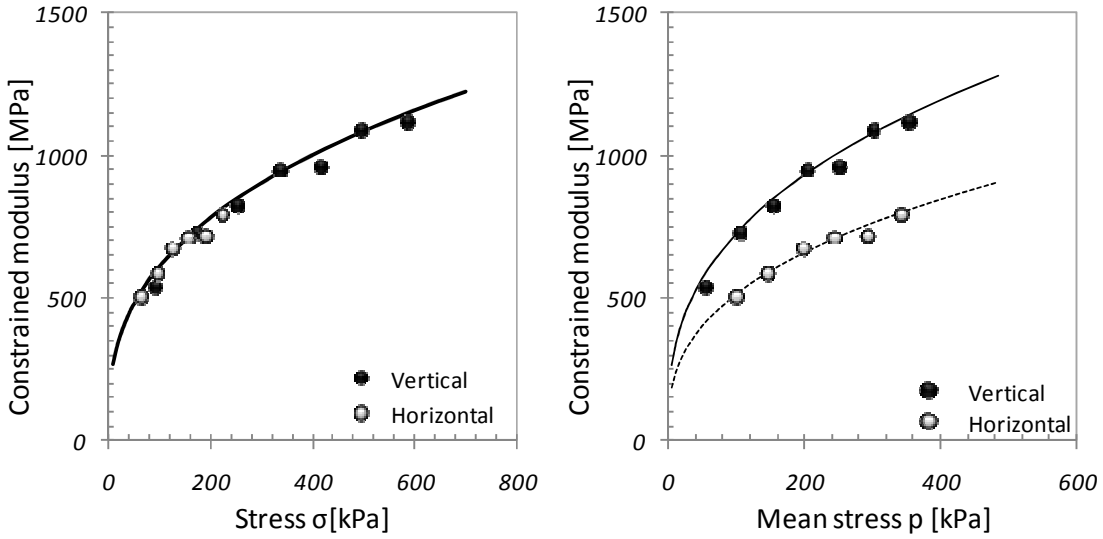

Figure 3.11 Laboratory measured and predicted constrained moduli in the vertical and horizontal directions as a function of the stress in the direction of P-wave propagation and the mean stress.

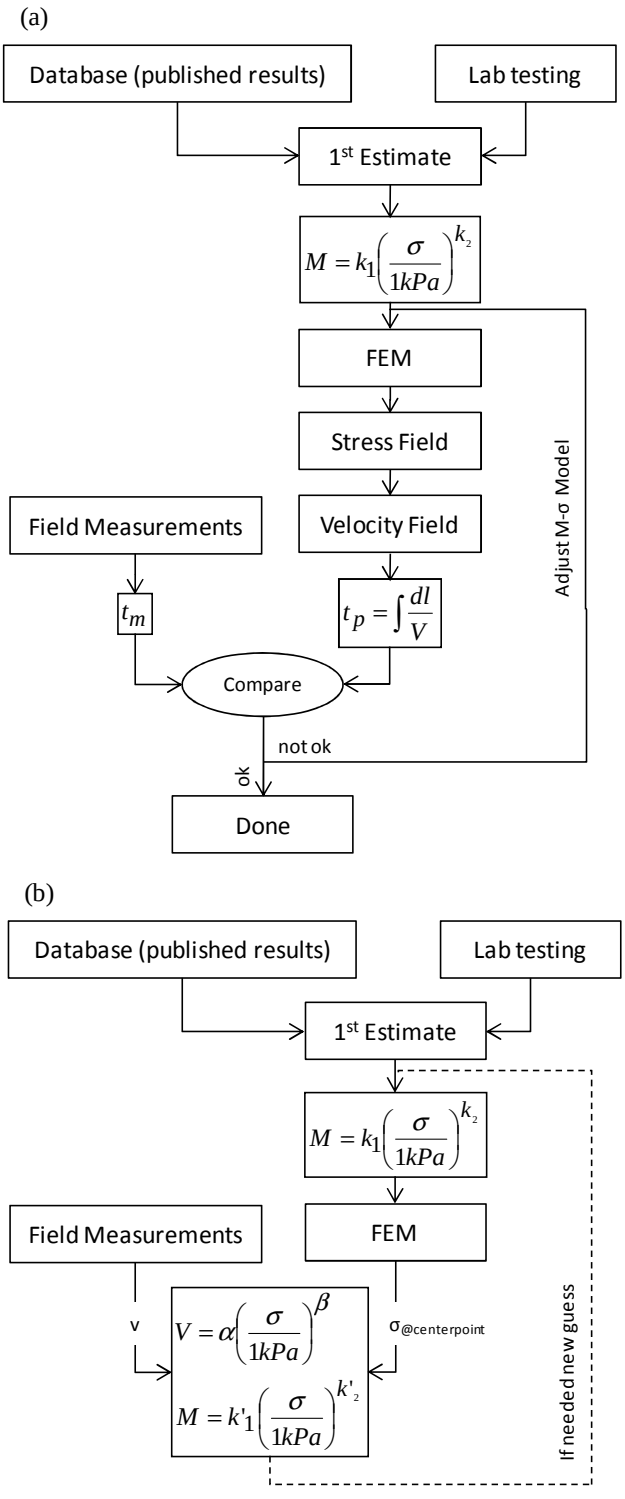

Figure 3.12 Advanced (a) and simplified (b) in-situ material parameter inversion

CHAPTER 4

UNBOUND AGGREGATE BASES:

CONSTITUTIVE MODEL SELECTION AND CALIBRATION

4.1. Introduction

Unbound aggregate bases exhibit non-linear stress-dependent behavior. Under repeated loading, plastic deformations gradually decrease with the number of load repetitions until only elastic strains take place during loading; this is also known as the "elastic shake down" state. The resilient modulus captures the ratio of the cyclic stress amplitude to the elastic strain at this stage. The non-linear material behavior must be considered in mechanistic pavement design methods. However, initial attempts in the AASHTO (1993) pavement design guide are overshadowed by the empirical nature of the guide. The stress-dependent non-linear response of unbound aggregate bases has a profound effect on inverted base pavements where the unbound aggregate is subjected to high changes in stress and stiffness during loading-unloading cycles. It is therefore essential to properly capture the material response in constitutive models used in numerical codes.

There is an inherent trade-off between an accurate representation of complex granular media behavior and the need for simplicity and robustness required for routine analysis. This chapter starts with a fundamental analysis of the factors that control the resilient behavior of unbound aggregate bases, followed by a comprehensive review of available material models developed within the framework of pavement analysis. This review leads to a critical assessment of available models within the framework of inverse

problems. A robust model is selected based on information theory concepts, and a procedure is developed to invert physically meaningful material parameters. Data available in the literature are used for calibration of the material model and results are compared to reported predictions.

4.2. Resilient Modulus – A Granular Media Perspective

The large-strain load-deformation response of unbound aggregates is determined by changes in the granular skeleton. Conversely, the small-strain resilient load-deformation response occurs at constant fabric and the macro-scale deformation integrates contact-level particle deformation. Available experimental studies show that the main parameters that control the resilient response of the granular base are: stress history, stress level (mean and deviatoric stress, and load duration), density, gradation (grain size and uniformity), and moisture conditions. In this section we summarize experimental observations on the resilient behavior of unbound aggregates and offer a particle-scale analysis of causal mechanisms. A comprehensive precedent to this review can be found in the work by Lekarp et al. (2000).

4.2.1. State of Stresses

The state of stress has the most significant effect on the resilient response of unbound aggregate bases. The resilient modulus increases with the mean stress and decreases slightly with increasing amplitude of the repeated deviator stress (Morgan 1966; Monismith et al. 1967; Hicks and Monismith 1971; Smith and Nair 1973). The resilient modulus approaches asymptotic values with repeated loading and becomes insensitive to stress history provided the applied deviatoric stress remains away from

failure. Load duration and frequency do not affect the resilient behavior of granular materials for moisture contents at or near optimum; however, the resilient modulus is likely to decrease with increasing loading frequency when loading occurs near saturation (Lekarp et al. 2000).

The velocity of P-waves in an unbound aggregate responds to similar small-strain mechanisms and it is related to the medium stiffness as $V_p = \sqrt{M\rho^{-1}}$. Several studies have shown that the velocity V_p of P-waves propagating in a principal effective stress direction is only affected by the principal stress in the direction of propagation σ' (Kopperman et al. 1982; Hardin and Blandford 1989). The relationship is captured using the power function:

$$V_p = \alpha\left(\frac{\sigma'}{1kPa}\right)^{\beta} \qquad 4.1$$

where the fitting parameters are the factor α which represents the P-wave velocity at σ'=1kPa and the exponent β which describes the stiffness sensitivity to a change in the principal stress in the direction of wave propagation.

4.2.2. Density

The resilient modulus increases with increasing density. Denser granular assemblies have a higher coordination number which increases skeletal stability and decreases the average inter-particle contact force and contact deformation (figure 4.1-a,b - Trollope et al. 1962, Hicks 1970, Robinson 1974, Rada and Witczak 1981, and Kolisoja 1997). While early studies reported relatively low density effects on the resilient modulus (Thom and Brown 1987), more recent works have shown that the effect of density can be

considerable on the resilient modulus of low density materials (Vuong 1992), and at low mean stress (Barksdale and Itani 1989; Konrad 2006).

4.2.3. Grain Size Distribution

The unbound aggregate base stiffness initially increases with higher fines fraction as a result of an increase in coordination number caused by pore-filling fines. Beyond a certain threshold, the soil skeleton is dominated by the presence of fine particles and coarse particles float in an skeleton made of fines (figure 4.1-c), the soil matrix becomes fines-dominated and the resilient modulus reduces considerably (Jorenby and Hicks 1986). This mechanism could in part explain the conflicting observations found in the literature where results vary from a minor increase to a dramatic drop in resilient modulus with increasing fines content ranging from 0 to 10% (Hicks 1970; Barksdale and Itani 1989).

4.2.4. Moisture Content

Capillary forces add to skeletal forces in unsaturated particulate media (figure 4.1-d). As a result, the stiffness of the unbound aggregate increases in unsaturated bases (Dawson et al. 1996; Santamarina et al. 2001). Higher capillary suction can be generated in the small pores of fine grained subgrades. However, moisture also influences the coarser aggregates used as bases and sub-bases: studies conducted using gravels (0.04m maximum particle size) and rock fill show that the compressibility of the medium is affected by changes in moisture introduced by wetting and drying (Oldecop and Alonso 2003).

4.2.5. Particle Shape

Rough angular to sub-angular shaped particles tend to interlock and to develop stronger (yet not necessarily stiffer) granular assemblies (figure 4.1-e). Rough angular particles also tend to form looser packings than round smooth particles (Cho et al. 2006), and can accommodate a higher volume of fine particles while maintaining a coarse particle matrix. Aggregate shape is also a factor in the development of stiffness anisotropy. Flat and elongated (i.e., eccentric) grains in unbound aggregate bases favor preferential particle alignment under gravity and/or compaction (figure 4.1-f). Anisotropy in particle orientation contributes to anisotropy in the mechanical properties of the layer (Kim 2004). The analysis of the α-β parameters (equation 4.1) recovered from angular and rounded particle mixtures under virgin loading and recompression reveal that particle shape does not influence the β-exponent as much as the α-factor (figure 4.2). Note that Cho et al. (2006) present data for virgin compression, while the results shown in figure 4.2 correspond to the same data set but for recompression. In summary, when properly densified, rough and angular crushed aggregates make stronger bases with a higher resilient modulus (Allen and Thompson 1974; Thom and Brown 1988; Barksdale et al. 1989; Kim et al. 2005).

4.3. Available Constitutive Models

An isotropic linear elastic material can be modeled with two elastic parameters; however, five parameters are required to model cross isotropic linear elastic materials. The stress dependent non-linear response of unbound aggregates requires more complex models. We seek to find the simplest and best predictive model for pavement

applications. The review presented here extends the comprehensive compilation conducted by Lekarp et al. (2000).

Available constitutive models are summarized in table 4.2. All models attempt to capture the variation in the unbound aggregate stiffness in response to changes in confining stress (Brown and Pell 1967; Monismith et al. 1967; Seed et al. 1967; Hicks 1970; Rada and Witczak 1981). More sophisticated expressions include the effect of the deviator stresses (Thom and Brown 1988; Nataatmadja 1992; Pezo 1993; Kolisoja 1997; Van Niekerk et al. 2002; Rahim and George 2005). The influence of other physical parameters such as porosity is captured explicitly (Zaman et al. 1994; Lytton 1995; Kolisoja 1997; Rahim and George 2005) or through the fitting parameters themselves.

Laboratory protocols that impose independent cyclic control of confining and deviatoric stresses generate information-rich data that permit the determination of cross-isotropic elastic parameters (Adu-Osei 2000; Adu-Osei et al. 2001b; Kim 2004). All cross-isotropic parameters can be extracted from variable confinement cyclic triaxial tests at multiple states of stress. Typically, the same constitutive model is selected to represent the axial, radial and shear moduli. In particular, the model proposed by Uzan (1985) has been used to model the axial, radial and shear resilient moduli of unbound aggregates in anisotropic pavement analyses (Tutumluer 1995; Tutumluer and Barksdale 1995; Tutumluer and Thompson 1997; Adu-Osei 2000; Adu-Osei et al. 2001a; Adu-Osei et al. 2001b; Tutumluer et al. 2003; Tutumluer and Seyhan 2003; Kim 2004).

4.4. Model Selection

The material model selected to capture the stress-dependent stiffness must be able to predict experimental measurements while satisfying physical constraints. Models with more parameters have more degrees of freedom and can better fit the data; this has lead to the development of increasingly more complex models. However, a better fit does not necessarily imply better prediction capability. These observations are discussed next.

4.4.1. Guiding Criteria

Robust model predictions start with the physically-guided selection of a good material model, following experimental observations and physical principles reviewed above. In addition, fundamental concepts from information theory must be considered during the selection of a robust model (details in Santamarina and Fratta 2005). In particular:

1. *Ockham's Razor*: "plurality should not be assumed without necessity." The number of unknowns in a model should only be increased if its predictions are significantly more accurate for multiple data sets. If two models offer the same level of accuracy, the model with the least number of parameters should be favored to improve predictability.
2. *Physical criteria*: physical insight (i.e., the resilient behavior of granular materials) must guide the analytical form of the model (e.g., linear, exponential, or power law), help in limiting the number of unknowns, and provide physical constraints to the range of values material parameter can take.
3. *Predictability*: a properly selected and calibrated material model must predict future behavior. A n-1 polynomial can perfectly fit n-data points; however, high-order terms

provide marginal insight on the physical laws that govern the measured response. Conversely, lower-order polynomials follow dominant trends, filter data noise, and extract the most meaningful information conveyed by the data. As a result, new data will most likely appear closer to the low-order polynomial model predictions, particularly when the model is used to extrapolate beyond the range of calibration data (figure 4.3).

The introduction of physically meaningless parameters in the pursuit of error minimization has clouded physical understanding of the material response and has lead to the emergence of models that have more parameters than those that can be retrieved from even the best instrumented laboratory tests available today. Furthermore, additional information, such as physical constraints, is often available and must be taken into consideration during model calibration. We focus on the physics-guided selection of a sound and robust mathematical model and the development of parameter inversion methods that go beyond error minimization to ensure the development of a physically meaningful and predictive constitutive model.

4.4.2. Selected Model

We want the selected constitutive model to capture (1) the Hertzian-type stress-dependent stiffness of granular bases and (2) the skeletal softening caused by deviatoric loads that approach failure. The model initially proposed by Huurman (1996) and latter modified by Van Niekerk et al. (2002) satisfies these two fundamental criteria:

$$E_R = k_1\left(\frac{p}{p_0}\right)^{k_2}\left[1-k_3\left(\frac{q}{q_f}\right)^{k_4}\right] \qquad 4.2$$

This non-linear elastic model consists of two stress terms and four fitting parameters, where p_o is a normalizing stress, k_1 is the resilient modulus at $p = p_o$ and $q = 0$, $k_2 > 0$ captures the sensitivity of the resilient modulus to the mean stress, and $k_3 > 0$ and $k_4 > 0$ combine to capture skeletal softening induced by the deviator stress q in reference to the proximity to the failure load q_f. The k_2-exponent is analogous to the β-exponent in equation 4.1.

4.4.3. Fitting the Model to Data – Parameter Inversion

We invert the material parameters k_1, k_2, k_3 and k_4 based on the analysis of the error surface and physical constraints. In this case, the error surface exists in 5D, where the sum of the square errors is $L_2 = \sum e_i^2$. Here e_i is the error between the i-th measured and predicted value and is plotted as a function of k_1, k_2, k_3 and k_4 assumed values. We visualize the error surface by plotting 2D slices across the point of minimum error (min-L_2). The shape of these slices indicates the sensitivity of the fit to the variation of a parameter and permits the reduction of unknowns.

Guidance for the determination of physically meaningful k_2-values can be found in the elastic wave velocity literature where $k_2 \approx 2\beta$ (refer to equation 4.1 - Kopperman et al. 1982, Hardin and Blandford 1989, Santamarina et al. 2001). We conclude that the values of k_2 can range from $k_2 = 0$ for cemented soils to $k_2 = 1.5$ in soils whose response is strongly influenced by electrical interactions. In the case of unbound aggregates used for pavement bases and sub-bases, expected values can be found in the range from $k_2 = 0$ for cement-treated bases to 0.5 for rough/angular aggregates.

The deviatoric stress softening effect is controlled with k_3 and k_4. At $q = q_f$, the material reaches failure and the stress softening term reduces to 1-k_3; thus, physically

meaningful values of k_3 are in the range from k_3= 0 (no-softening) to k_3= 1(flow at failure). The k_4 parameter captures the softening sensitivity of the material for a given deviatoric stress amplitude. Stiffness diminishes linearly with deviatoric loading if k_4= 1. Typically, the effect of deviatoric loading is low when $q<<q_f$ and increases as the material approaches failure, therefore $k_4 > 1$.

4.4.4. Failure Conditions

Resilient behavior is by definition elastic, yet the limiting failure strength q_f is recognized in the model (equation 4.2). Furthermore, numerical results must be carefully examined to confirm that the modeled loads have caused a state of stresses within the aggregate base that is compatible with failure conditions. Here the Drucker-Prager failure criterion is applied to determine the boundary between elastic and perfectly plastic deformations. The failure surface f is a function of the material strength parameters, i.e., friction angle ϕ and apparent cohesion c. The onset of plastic deformation or failure surface is defined by $f = 0$. The material remains in the elastic regime as long as $f < 0$ and deforms plastically for $f = 0$. Thus, the state of stresses at failure is given by:

$$q_f = \frac{6\cos\phi}{3-\sin\phi} c + \frac{6\sin\phi}{3-\sin\phi} p \qquad 4.4$$

4.5. Calibration Examples

The selected constitutive model is used to model published experimental results gathered in triaxial tests under both constant and variable confinement.

4.5.1. Constant Confinement Cyclic Triaxial Data Analysis

Stress-strain data were measured using 0.30m high 0.15m diameter, well graded crushed Georgia granite specimens (Tutumluer 1995). The test protocol consisted on applying a confining pressure σ_c and cyclically loading the specimen in the axial direction up to a preselected deviatoric stress level $\Delta\sigma_z$. The resilient modulus in the axial direction E_{Rz} was calculated by dividing the applied deviator stress amplitude by the measured axial elastic strain ε_z, thus: $E_{Rz} = \Delta\sigma_z / \varepsilon_z$. The test was repeated at five different confining pressures σ_c under three different levels of cyclic deviator stress $\Delta\sigma_z$ each. The data are presented in figure 4.4 in terms of E_{Rz} versus the peak cyclic deviator stress $q=\Delta\sigma_{z\text{-}max}$.

The inversion of material parameters and the construction of the error surface were done using the L_2-norm as described above. Slices of the error surface are shown in figure 4.5. The dotted curve is obtained by controlling k_2 and optimizing k_1 (while $k_3=k_4=0$). The relatively flat trend for the dotted line (e.g., between $k_2= 0.5$ and $k_2= 0.7$) shows a trade-off between k_1 and k_2. Slices of the error surface are obtained by setting k_1 constant and varying the value of k_2 (continuous line) or by holding k_2 constant while varying k_1 (dashed line). The k_1 and k_2 values that minimize the L_2 norm are shown at the intersection between curves in figure 4.5b. Figure 4.5c and figure 4.5d show slices of the error surface across min-L_2; steep slopes near optimum indicate high predictability.

Knowing the upper bound of physically meaningful values for k_2, we set $k_2= 0.5$ and determine the corresponding value of $k_1= 30$MPa. Having determined k_1 and k_2 we introduce the deviatoric stress factor ($k_3\neq0$, $k_4\neq0$) to fine-tune the model using a similar

analysis of the error surface and obtained k_3=0.9 and k_4=16. We call this approach "physically constrained optimization" (PCO).

Alternatively, we find the set of unconstrained parameters solely on the basis of error minimization i.e., "min-L_2" approach. The two sets of parameters are listed in table 4.3; measured and predicted values are compared in figure 4.6. In this case, the two approaches provide adequate fitting of the data and parameters in min-L_2 approach are within physically acceptable ranges.

4.5.2. Variable Confinement Cyclic Triaxial Data Analysis

Variable confinement cyclic triaxial test results from a 0.15m high 0.15m diameter well graded crushed California granite specimens are analyzed next (ICAR 502 series - comprehensive study on anisotropic behavior of aggregates used as bases in flexible pavements - Adu-Osei 2000, Adu-Osei et al. 2001a, and Adu-Osei et al. 2001b). The ICAR protocol employs three triaxial stress regimes: triaxial compression, triaxial extension, and triaxial shear. The ICAR data reduction and analysis of the test results was conducted using a system identification algorithm that considers all the applied stresses and corresponding strains to invert the five cross-isotropic elastic material properties: the modulus in the axial direction E_{Rz}, the modulus in the isotropic plane E_{Rp}, the shear modulus in the anisotropic plane G*, the Poisson's ratio in the isotropic plane υ_{pp}, and the Poisson's ratio in the anisotropic plane υ_{zp}.

We adopt the same constitutive model for E_{Rp}, E_{Rz} and G* (equation 4.2). Resilient axial, radial, and shear moduli data are presented in figure 4.7 as a function of the mean and deviatoric stress *p* and *q*. Following the analysis outlined in the previous section, the resulting error surface sections for the axial resilient modulus data are

presented in figure 4.8, for the radial resilient modulus data in figure 4.9, and for the shear resilient modulus in figure 4.10. The corresponding material parameters recovered using error minimization and the proposed physically constrained optimization are listed in table 4.3. A comparison of the fit quality achieved with the two methods is shown in figure 4.11. The following observations can be made:

- There is a trade-off between k_1 and k_2 (or k_5 - k_6, or k_9 - k_{10}); in other words, the data can be fitted equally well with a "low k_1 and high k_2" or with a "high k_1 and low k_2" combination (figures 4.5-b, 4.8-b, 4.9-b and 4.10-b)
- The optimal set of parameters at the min-L_2 leads to k_2, k_6, and k_{10} exponents higher than the physically justifiable ~0.5 value.
- When the inversion is physically constrained on exponents k_2, k_6, and k_{10}, then the sensitivity of the deviatoric load is properly captured: (a) exponents k_4, k_8, and k_{12} are significantly greater than 1.0, and (b) factors k_3, k_7, and k_{11} are in the range $0 \leq k \leq 1$. Conversely, unconstrained optimization using min-L_2 leads to physically inadequate values.

4.6. Discussion

The complexity of a selected model in terms of number of parameters must be compatible with the physical behavior of the material and the richness of information contained in the experimental measurements used for calibration. In particular, complex models based on a large number of physically void parameters calibrated using inaccurate and/or information poor experimental measurements result in the inability of the model to

predict behavior, especially beyond the conditions from which it was originally developed.

The analysis of the error surface shows that the selection of parameters merely on the basis of numerical error optimization and min-L_2 is unjustified given that multiple sets of values give similarly good fits within the data range. Physical understanding of the material behavior must be used to guide model selection and to constrain model parameters. The two crushed granite samples analyzed above showed strikingly similar E_{Rz}-p response (figure 4.12-a). Yet, independent analyses of the experimental data reported in the original studies (Tutumluer 1995; Adu-Osei et al. 2001b) resulted in very different constitutive parameters while using the same constitutive model, as summarized in table 4.4. The calibrated constitutive models using error minimization provide an excellent fit to each of the individual data sets; however, this does not imply that the calibrated models are capable of accurately predicting material behavior beyond the tested conditions. In particular, figure 4.12-b shows the predicted material response and the data range, in comparison to the stress range in a conventional flexible pavement and in an inverted base pavement. Predictions based on the model and parameters in table 4.4 and the model in equation 4.2 (PCO parameters in table 4.3) are very similar when the mean stresses is below 180kPa; however, at higher stresses, which are typical in inverted base pavements, predictions diverge considerably. The onset of divergence in the predictions coincides with the highest mean stress tested in the laboratory characterization of the aggregate.

4.7. Conclusions

The blind use of error minimization algorithms in combination with constitutive models with a large number of parameters that lack physical meaning hamper the ability of available models to predict material behavior beyond the range of stresses used during characterization.

A comprehensive understanding of the resilient behavior of granular materials has been used to guide the selection of a robust constitutive model (equation 4.2) capable of reproducing the non-linear resilient response of unbound aggregate layers under loading. The selected model captures the effect of mean stress and skeletal softening when deviatoric loads approach failure.

Fundamental concepts in information theory have been used to develop a robust inversion method for the material parameters based on the L_2 error surface analysis. Value selection is guided by physical constraints to improve predictability. We conclude that the values of k_2 can range from $k_2 = 0$ for cement-treated bases to $k_2 \approx 0.5$ for rough/angular aggregates. The deviatoric stress softening effect is controlled with k_3 and k_4. Physically meaningful values of k_3 are in the range from $k_3 = 0$ (no-softening) to $k_3 = 1$ (flow at failure). The k_4 parameter captures the softening sensitivity of the material for a given deviatoric stress amplitude. The effect of deviatoric loading increases as the material approaches failure, therefore $k_4 > 1$.

The selected constitutive model is calibrated following the proposed physically constrained optimization method to capture the experimental response of two crushed granite aggregates from different geographic locations, and characterized using different laboratory test protocols in independent studies. While published predictions are adequate

for stress levels within the range of the experimental data, predicted values for the stress range relevant to inverted pavements can deviate in almost 100% or more depending on the selected model and inversion approach.

Table 4.1 Notation

γ :	Total unit weight	p :	Mean normal stress
γ_w :	Water unit weight	p_o :	Normalization stress
γ_d :	Dry unit weight	q :	Deviatoric stress
Ψ :	Suction induced stress	q_f :	Deviatoric stress at failure
ϕ:	Friction angle	J_2 :	Second deviatoric stress invariant
τ_{oct} :	Octahedral shear stress	w :	Gravimetric water content
υ :	Poisson's ratio	h_m :	Matric suction
ω :	Volumetric water content	n :	Porosity
E_R :	Resilient modulus	n_{max} :	Maximum porosity
k_i :	Model parameters (i =1,2,3,…)	#200:	Fraction of aggregate smaller than 75μm
G :	Shear modulus	C_u :	Coefficient of uniformity
σ_1 :	Major principal stress	C :	"Cohesion"
σ_3 :	Minor principal stress	S :	Degree of saturation
R :	Stress/strength	EC :	Compaction energy

Stress functions:

$$p = \tfrac{1}{3}(\sigma_1 + 2\sigma_3)$$

$$q = \sigma_1 - \sigma_3$$

$$\tau_{oct} = \tfrac{1}{3}\left[(\sigma_1 - \sigma_2)^2 + (\sigma_2 - \sigma_3)^2 + (\sigma_3 - \sigma_1)^2\right]$$

$$J_2 = \tfrac{1}{6}\left[(\sigma_1 - \sigma_2)^2 + (\sigma_2 - \sigma_3)^2 + (\sigma_3 - \sigma_1)^2\right]$$

Table 4.2 Review of available constitutive models (see table 4.1 for notation).

Models	**References**
$E_R = k_1 \left(\frac{\sigma_3}{p_o} \right)^{k_2}$	(Monismith et al. 1967)
$E_R = k_1 \left(\frac{p}{p_o} \right)^{k_2}$ *Material* — Parameter k_1 [MPa] — Exponent k_2 [ ] *Silty sands* — 11.2 (±*5.4*) — 0.62 (±*0.13*) *Sand gravel* — 30.9 (±*29.7*) — 0.53 (±*0.17*) *Sand blend* — 30.0 (±*18.1*) — 0.59 (±*0.13*) *Crushed stone* — 49.7 (±*51.7*) — 0.45 (±*0.23*)	(Brown and Pell 1967; Seed et al. 1967; Hicks 1970; Rada and Witczak 1981)
$E_R = k_1 + k_2 S + k_3 (EC) + k_4 \log p$	(Rada and Witczak 1981)
$E_R = p_o k_1 \left(\frac{p}{p_o} \right)^{k_2} \left(\frac{q}{p_o} \right)^{k_3}$ $E_R = p_o k_1 \left(\frac{p}{p_o} \right)^{k_2} \left(\frac{\tau_{oct}}{p_o} + 1 \right)^{k_3}$	(Uzan 1985)
$E_R = k_1 \left(\frac{J_2}{\tau_{oct}} \right)^{k_2}$	(Johnson et al. 1986)
$E_R = k_1 \left(\frac{p}{q} \right)^{k_2}$	(Thom and Brown 1988)
$E_R = k_1 \left(\frac{\left(p / p_o \right)^{k_2}}{10^{k_3 R^3}} \right)$	(Elliott and Lourdesnathan 1989)
$E_R = \frac{p}{q}(k_1 + q k_2)$ (for CCT) $E_R = \frac{p}{\sigma_1}(k_3 + q k_4)$ (for VCT)	(Nataatmadja and Parkin 1989; Nataatmadja 1992)
$E_R = k_1 \left(\frac{p + \Psi\omega}{p_o} \right)^{k_2} \left(\frac{\tau_{oct}}{p_o} \right)^{k_3} \left(\frac{\gamma}{\gamma_w} \right)^{k_4}$	(Crockford et al. 1990; Kim 2007)

$E_R = k_1 p_0 \left(\frac{p - \omega \cdot j \cdot h_m}{p_{atm}} \right)^{k_2} \left(\frac{\tau_{oct}}{p_{atm}} \right)^{k_3}$	(Lytton 1995)
$E_R = k_1 \left(\frac{\left(q / p_o \right)^{k_2}}{\left(\sigma_3 / p_o \right)^{k_3}} \right)$	(Pezo 1993)
$E_R = k_1 + k_2 C + k_3 \sigma_1 \tan\phi + k_4 p$	(Zaman et al. 1994)
$E_R = k_1 (n_{\max} - n) p_o \left(\frac{p}{p_o} \right)^{0.5}$ $E_R = k_2 (n_{\max} - n) p_o \left(\frac{p}{p_o} \right)^{0.7} \left(\frac{q}{p_o} \right)^{-0.2}$	(Kolisoja 1997)
$Log \left(\frac{E_R}{p_o} \right) = k_1 + k_2 \left(\frac{\sigma_3 - 3k_6}{p_o} \right) + k_3 \left(\frac{p}{p_o} + k_7 \right)$	(Andrei 1999)
$E_R = k_1 \left(\frac{p}{p_o} \right)^{k_2} \left[1 - k_3 \left(\frac{q}{q_f} \right)^{k_4} \right]$	(Van Niekerk et al. 2002)
$E_R = k_1 p_{atm} \left(\frac{p}{p_{atm}} \right)^{k_2} \left(\frac{\tau_{oct}}{p_{atm}} + 1 \right)^{k_3}$	(ERES 2004)
$E_R = k_1 p_o \left(1 + \frac{\left(p / p_o \right)}{1 + \left(q / p_o \right)} \right)^{k_2}$	(Rahim and George 2005)

Table 4.3 Comparison of results from material parameter inversion methods. Data reported in the literature for crushed Georgia and California granite are used to calibrate selected models following the proposed physically constrained optimization method (PCO) and least-squares inversion ("min-L_2"). See table 4.1 for notation.

Material	**Model**	**Model Parameters**	
		PCO	**"min L_2"**
Crushed Georgia granite (data in Tutumluer 1995)	*Non-linear isotropic elasto-plastic:* $E_{Rz} = k_1\left(\frac{p}{p_0}\right)^{k_2}\left[1-k_3\left(\frac{q}{q_f}\right)^{k_4}\right]$ $q_f = \left(\frac{6\sin\phi}{3-\sin\phi}\right)p + \left(\frac{6\cos\phi}{3-\sin\phi}\right)C$ ν = constant; p_o = 1kPa	k_1 = 30MPa k_2 = 0.5 k_3 = 0.9 k_4 = 16 ϕ= 40 L_2 = 63MPa	k_1 = 22MPa k_2 = 0.61 k_3 = 0.16 k_4 = 3.24 ϕ= 40 L_2 = 36MPa
Crushed California granite (data in Adu-Osei et al. 2001b)	*Non-linear cross-isotropic elasto-plastic:* $E_{Rp} = k_1\left(\frac{p}{p_0}\right)^{k_2}\left[1-k_3\left(\frac{q}{q_f}\right)^{k_4}\right]$ $E_{Rz} = k_5\left(\frac{p}{p_0}\right)^{k_6}\left[1-k_7\left(\frac{q}{q_f}\right)^{k_8}\right]$ $G^* = k_9\left(\frac{p}{p_0}\right)^{k_{10}}\left[1-k_{11}\left(\frac{q}{q_f}\right)^{k_{12}}\right]$ $q_f = \left(\frac{6\sin\phi}{3-\sin\phi}\right)p + \left(\frac{6\cos\phi}{3-\sin\phi}\right)C$ ν_{zp} = constant ν_{pp} = constant p_0= 1kPa	k_1 = 12.6MPa k_2 = 0.5 k_3 = 0.9 k_4 = 6 k_5 = 30MPa k_6 = 0.5 k_7 = 0.9 k_8 = 16 k_9 =8.5 k_{10} = 0.5 k_{11} = 0.9 k_{12} = 15 ν_{pp}= 0.37 ν_{zp}=0.17 ϕ= 40 L_2 = 110MPa	k_1 = 8MPa k_2 = 0.901 k_3 = 0.79 k_4 = 0.15 k_5 = 11MPa k_6 = 0.67 k_7 = -1.27 k_8 = 2.08 k_9 = 0.3MPa k_{10} = 0.793 k_{11} = -4.89 k_{12} = -0.1 ν_{pp}= 0.37 ν_{zp}=0.17 ϕ= 40 L_2 = 23MPa

Table 4.4 Material parameters for crushed granite aggregates recovered from error minimization algorithms. Complete material characterization data can be found in the original references. See table 4.1 for notation.

Material / Reference	**Model**	**Material Parameters**
Crushed Georgia granite - axial resilient modulus data from constant confinement triaxial test (Tutumluer 1995)	*Non-linear elastic:* $E_{Rz} = k_1 \left(\frac{3p}{1psi} \right)^{k_2} \left(\frac{q}{1psi} \right)^{k_3}$	k_1 = 4231psi k_2 = 0.645 k_3 = -0.056
Crushed California granite - axial resilient modulus data from variable confinement cyclic triaxial test (Adu-Osei et al. 2001b)	*Non-linear elastic:* $E_{Rz} = k_1 \cdot p_a \left(\frac{3p}{p_a} \right)^{k_2} \left(\frac{\tau_{oct}}{p_a} \right)^{k_3}$ p_a = 100kPa	k_1 = 2934 k_2 = 0.326 k_3 = 0.366

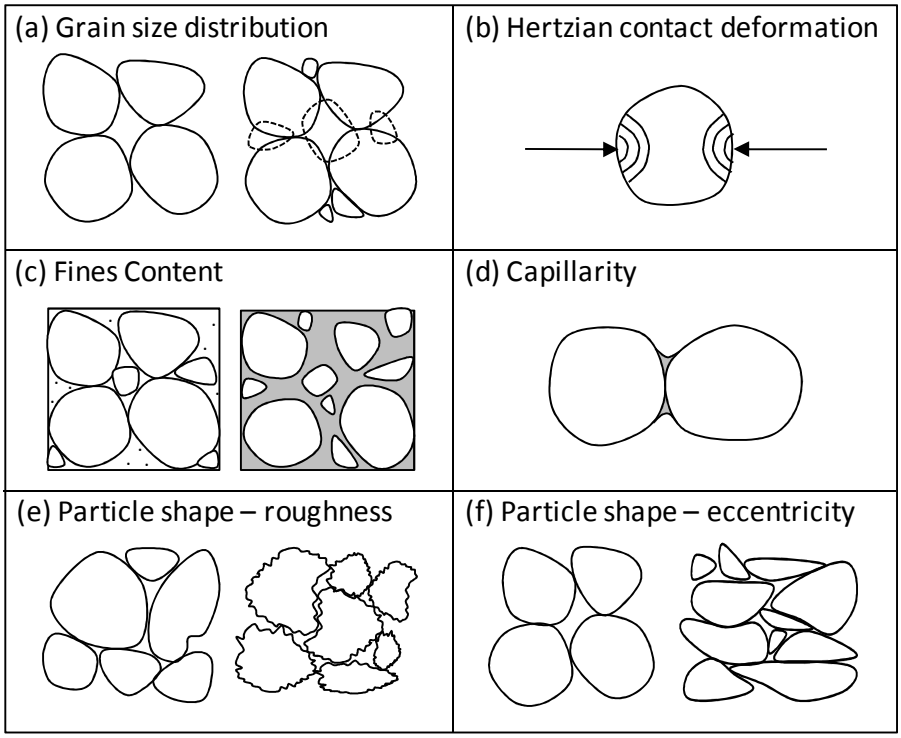

Figure 4.1 Fundamental concepts in granular materials that influence the resilient behavior of unbound aggregate bases.

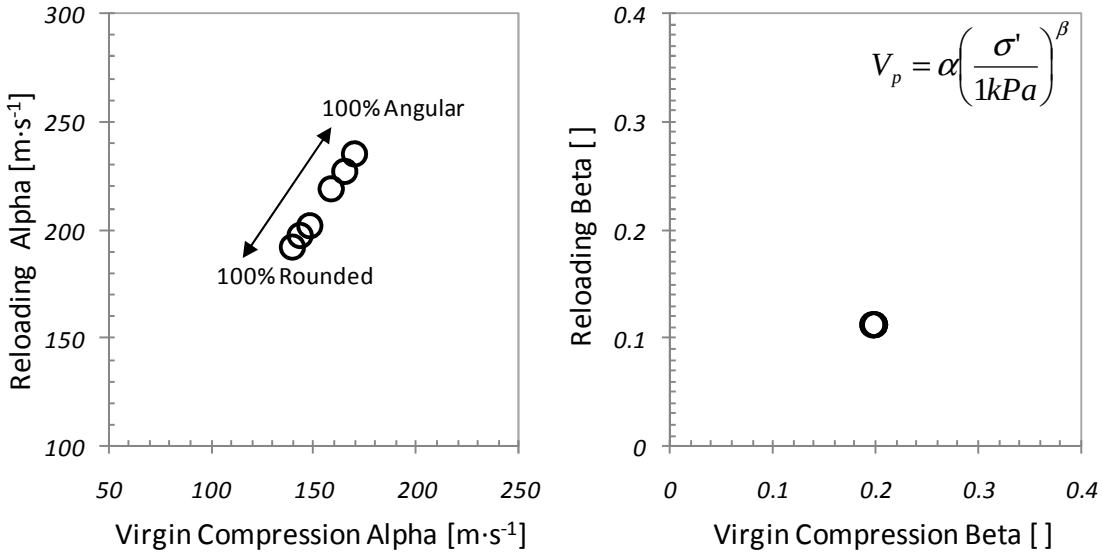

Figure 4.2 Effect of particle shape on the stiffness-stress material parameters under virgin loading and reloading (data from Cho et al. 2006). The alpha and beta parameters fit the model presented in equation 4.1 (also shown in the insert).

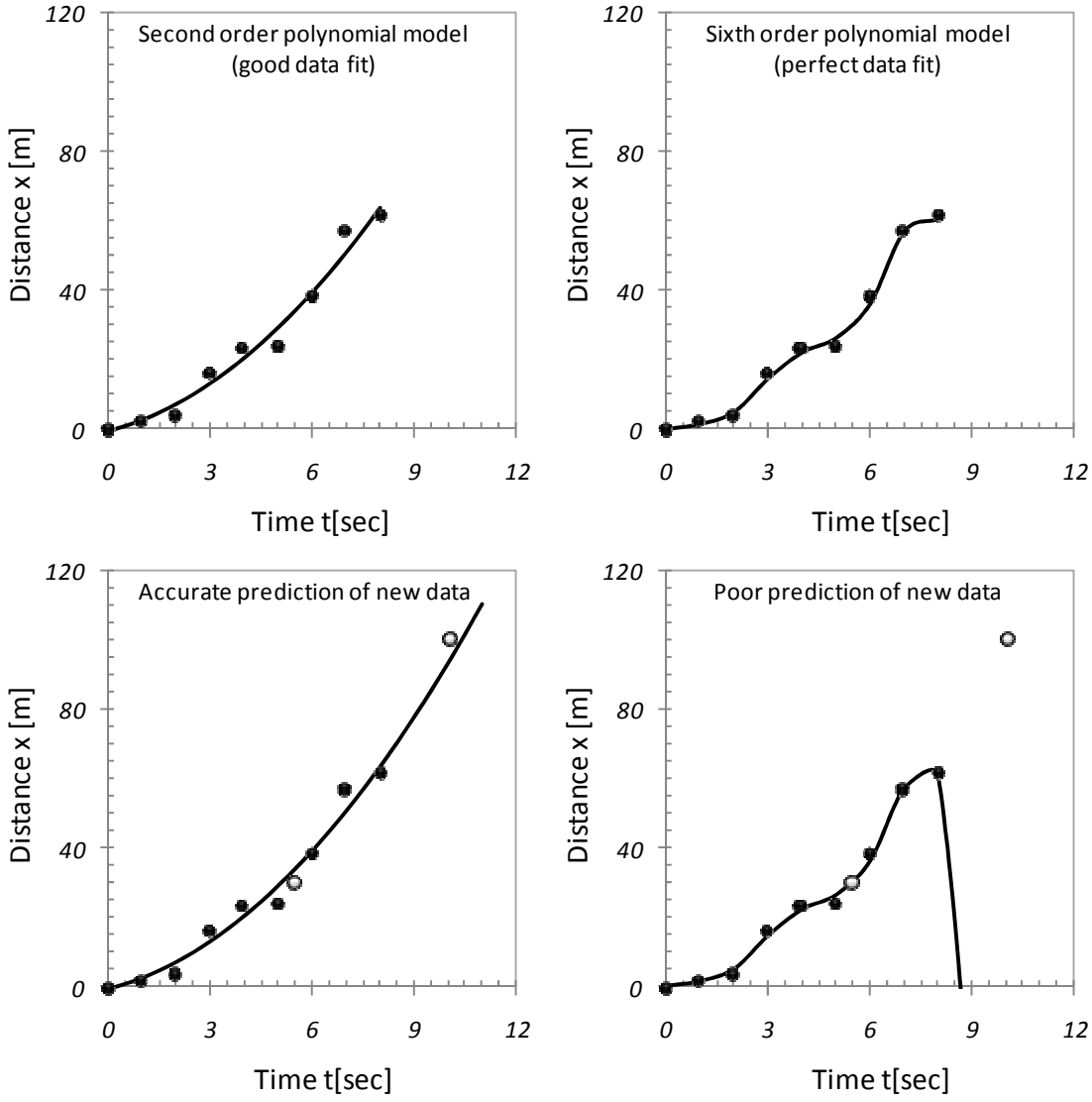

Figure 4.3 The simulated data corresponds to the equation of motion for an accelerating body, $x = \frac{1}{2}at^2$ with random noise. The second and sixth order polynomial coefficients are determined by fitting to the black points. New data are shown as hollow points. Original figure from Santamarina and Fratta (2005).

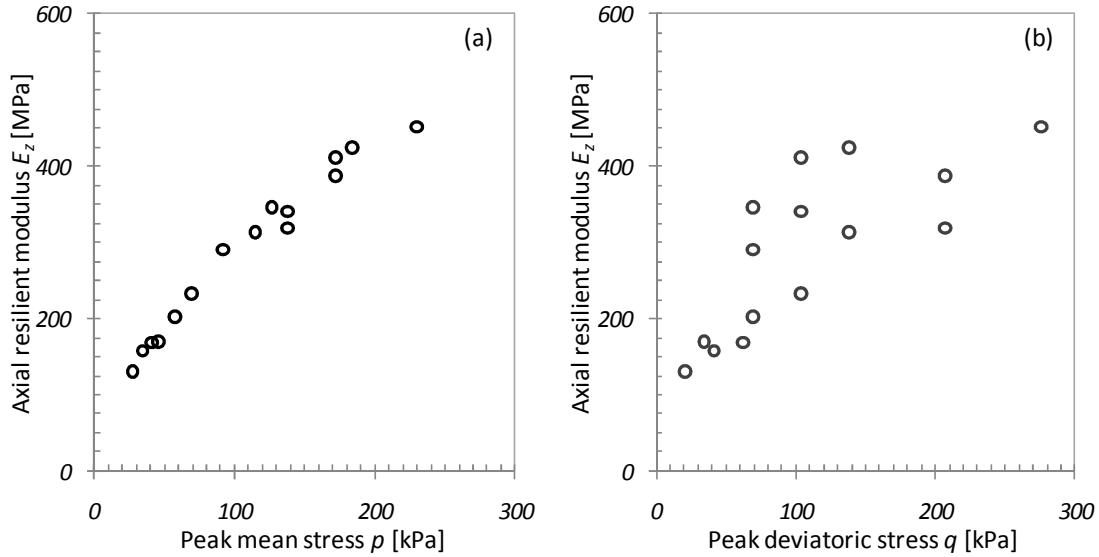

Figure 4.4 Cyclic triaxial at constant confinement test results for crushed granite aggregate (data from Tutumluer 1995). The axial resilient modulus E_z is plotted (a) against the peak mean stress $p=(3\sigma_c+\Delta\sigma_v)$ and (b) the peak deviatoric stress $q=\Delta\sigma_v$.

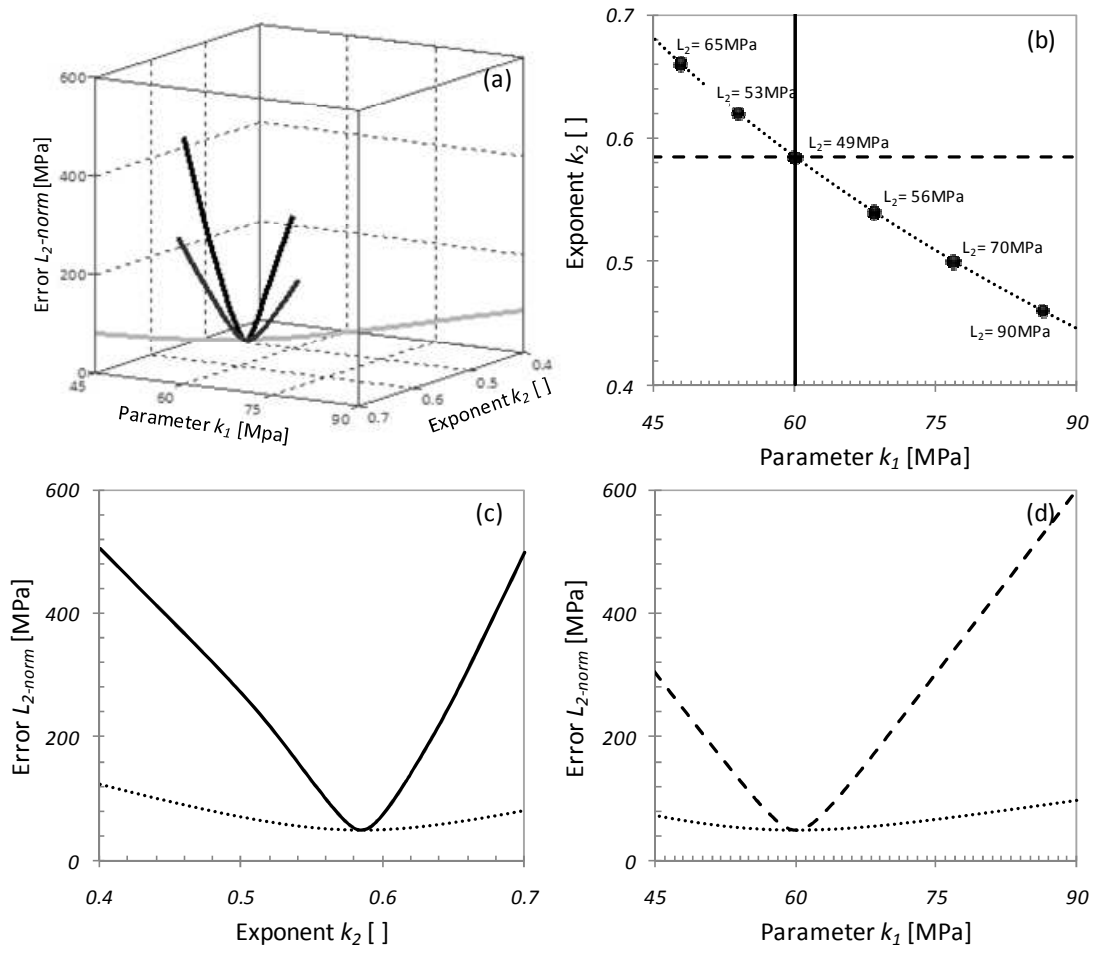

Figure 4.5 Error surface sections obtained while fitting equation 4.2 to axial resilient modulus E_z data in Tutumluer (1995). The optimum values for $k_1$and k_2 are selected by error minimization keeping k_3=k_4=0. The 4 plots show: (a) the error surface in three dimensions, (b) the analyzed errors in k_1–k_2 space (min-L_2 plots at the intersection), (c) a slice of the error surface in the k_2-plane, and (d) a slice of the error surface in the k_1-plane.

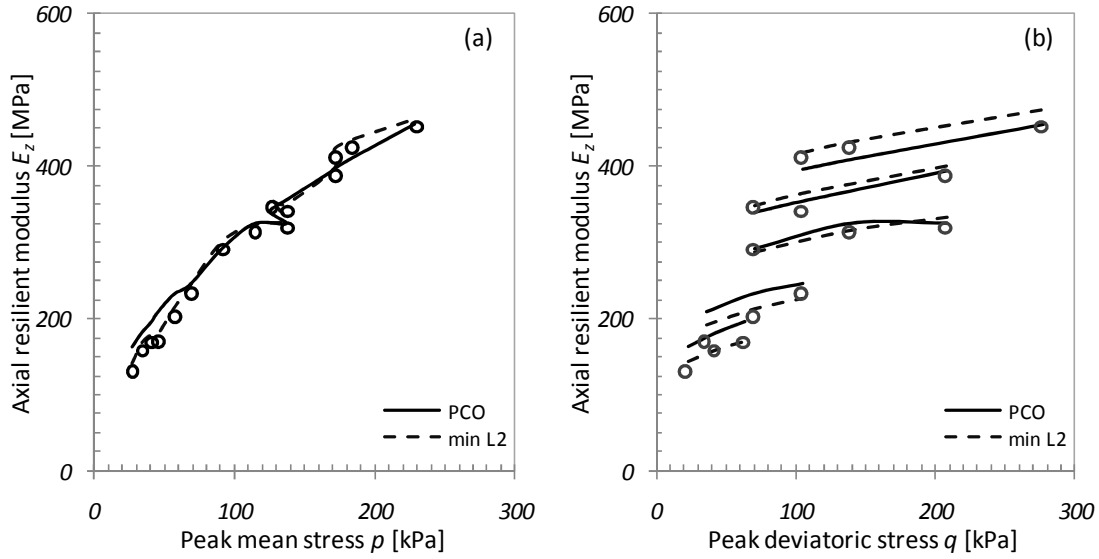

Figure 4.6 Predictions based on the parameters obtained from min-L_2 optimization (dashed line) and physically constrained optimization PCO (continuous) compared against the measured experimental data. The data are from Tutumluer (1995) and the fitted model is presented in equation 4.2. The axial resilient modulus E_z is plotted (a) against the peak mean stress $p=(3\sigma_c+\Delta\sigma_v)$ and (b) the peak deviatoric stress $q=\Delta\sigma_v$.

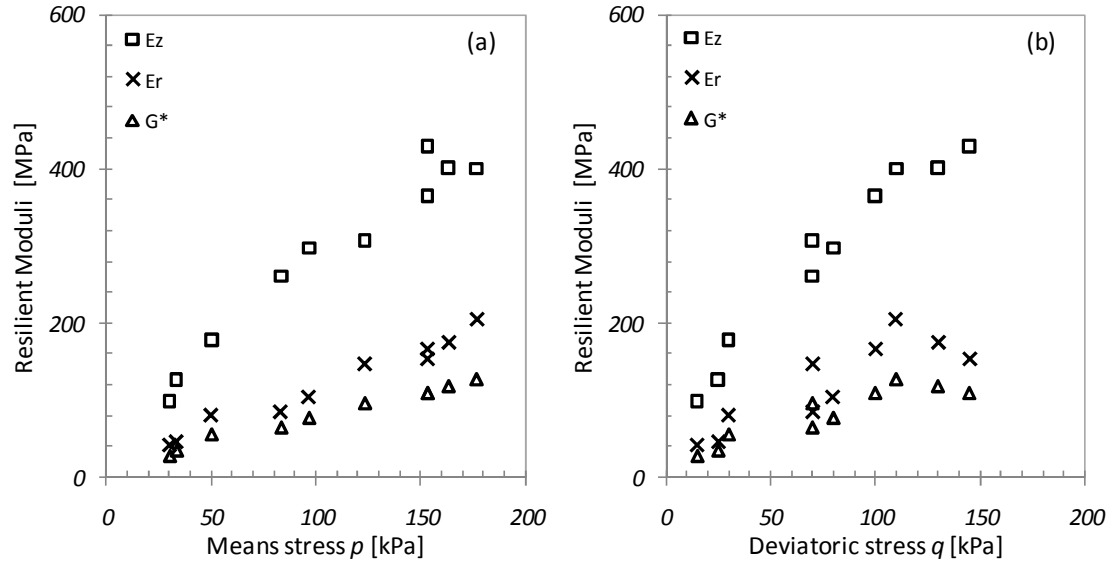

Figure 4.7 Cyclic triaxial under variable confinement. Data for crushed granite aggregate from Adu-Osei et al. (2001b). The axial E_z, radial E_r, and shear G* resilient moduli are plotted (a) against the mean stress $p=(\sigma_1+2\sigma_3)$ and (b) the deviatoric stress $q=\sigma_1-\sigma_3$.

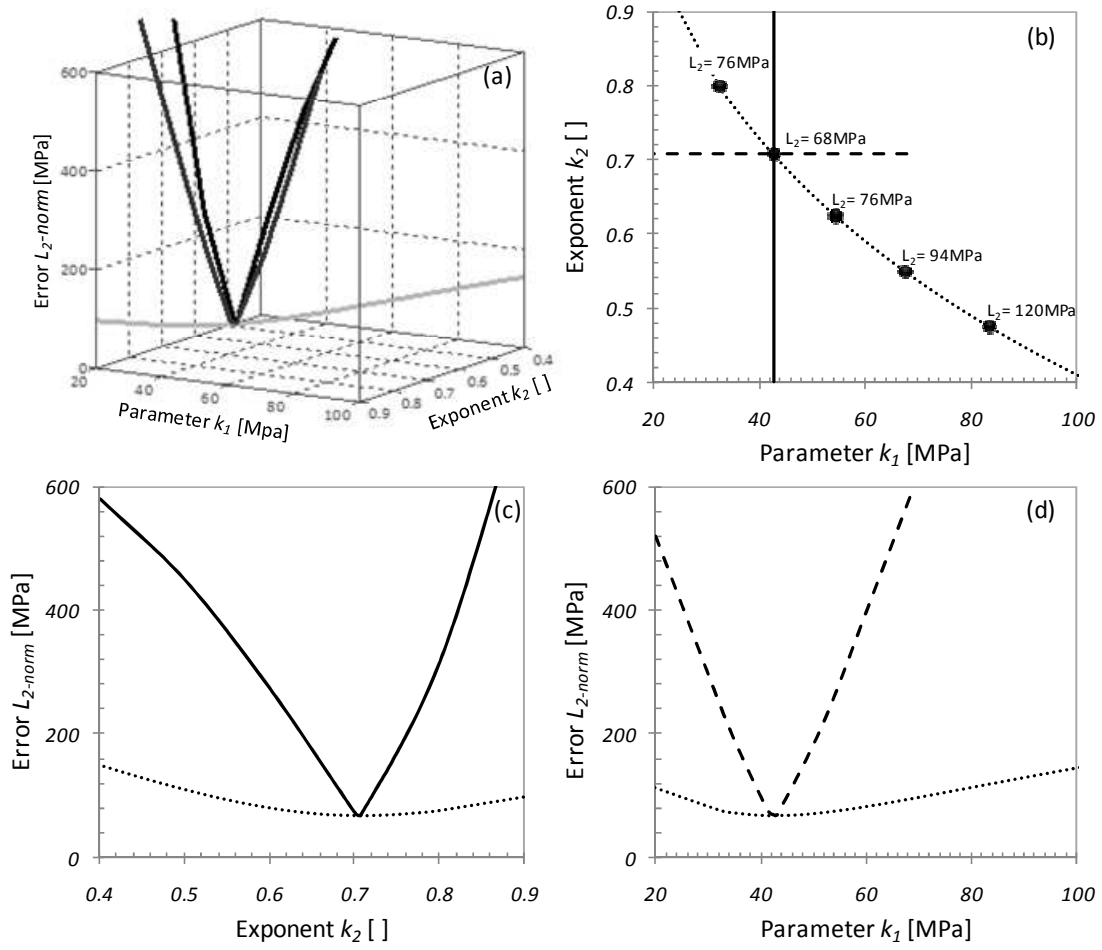

Figure 4.8 Error surface sections obtained while fitting equation 4.2 to axial resilient modulus E_z data in Adu-Osei et al. (2001b). The optimum values for $k_1$and k_2 are selected by error minimization keeping k_3= k_4=0. The 4 plots show: (a) the error surface in three dimensions, (b) the analyzed errors in k_1–k_2 space (min-L_2 plots at the intersection), (c) a slice of the error surface in the k_2-plane, and (d) a slice of the error surface in the k_1-plane.

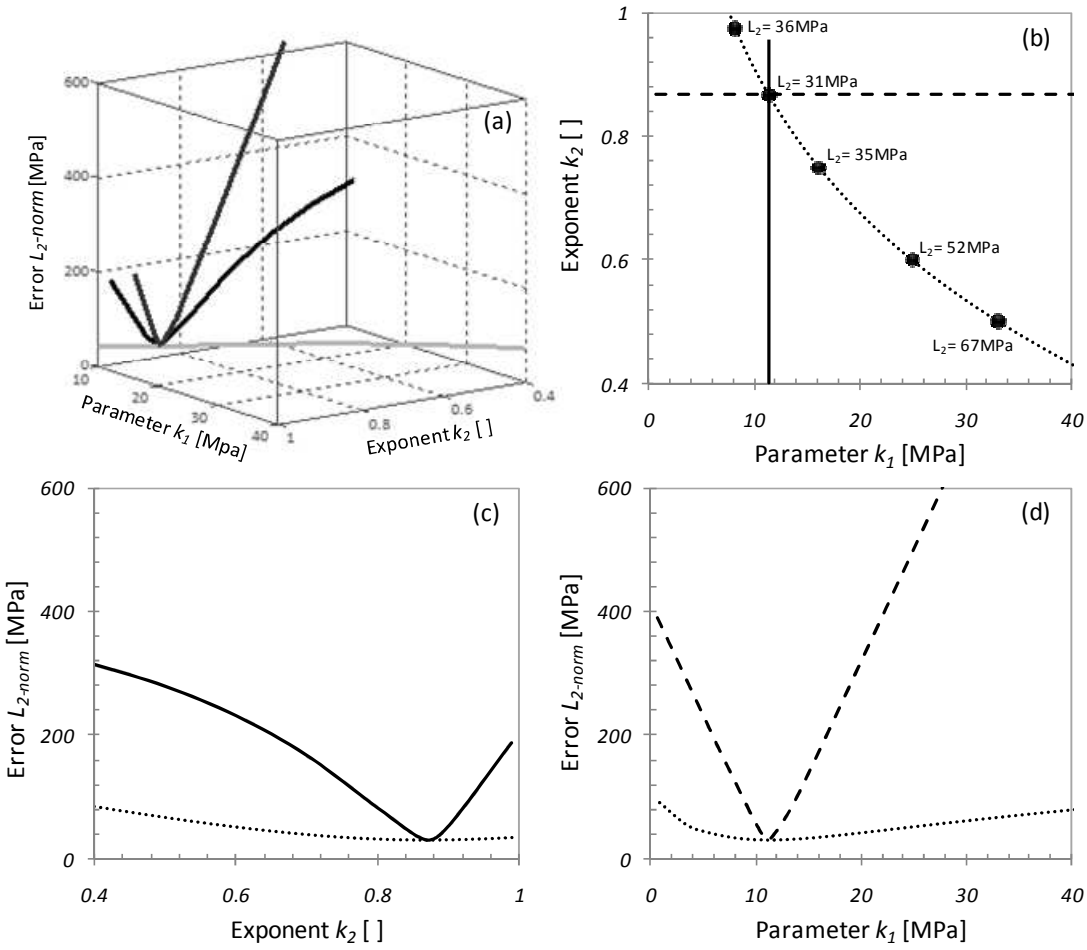

Figure 4.9 Error surface sections obtained while fitting equation 4.2 to radial resilient modulus E_r data in Adu-Osei et al. (2001b). The optimum values for $k_1$and k_2 are selected by error minimization keeping k_3= k_4=0. The 4 plots show: (a) the error surface in three dimensions, (b) the analyzed errors in k_1–k_2 space (min-L_2 plots at the intersection), (c) a slice of the error surface in the k_2-plane, and (d) a slice of the error surface in the k_1-plane.

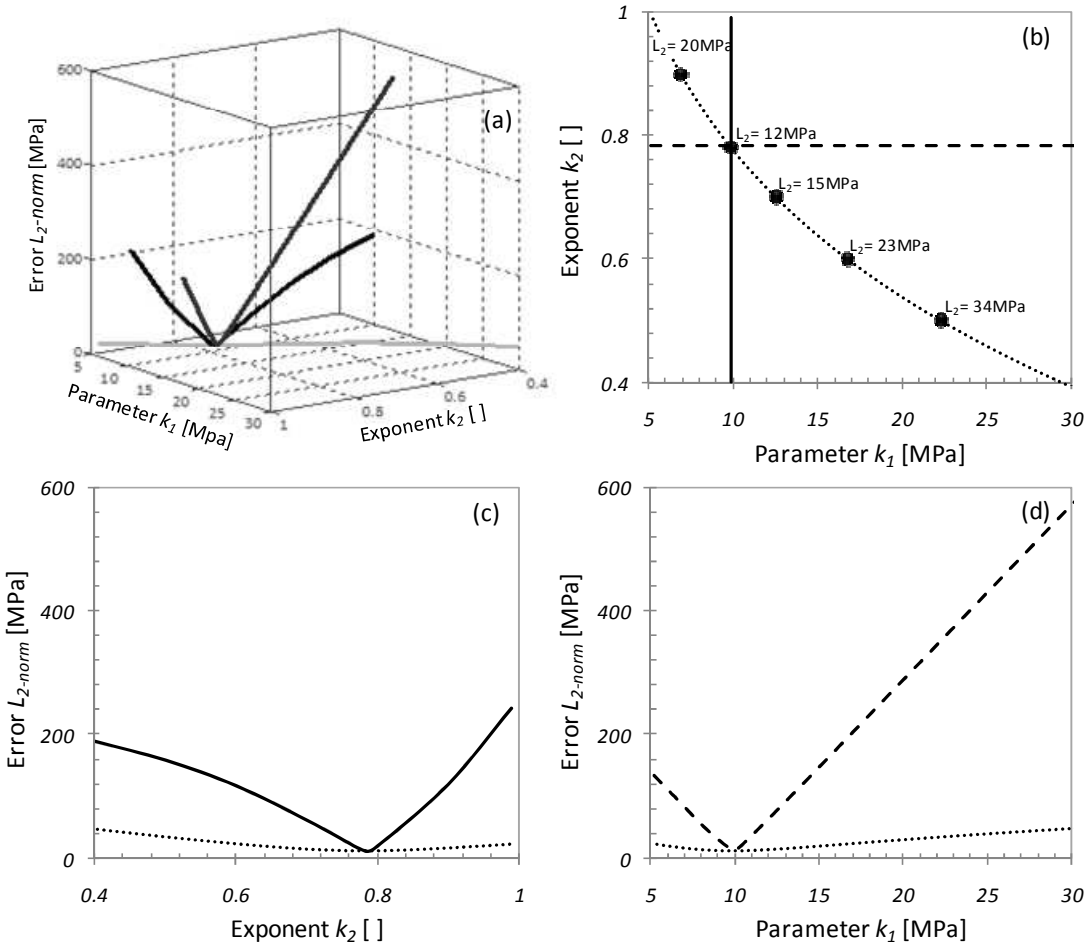

Figure 4.10 Error surface sections obtained while fitting equation 4.2 to shear resilient modulus G* data in Adu-Osei et al. (2001b). The optimum values for $k_1$and k_2 are selected by error minimization keeping k_3= k_4=0. The 4 plots show: (a) the error surface in three dimensions, (b) the analyzed errors in k_1–k_2 space (min-L_2 plots at the intersection), (c) a slice of the error surface in the k_2-plane, and (d) a slice of the error surface in the k_1-plane.

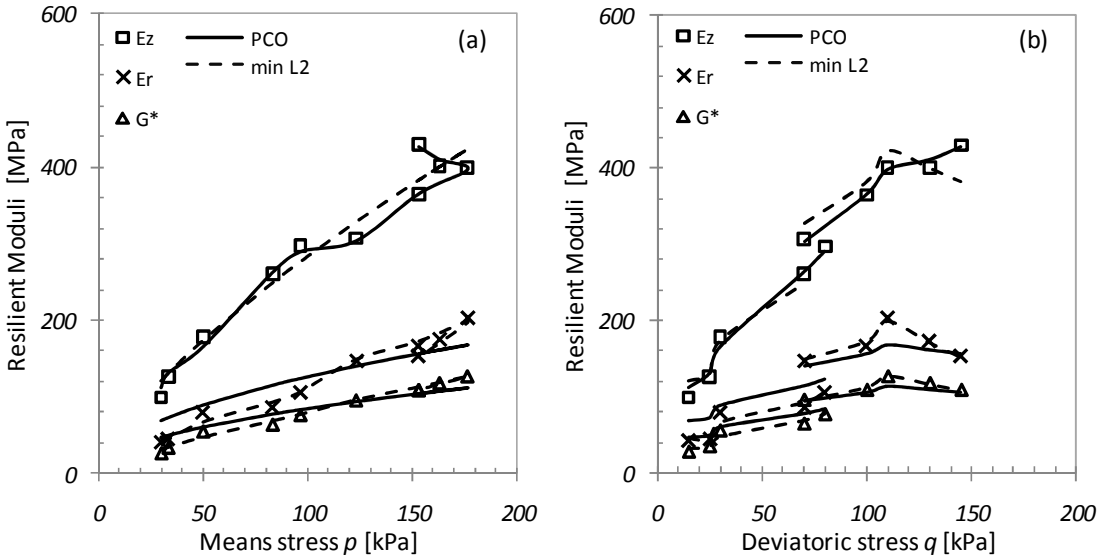

Figure 4.11 Predictions based on the parameters obtained from min-L_2 optimization (dashed line) and physically constrained optimization PCO (continuous) compared against the measured experimental data. The data are from Adu-Osei et al. (2001b) and the fitted model is presented in equation 4.2. The axial E_z, radial E_r, and shear G* resilient moduli are plotted (a) against the mean stress $p=(\sigma_1+2\sigma_3)$ and (b) the deviatoric stress $q=\sigma_1-\sigma_3$.

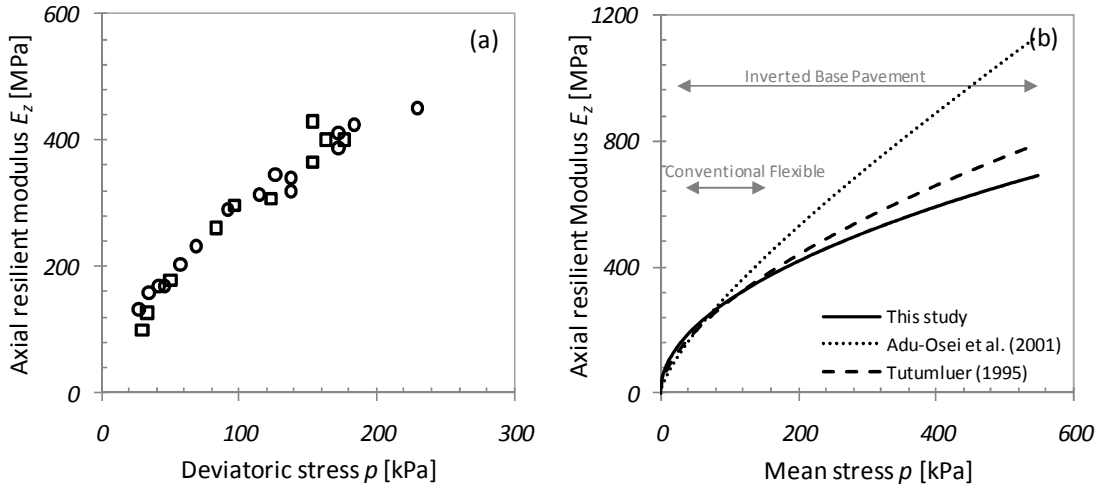

Figure 4.12 Comparison of axial elastic resilient modulus predictions for well graded crushed granite based on the models and parameters documented in the literature and the proposed model and parameter reduction method. (a) data reported by Tutumluer (1995) and Adu-Osei (2001b) and (b) comparison of behavior predictions made based on the reported models and material parameters (table 4.3) and the selected model (equation 4.2) and the proposed physically constrained material parameter inversion method (PCO table 4.3). The range of traffic induced mean stresses expected for conventional flexible pavements and inverted base pavement structures are shown for reference.

CHAPTER 5

NUMERICAL SIMULATION OF INVERTED BASE PAVEMENTS

5.1. Introduction

Pavement analysis and design following the AASHO road test (1956-1961) combines mechanistic theories and empirical relationships. Layered linear and non-linear elasticity concepts guided the development of the AASHTO 1972 interim design guide and its subsequent 1993 revision. More recently, underlying concepts are explicitly recognized in the latest mechanistic-empirical pavement design guide developed under the NCHRP project 1-37A (2002). In this guide, pavement structures are analyzed in two steps. First, the structural response is determined using mechanistic and constitutive material models developed from as-built layer properties, the key results from this analysis are horizontal tensile strains at the bottom/top of the bounded aggregate layers and compressive vertical stresses within the unbound layers. Then, these values are used as input parameters to distress prediction models based on accumulated empirical field data from which the expected pavement life is determined (ERES 2004; Kim 2008).

Inverted base pavements consist of an unbound aggregate base confined by a stiff cement treated sub-base and a thin asphalt cover. Large cyclic stresses develop within the unbound aggregate layer under service loading, which translate into large variations in the resilient modulus of the material. Linear elastic analysis cannot accommodate the stiffness-stress dependency of unbound aggregate layers, and yield erroneous stress and strain predictions in inverted base pavement structures.

The analysis of pavement structures using the finite element method facilitates the incorporation of complex constitutive models that appropriately capture the non-linear behavior of unbound aggregate layers. The use of finite elements in the analysis of pavement structures started in the 1960's and evolved into codes such as GAPPS7, SENOL, ILLI-PAVE, MICH-PAVE, FENLAP, and GT-Pave (Shifley and Monismith 1968; Raad and Figueroa 1980; Brown and Pappin 1981; Barksdale et al. 1989; Harichandran et al. 1990; Brunton and De Almeida 1992; Tutumluer 1995; Park and Lytton 2004). Selected numerical studies summarized in table 5.1 show that codes have been developed for the specific conditions, applicable to conventional flexible pavement structures.

Various general-purpose finite element analysis packages offer the versatility needed for the study of inverted pavements. In particular, the general-purpose finite element program ABAQUS has been used to study pavement conditions such as multiple wheel loads, unbound aggregate non-linear behavior, and anisotropy (Chen et al. 1995; Cho et al. 1996; Hjelmstad and Taciroglu 2000; Sukumaran et al. 2004; Kim et al. 2009). Yet, available built-in material models are not suitable to capture the resilient behavior exhibited by unbound aggregate layers.

This chapter documents the development of an ABAQUS-based code to analyze the response of inverted base pavements, including the numerical implementation of a robust constitutive model for the unbound aggregate layer. The code is used to guide the selection of the domain size, to reveal the implications of simplifying assumptions, and to illustrate key differences in the mechanical performance between inverted base and conventional flexible pavements.

5.2. Pavement Materials: Behavior and Modeling

5.2.1. Asphalt Concrete

The stress-strain behavior of asphalt concrete is determined by the loading frequency, duration and amplitude, temperature, stress state, aging, and moisture (Abbas et al. 2004). Asphalt concrete deforms slowly and permanently at low strain rates and high temperatures, and becomes stiffer and brittle at high strain rates and low temperatures (Kim 2008). The tensile strength and strain at failure depend on both temperature and the fraction of air filled void space. Asphalt concrete strength values reported vary between 3.6 to 5.4MPa at -10°C and 0.9 to 1.6MPa at 21°C; the strain at failure is in the order of 1×10^{-4} to 3×10^{-3} (Underwood et al. 2005; Kim 2008; Richardson and Lusher 2008). Aggregate shape and compaction during construction result in inherent and stress-induced anisotropy; thus, asphalt concrete exhibits cross isotropic material properties (Underwood et al. 2005). The response of asphalt concrete to service load can be represented by a visco-elasto-plastic model (Uzan 2005; Kim et al. 2008).

5.2.2. Cement-Treated Base

The long term behavior of lightly cemented aggregate bases exhibits three distinctive stages: (1) pre-cracked phase, (2) the onset of fatigue cracking, and (3) advanced crushing. During the pre-cracked phase, the layer behaves as a slab with horizontal plane dimensions larger than the layer thickness; the elastic modulus during this stage corresponds to that measured immediately after construction of the pavement structure. At the onset of fatigue cracking, the initial elastic modulus reduces rapidly as the layer brakes down into large blocks with dimensions in the horizontal plane in the

order of magnitude of the layer thickness. Finally in the advanced crushing state, the layer reduces to a granular equivalent with blocks smaller than the layer thickness. At this stage the originally cemented aggregate now behaves non-linearly and with stress-dependent stiffness alike an unbound aggregate (Theyse et al. 1996; Balbo 1997). This evolution in mechanical behavior of the cement-treated base results in rearrangement of stresses and strains within the entire pavement structure. Therefore, while deterioration of the cemented aggregate itself is not considered a critical mode of distress, it has serious implications on the distress evolution of more critical layers, specially the asphalt concrete layer.

5.2.3. Unbound Aggregate Base and Subgrade Layers

Unbound aggregates exhibit inherently non-linear behavior (refer to detailed review in chapter 4). Typically, plastic deformations decrease with the number of load repetitions until only elastic strains are present in the material response, i.e., shake-down. The resilient modulus is defined as the ratio of the cyclic stress amplitude to the recoverable elastic strain. Experimental studies have established that the resilient response of the granular base is controlled by stress level, density, gradation, particle size, maximum grain size, moisture content, stress history, load duration, and load frequency.

The state of stresses has the most significant effect on the resilient response of unbound aggregate bases. In the shake-down regime, the resilient modulus increases with the bulk stress and decrease slightly with increasing amplitude of the repeated deviator stress (Morgan 1966; Hicks and Monismith 1971; Smith and Nair 1973). Dense granular assemblies have high coordination number which lowers the average inter-particle

contact stress under loading. Lower inter-particle contact stresses lead to less grain deformation at contacts which in turn results in higher resilient modulus (Trollope et al. 1962; Hicks 1970; Robinson 1974; Rada and Witczak 1981; Kolisoja 1997). Density effects are more evident at low values of the mean normal stress (Barksdale and Itani 1989). The stiffness of unbound aggregate layers is also affected by capillary forces (Dawson et al. 1996).

The unbound aggregate base stiffness increases with the fines fraction until the granular skeleton becomes fines-dominated; thereafter, the resilient modulus reduces considerably as the mechanical performance is controlled by the fine aggregate properties (Jorenby and Hicks 1986). Crushed aggregates are characterized by rough angular particles that tend to interlock leading to stronger and stiffer granular assemblies when properly compacted (Allen and Thompson 1974; Thom and Brown 1988; Barksdale et al. 1989; Kim et al. 2005). Aggregate shape controls the inherent anisotropy of the unbound aggregate base (Pennington et al. 1997).

5.3. Numerical Simulator

The development of the numerical simulator is described in this section.

5.3.1. User-Defined Material Subroutine

A cross-isotropic non-linear elastoplastic material model is implemented in Fortran and inserted as a subroutine in the commercial finite element software ABAQUS. The subroutine is called at Gaussian points of elements that the user defines with this material behavior. ABAQUS inputs initial stresses, strains, state variables, and the current strain increment at the beginning of each computation time. The subroutine

updates the stresses and solution-dependent state variables and provides the material stiffness matrix (Simulia 2007).

The notation used in this manuscript follows. Underlined lower case letters denote 2nd order tensors, e.g. $\underline{a} = a_{ij}$, here the 2nd order tensor $\underline{1} = \delta_{ij}$ is the kronecker delta. Underlined upper case letters denote 4th order tensors e.g., $\underline{\underline{A}} = A_{ijkl}$, here the $\underline{\underline{I}} = \left(\delta_{ik}\delta_{jl} + \delta_{il}\delta_{jk}\right)/2$ is the unit 4th order tensor. The symbol ':' denotes the inner product of two tensors; thus, $\underline{a} : \underline{b} = a_{ij}b_{ij}$, $\underline{1} : \underline{1} = \delta_{ij}\delta_{ij} = 3$, and $\underline{\underline{A}} : \underline{a} = A_{ijkl}a_{kl}$. Finally, the symbol $\otimes$ denotes the juxtaposition of two tensors e.g., $\underline{a} \otimes \underline{b} = a_{ij}b_{kl}$.

The constitutive equations in linear elasticity are represented by the generalized Hooke's law which can be expressed as $\underline{\sigma} = \underline{\underline{D}}^e : \underline{\varepsilon}$, where $\underline{\sigma} = \sigma_{ij}$ is the stress tensor, $\underline{\varepsilon} = \varepsilon_{ij}$ the strain tensor and $\underline{\underline{D}}^e = D^e{}_{ijkl}$ is the fourth order material stiffness tensor. In cross-isotropic materials the elastic properties in any direction within the plane perpendicular to a certain axis of symmetry are all the same. Consequently, the stiffness matrix reduces to:

$$\underline{\underline{D}}^e = \begin{bmatrix} \frac{E_p\left(E_z - \nu_{zp}{}^2 E_p\right)}{A\left(1+\nu_{pp}\right)} & \frac{E_p\left(\nu_{pp}E_z + \nu_{zp}{}^2 E_p\right)}{A\left(1+\nu_{pp}\right)} & \frac{\nu_{zp}E_pE_z}{A} & 0 & 0 & 0 \\ \frac{E_p\left(\nu_{pp}E_z + \nu_{zp}{}^2 E_p\right)}{A\left(1+\nu_{pp}\right)} & \frac{E_p\left(E_z - \nu_{zp}{}^2 E_p\right)}{A\left(1+\nu_{pp}\right)} & \frac{\nu_{zp}E_pE_z}{A} & 0 & 0 & 0 \\ \frac{\nu_{zp}E_pE_z}{A} & \frac{\nu_{zp}E_pE_z}{A} & \frac{\left(1-\nu_{pp}\right)E_z{}^2}{A} & 0 & 0 & 0 \\ 0 & 0 & 0 & \frac{E_p}{2\left(1+\nu_{pp}\right)} & 0 & 0 \\ 0 & 0 & 0 & 0 & G^* & 0 \\ 0 & 0 & 0 & 0 & 0 & G^* \end{bmatrix}$$

where $A = E_z\left(1-\nu_{pp}\right)-2\nu_{zp}{}^2 E_p$, E_p is the Young's modulus in the isotropic plane p, E_z is the Young's modulus in the z-direction normal to the isotropic plane, G^* is the shear modulus in the *z-p* plane, v_{zp} is the Poisson's ratio for stress applied in the *z*-direction inducing strains in the *p*-direction, v_{pp} is the Poisson's ratio for stress applied in a *p*-direction inducing strains in the *p*-plane.

We incorporate the model proposed by Van Niekerk et al. (2002) to capture the unbound aggregate non-linear resilient elastic behavior (see details in chapter 4)

$$E_{Rp} = k_1\left(\frac{p}{p_0}\right)^{k_2}\left[1-k_3\left(\frac{q}{q_f}\right)^{k_4}\right]$$

$$E_{Rz} = k_5\left(\frac{p}{p_0}\right)^{k_6}\left[1-k_7\left(\frac{q}{q_f}\right)^{k_8}\right]$$

$$G^* = k_9\left(\frac{p}{p_0}\right)^{k_{10}}\left[1-k_{11}\left(\frac{q}{q_f}\right)^{k_{12}}\right]$$

where:

$$p = \frac{1}{3}\underline{\sigma}:\underline{1} \quad , \quad q = \sqrt{\frac{3}{2}\underline{\sigma}':\underline{\sigma}'}\underline{1} \quad \text{and} \quad \underline{\sigma}' = \underline{\sigma} - p\underline{1}$$

and p is the mean stress, q the deviatoric stress, q_f is the deviatoric stress at failure, and k_i are material parameters. The proposed user-defined material subroutine combines cross-isotropic non-linear elasticity and the Drucker-Prager failure criterion to fully characterize the unbound aggregate mechanical response. The plastic behavior is incorporated in the user-defined material subroutine through a continuum tangent modulus formulation. The derivation of the stress-strain relationship and the determination of the stress increment caused by a given strain increment follows:

(1) The stress increment $\dot{\underline{\sigma}}$, is defined in terms of the elastic strain increment $\dot{\underline{\varepsilon}}^{e}$ and the elastic stiffness tensor $\underline{D}^{e}$ according to:

$$\dot{\underline{\sigma}} = \underline{D}^{ep} : \dot{\underline{\varepsilon}} = \underline{D}^{e} : \left(\dot{\underline{\varepsilon}} - \dot{\underline{\varepsilon}}^{p} \right)$$

(2) The Drucker-Prager failure criterion is applied to determine the boundary between elastic and perfectly plastic deformations. Note that the failure surface f is a function of the material strength parameters, i.e., friction angle ϕ and apparent cohesion c. The onset of plastic deformation or failure surface is defined by $f = 0$. The material remains in the elastic regime as long as $f < 0$ and deforms plastically for $f = 0$. Thus, the state of stresses at failure is given by:

$$f = q - (\xi\, p + \chi) = 0 \quad \text{where } \xi = \frac{6\sin\phi}{3 - \sin\phi} \quad \text{and } \chi = \frac{6\cos\phi}{3 - \sin\phi} c$$

$$f = \|\underline{\sigma}'\| - \sqrt{\frac{2}{3}}(\xi\, p + \chi) = 0$$

(3) The plastic deformation on the failure surface is determined by the plastic potential function, g. If the plastic potential function g is equal to the failure function f, the material is said to follow an associated flow rule, otherwise the material follows a non-associated flow rule. The plastic potential function is given by:

$$g = \|\underline{\sigma}'\| - \sqrt{\frac{2}{3}}\left(\xi^{*}\, p\right) = 0 \quad \text{where } \xi^{*} = \frac{6\sin\delta}{3 - \sin\delta}$$

The parameter ξ* defines the rate of mobilized plastic volumetric strain in relation to the driving deviator strain, and it is a function of the dilation angle δ. Plastic strain increments are related to the plastic potential at the state of stresses on the failure surface; thus:

$$\dot{\underline{\varepsilon}}_p = \dot{\lambda}\frac{\partial g}{\partial \underline{\sigma}} = \dot{\lambda}\left(\underline{n} - \frac{\sqrt{2}}{3\sqrt{3}}\xi^*\underline{1}\right)$$

$$\underline{n} = \frac{\underline{\sigma}'}{\|\underline{\sigma}'\|}$$

where the scalar multiplier $\dot{\lambda}$ represents a plastic strain increment in the direction normal to the plastic potential function.

(4) The consistency condition limits the stress state to remain on the failure surface during plastic deformation, never outside. This facilitates the determination of an expression for the scalar multiplier $\dot{\lambda}$ from the differential form of the failure surface:

$$\dot{f}(\underline{\sigma}) = \frac{\partial f}{\partial \underline{\sigma}} : \dot{\underline{\sigma}} = \left(\underline{n} - \frac{\sqrt{2}}{3\sqrt{3}}\xi\underline{1}\right) : \dot{\underline{\sigma}} = 0$$

$$\left(\underline{n} - \frac{\sqrt{2}}{3\sqrt{3}}\xi\underline{1}\right) : \left(\underline{D}^e : \dot{\underline{\varepsilon}} - \underline{D}^e : \dot{\underline{\varepsilon}}^p\right) = 0$$

The scalar multiplier can be determined based on the given strain increment by:

$$\dot{\lambda} = a\left(\underline{n} - \frac{\sqrt{2}}{3\sqrt{3}}\xi\underline{1}\right) : \underline{D}^e : \dot{\underline{\varepsilon}}$$

$$a = \frac{1}{\left(\underline{n} - \frac{\sqrt{2}}{3\sqrt{3}}\xi\underline{1}\right) : \underline{D}^e : \left(\underline{n} - \frac{\sqrt{2}}{3\sqrt{3}}\xi^*\underline{1}\right)}$$

(5) Finally, the elastoplastic stress-strain relationship is given by:

$$\dot{\underline{\sigma}} = \underline{D}^{ep} : \dot{\underline{\varepsilon}} = \left(\underline{D}^e - a\,\underline{b} \otimes \underline{d}\right) : \dot{\underline{\varepsilon}}$$

where

$$\underline{b} = \underline{D}^e : \left(\underline{n} - \frac{\sqrt{2}}{3\sqrt{3}}\xi^*\underline{1}\right) \quad \text{and} \quad \underline{d} = \underline{D}^e : \left(\underline{n} - \frac{\sqrt{2}}{3\sqrt{3}}\xi\underline{1}\right)$$

5.3.2. Mesh Generation and Element Selection

Simple models of the wheel load as a uniformly distributed pressure over a finite area cause an abrupt discontinuity in the stress field at the periphery of the loaded area. A fine mesh size is used in the vicinity of the load discontinuity to appropriately resolve the large stress gradients in this zone. The magnitude of stress and strain gradients decreases away from the load boundary where larger elements are used to optimize computation time without compromising resolution. The mesh used in the simulations is shown in figure 5.2. The 3D-axisymmetric analysis of the pavement structure is conducted using 8-node bi-quadratic axisymmetric quadrilateral elements with reduced integration (ABAQUS-CAX8R type).

5.3.3. Code Verification

The verification of the user-defined material subroutine is done by comparison with existing models including Boussinesq closed form solution, standard ABAQUS material models, and published data from available multi-layered linear elastic pavement analysis software packages. Note that the implemented cross isotropic non-linear material model reduces to linear elasticity by using appropriate input parameters (table 5.2). The geometric parameters and loads summarized in table 5.2 refer to the dimensions and distributed loads shown in figure 5.1-a. Parameters for non-linear analyses are extracted by fitting constant confinement cyclic triaxial test data using the model and ABAQUS.

Isotropic linear elasticity: we model a 103kPa uniformly distributed load over a circular area of r=0.127m diameter on an isotropic linear elastic material with E=200MPa and a v=0.3. Boussinesq and numerical predictions superimpose as shown in figure 5.3-a.

Multi-layered isotropic linear elasticity: A conventional flexible pavement structure (figure 5.1-a) is modeled using isotropic linear elastic properties to match the simulations by Tutumluer (1995). Young's modulus and Poisson's ratio values for the different layers are presented in table 5.2. Predicted vertical stresses along the centerline caused by a 103kPa uniformly distributed load favorably compare to predictions made with KENLAYER and GT-Pave (data from Tutumluer 1995) in figure 5.3-b (note: apparent discrepancies between KENLAYER and GT-Pave are in part due to data digitization from published plots).

Multi-layered cross isotropic linear elastic: Predictions using the new code for cross-isotropic linear behavior are compared to published results obtained with GT-Pave in figure 5.3-c. The asphalt concrete and the subgrade are modeled as isotropic linear elastic layers using the same properties as in figure 5.3-b. The unbound aggregate layer is modeled as a cross-isotropic liner elastic layer (parameters in table 5.2). Values were selected to replicate Tutumluer's analysis and are not necessarily representative of a real unbound aggregate layer. Once again, there is close agreement between reported predictions and our model predictions.

Summary: the three verification studies show that the predictions made using the proposed user-defined material model subroutine compare favorably with the closed form solution and established multi-layered linear elastic isotropic and cross-isotropic simulators. These results verify the implementation of the new code.

5.3.4. Model Calibration

Constant confinement cyclic triaxial test results reported in Tutumluer (1995) for a crushed Georgia granite aggregate are used to assess the ability of the model to

reproduce the physical response of unbound aggregate layers. Tests were conducted at five different cell pressures and three deviatoric stress increments for each cell pressure. The procedure followed for the determination of the constitutive model k_i-parameters was described in chapter 4 and values are summarized in table 5.2. There is very good agreement between numerical model predictions and the experimental data, as shown in figure 5.4.

5.3.5. Domain Size and Boundary Conditions

A large number of numerical and experimental studies show that zero displacement boundaries must be at a distance R and depth t much greater than the radius of the contact area r, typically $R > 20r$ and $t > 140r$ to minimize boundary effects (see for example Kim 2007 and Kim et al. 2009). Note however, that the distance between the wheel path and the pavement edge can be as short as $R \approx 4r$ in the field. Furthermore, nearby rock can impose a rigid vertical boundary considerably closer than the prescribed $t > 140r$.

We conducted a numerical investigation of boundary effects on the predicted mechanical response of an inverted pavement structure. Following the recommendations of the guide for mechanistic-empirical design of new and rehabilitated pavement structures (ERES 2004), we use a 550kPa tire contact pressure spread over a circular area of radius 0.15m. The dimensions and material properties of individual layers are summarized in table 5.3. The pavement section is modeled using a 3D axisymmetric mesh that replicates the geometry of the inverted base pavement structure shown in figure 5.1-b. We assumed no-slip at the interfaces between layers. Results presented in figure 5.5 show the sensitivity of critical design parameters including effects on maximum

tensile strains in the asphalt concrete and cement treated sub-base, and maximum vertical compressive stresses in the unbound aggregate base and subgrade to variations in the horizontal domain *R*/*r*. Note that the cemented aggregate layers are not constrained in the transverse direction at the edges of pavement structure. The fill at the edges of a road may at best provide lateral constraint leading to compression but never to the development of tensile stresses. The influence of the lateral boundary was assessed by imposing a zero lateral displacement boundary along the edge of the model for all layers, figure 5.5-a,c, and only along the unbound aggregate base and subgrade layers, figure 5.5-b,d. There are only minor differences in the magnitude of the parameters studied. The domain size study shows clear and consistent trends for both boundary types. Boundary effects are minimal when $R/r > 20$; however, there is a 30% difference in predicted maximum tensile strains in the cement-treated base and a 15% difference in the predicted maximum compressive stress in the subgrade between R/r =10 to 50.

5.4. Simulation Studies and Results

Three simulation studies are conducted to determine the mechanical performance of an inverted base pavement structure, to study the impact of simplifying assumptions, and to identify an equivalent conventional flexible pavement structure for a pre-selected inverted base pavement.

5.4.1. Mechanical Performance of an Inverted Base Pavement Structure

This simulation study is conducted to determine the mechanical response, stresses and strains, of the inverted base pavement structure depicted in figure 5.1-b (layer thicknesses in figure 5.6). Following the findings on domain size reported above, we

model the load on the pavement as a 550kPa tire contact pressure spread over a circular area of radius r = 0.15m with a domain size R=10r = 1.50m. Material properties and layer thicknesses are summarized in table 5.3. The pavement structure is modeled using a 3D axisymmetric edge biased mesh, with zero-lateral-displacement boundaries at the edge of the pavement, zero-vertical-displacement at the foundation of the structure, and no-slip between the layers (figure 5.2).

The resulting vertical, radial and shear stress distributions along the centerline and under the wheel-edge are presented in figure 5.6. Vertical stresses along the centerline and the wheel-edge are compressive throughout the full depth of influence of the load, and become negligible within the cement-treated base. Radial stresses along the centerline and wheel-line for the asphalt concrete and cement-treated base layers range from compression at the top to tension at the bottom. Both vertical and radial stresses in the unbound aggregate base remain in compression for the full depth of the layer (in agreement with Mohr-Coulomb behavior). Shear stresses are zero along the centerline and reach maximum values along the wheel-edge. The maximum shear stress along the wheel-edge occurs within the asphalt concrete layer.

Radial slices of the vertical stress field are shown at multiple depths in figure 5.7-a. The vertical stress caused by the wheel load diminishes with depth to the point that the peak vertical stress on the subgrade is less than 4.5% of the vertical stress applied on the surface. Slices of the horizontal and shear stress fields at different depths are presented in figure 5.7-b,c. Radial tensile stresses in the asphalt layer are greatest along the bottom of the layer, reaching a maximum at the load centerline. Tensile stresses at the bottom of the cement-treated base also reach a maximum at the centerline. The shear stresses along the

asphalt concrete surface show a peak at the wheel-edge where there is a large discontinuity in vertical stresses. In the unbound aggregate layer, shear stresses increase slightly with depth along the wheel-edge. The cement-treated base considerably reduces the wheel induced shear stresses on the subgrade.

5.4.2. Linear Elastic Unbound Aggregate Layer Modeling Implications

The layer stiffness decreases with depth in conventional pavement structures. The use of linear elastic models for such a structure results in the prediction of tensile stresses at the bottom of the asphalt concrete layer, the unbound aggregate base and the sub-base. However, unbound aggregates are incapable of sustaining tensile stresses. The shortcomings of layered linear elasticity have stimulated the development of complex unbound aggregate material models and their implementation in the analysis of conventional flexible pavement structures with finite elements.

The linear elastic analysis of the modeled inverted base pavement structure does not predict tensile stresses in the unbound aggregate base along the centerline. The stiffness profile characteristic of inverted pavement structures results in the development of compressive stresses along the full thickness of the unbound aggregate base.

In order to determine the implications of using simple linear elastic models to characterize the unbound aggregate base in the analysis of an inverted base pavement structure we compare the results of the non-linear unbound aggregate inverted base pavement model (NLEP) studied in section 5.4.1. with a linear elastic model for the unbound aggregate base, using two values of the elastic modulus: a minimum value of 230MPa (LE1 model) corresponding to the in-situ measured unloaded unbound aggregate base stiffness, and a maximum value of 500MPa (LE2 model) corresponding to the

model predictions for the state of stresses at mid-depth in the unbound aggregate base under the 550kPa wheel load. The results of the three analyses are shown in figure 5.8; differences between linear and non-linear analyses follow:

1. The maximum tensile strain at the bottom of the asphalt concrete layer is under-predicted by 44% when using the maximum elastic modulus and by 11% when using the minimum elastic modulus.
2. The maximum tensile strain at the bottom of the cement-treated base is under-predicted by 11% when using the maximum elastic modulus and by 6.4% when using the minimum elastic modulus.
3. The maximum compressive stress on the unbound aggregate base is over-predicted by 34% when using the maximum elastic modulus and by 7.3% when using the minimum elastic modulus.
4. The maximum compressive stress on the subgrade is over-predicted by 130% when using the maximum elastic modulus and under-predicted by 5% when using the minimum elastic modulus.

Differences in tensile strains at the bottom of the asphalt concrete layer are of particular concern. Overall, these results suggest the low range stiffness values should be selected if linear elastic models are considered for pre-design.

5.4.3. Equivalent Conventional Flexible Pavement Study

The structural number *SN* of a flexible pavement structure of *i*-layers is given by (detail in AASHTO 1972 and ASHTO 1993):

$$SN = \sum_i a_i t_i$$

where a_i and t_i are the structural layer coefficient and thickness of layer *i*. Structural layer coefficients are obtained from either tabulated values or empirical correlations, and remain constant for a given material. If the structural layer coefficients are known, the layer thicknesses may be varied in order to obtain flexible pavement structures of equivalent structural number. The structural number reflects the relative stiffness between layers and values for conventional flexible pavement structures cannot be applied to inverted base pavements. We use successive forward simulations to identify a conventional flexible pavement of similar mechanical performance to the inverted section studied in section 5.4.1. The simulation assumes that the material properties of individual layers are the same in the conventional and inverted base sections (table 5.3).

The mechanical response is compared in terms of the critical design parameters for fatigue failure analysis (i.e., maximum tensile strain at the bottom of the asphalt concrete) and rutting failure analysis (i.e., maximum vertical stress on the subgrade). The mechanical response of the studied inverted base pavement and three conventional flexible pavement sections are compared in figure 5.9. To facilitate the comparison, we keep the thickness of the unbound aggregate base constant in all the conventional pavement structures. Simulation results show that a conventional pavement section with asphalt concrete thickness t_{AC}= 0.15m, and an unbound aggregate base thickness t_{UAB}=0.3m sustains similar maximum tensile strain in the asphalt concrete layer as the inverted pavement. Furthermore, the inverted pavement is more efficient in redistributing the vertical compressive stresses transferred to the subgrade.

5.5. Discussion

Boundary conditions in the field. The proximity of the wheel to the road often creates a range of physically meaningful domain sizes between $R/r = 5$ to 10. Results in figure 5.5 show that simulations with a domain size $R/r \geq 20$ can lead to a ~140% underestimation of the maximum compressive stress in the subgrade, a ~60% overestimation of the maximum tensile strain in the cement-treated base, and a ~6% overestimation of the maximum tensile strain in the asphalt concrete layer. Consequently, predictions made using $R/r \geq 20$ would underestimate subgrade rutting, the fatigue resistance of the cement-treated base and the fatigue life of the asphalt concrete layer.

Mechanical performance. The vertical stress profile presented in figures 5.7-a shows that the compressive vertical stresses along the centerline from the applied wheel load on top of the asphalt concrete, to the top of the cement treated sub-base decreases by 190/550kPa. The maximum tensile radial stresses at the bottom of the asphalt concrete and of the cement-treated base show a 350/1300kPa reduction in figure 5.7-b. The maximum tensile stress in the asphalt concrete layer (figure 5.6) is a source of concern as it approaches the reported tensile strength for the material: values of tensile strength consistent with the selected asphalt concrete Young's modulus range between 2400 and 3500kPa (Richardson and Lusher 2008). Thus, according to the predictions, the layer mobilizes tensile stresses between 0.4 and 0.5 of the material tensile strength for the simulated load. The predicted maximum tensile strain 2.3×10^{-4} is in the range measured for inverted base pavement test sections built with similar materials and geometry (2.6×10^{-4}~3.4×10^{-4} - Tutumluer and Barksdale 1995), and resembles the strain level in a conventional flexible pavement with an asphalt concrete layer twice as thick.

Linear elastic unbound aggregate material models. The stiffness profile characteristic of an inverted pavement structure prevents the generation of tensile stresses in the unbound aggregate base regardless of the material model assigned to the unbound aggregate base (linear or non-linear elastic). Yet, a preliminary analysis using linear elastic models is unwarranted. A linear elastic analysis based on the maximum expected modulus yields conservative subgrade and unbound aggregate base rutting predictions, but un-conservative asphalt concrete and cement-treated base fatigue predictions. Similarly, a linear elastic analysis based on the minimum expected stiffness produces un-conservative asphalt concrete and cement-treated base fatigue and unbound aggregate base and subgrade rutting predictions

Equivalent section. Limited comparative results of equivalent sections show a superior performance of the inverted base pavement in terms of subgrade rutting prevention (lower peak vertical stress on the subgrade) for the same maximum tensile strain in the asphalt concrete layer (i.e., equal fatigue life). However, thin asphalt concrete layers are prone to shear failure and top-down cracking due to the stresses along the wheel-edge.

The unbound aggregate material properties will not be the same in inverted and conventional flexible pavement structures. The aggregate base in inverted base pavements can reach high density because of the support provided by the stiff cement-treated base during compaction. Therefore, the as-built unbound aggregate base in an inverted pavement structure may exhibit higher stiffness and lower long-term stiffness-degradation than the aggregate base in a conventional flexible pavement.

It follows from this discussion that: the material parameters used to model the unbound aggregate base in an inverted base pavement and a conventional flexible pavement may vary for the same aggregate, the empirical fatigue and rutting distress prediction models developed for conventional flexible pavements are prone to yield conservative estimates of pavement life for inverted base pavement structures (differences in stiffness degradation), and that the design of inverted base pavement structures requires analysis of additional failure mechanisms and critical mechanical response parameters.

5.6. Conclusions

The mechanical response of an inverted base pavement structure was studied using a physically appropriate material model for non-linear elasto-plastic behavior implemented in ABAQUS through an user-defined material subroutine.

The maximum compressive stress on the subgrade and maximum tensile strain in the cement-treated base are domain size dependent within the range of physically meaningful domain sizes for wheel-to-road edge conditions. Mechanical performance predictions based on large domain sizes (R/r >20) prevent boundary effects but overestimate the fatigue resistance of the cement-treated base and the asphalt concrete layer.

The stiffness profile characteristic of an inverted pavement structure leads to the absence of tensile stresses in the unbound aggregate base regardless of the material model assigned to the unbound aggregate (linear or non-linear elastic). However, critical design

parameters derived from linear elastic analyses differ considerably from predictions based on non-linear elastic analyses.

Simulation results show that the maximum vertical compressive stress in the subgrade of an inverted pavement is lower than the predicted for a conventional flexible pavement structure with the same maximum strain in the asphalt concrete layer.

The as-built material parameters used to model the unbound aggregate base in an inverted base pavement and a conventional flexible pavement may vary for the same aggregate.

Table 5.1 Material models used in previous finite element analysis of flexible pavement structures

AC	UAB	Subgrade	CTB	Details	References
t_{AC}= 0.05 to 0.2m Linear elastic E= 4, 7, and 12 GPa; v= 0.3	t_{UAB}= 0.2 to 0.7m Non-linear elastic cross-isotropic s_1= ⅓; s_2=1; α= (8634,19454kPa); β= (0.69,0.5); γ= 0; v= 0.3	Linear elastic E= 20 to 70MPa v= 0.3	N/A	Conventional flexible pavements [SENOL] Q= 500kPa, r= 0.16m	(Brown and Pappin 1985)
t_{AC}= 0.09m Linear elastic E= 1720MPa; v= 0.35	t_{UAB}= 0.2m Non-linear elastic cross-isotropic s_1= ⅓; s_2=1; α= 5367psi; β= 0.61; γ= -0.07; E_{Rp}=0.8E_{Rz}; v_{zp}= 0.43; v_{pp}= 0.15	t_{SG}= 1.27m, 1.12m Non-linear elastic Bilinear model	t_{CTB}= 0.15m Linear elastic E= 10340MPa v= 0.2	Axisymmetric Inverted and conventional flexible pavements [GT-PAVE] Q= 689kPa, r= 0.116m	(Tutumluer 1995; Tutumluer and Barksdale 1995)
t_{AC}= 0.05, to 0.15m Non-linear elastic s_1= ⅓P_a; s_2=P_a; α= 28000Pa; β= 0.1; γ= 0.001; v= 0.35	t_{UAB}= 0.15 to 0.45m Non-linear elastic cross-isotropic s_1= ⅓P_a; s_2=P_a; α= 3500P_a; β= (0,0.455); γ= (0,0.295); v_{zp}= 0.2; G*=0.38E_{Rz};E_{Rp}=(0.5,1)E_{Rz};v_{pp}= 0.3	t_{SG}= 2.12 to 2.52m Non-linear elastic s_1= ⅓P_a; s_2=P_a; α= (207,1035,2070)P_a; β= 0.001;γ= 0.3;v =0.35	NA	Axisymmetric Conventional flexible pavements Q= 690kPa, r= 0.136m, R=10r	(Adu-Osei et al. 2001b)
t_{AC}= 0.1m Linear elastic E= 4995.3MPa; v= 0.35 Non-linear elastic s_1= ⅓P_a; s_2=P_a; α= 50000Pa; β= 0.1;γ= 0	t_{UAB}= 0.2m Linear elastic E= 69.9MPa; v= 0.35 Non-linear elastic s_1= ⅓P_a; s_2=P_a; α= 700P_a; β= 0.6; γ= -0.3	t_{SG}= 1.7m Linear elastic E= 40MPa; v= 0.4 Non-linear elastic s_1= ⅓P_a; s_2=P_a; α= 400P_a; β= 0; γ= -0.3	N/A	Axisymmetric Conventional flexible pavement sections Q= 689kPa, r= 0.136m, R=10r	(Park and Lytton 2004)
t_{AC}= 0.1m Linear elastic E= 2760MPa; v = 0.35	t_{UAB}= 0.3m Non-linear elastic cross-isotropic @170kPa E_{Rz}= 25968, 23088psi; E_{Rp}= 5476, 8657psi; G*= 3815, 4351psi;	Linear elastic E= 20.7MPa; v = 0.45	NA	Conventional flexible pavements [TTI-PAVE] Q= 1600kPa, r= 0.089m	(Kim et al. 2005)
t_{AC}= 0.08 to 0.127m Linear elastic E= 2759, 8286MPa; v= 0.35	t_{UAB}= 0.2 to 0.3m Non-linear elastic isotropic s_1= ⅓P_o; s_2=P_o; v= (0.38,0.4) α= (3.5,4.1,6.3,10.3)MPa;β= (0.4, 0.635, 0.64); γ= (0, 0.01, 0.065);	t_{SG}= 20.8 to 21m Non-linear elastic Bilinear model v= (0.4,0.45)	NA	3D-symmetric and axisymmetric Conventional flexible pavements [ABAQUS] Q= 551kPa, r= 0.152m, R=20r	(Kim et al. 2009)

$$E_R = \alpha\left(\frac{p}{s_1}\right)^{\beta}\left(\frac{q}{s_2}\right)^{\gamma}$$

Note: the generic model parameters provided are valid only for $\sigma_2=\sigma_3$

Table 5.2 Numerical simulator verification and validation parameters.

Figure	Load/Geometry	Properties	Parameters
Figure 5.3 (a)	Q = 103kPa R = 1.3m r = 0.127m t = 2.54m	E = 200MPa υ = 0.3	$k_1 = k_5$ = 200MPa ; k_9 = 76.9MPa $k_2 = k_3 = k_4 = k_6 = k_7 = k_8 = k_{10} = k_{11} = k_{12} = 0$ $v_{pp} = v_{zp}$= 0.3 ; p_0= 1kPa
Figure 5.3 (b)	Q = 103kPa R = 1.3m r = 0.127m t_{AC} = 0.1m t_{UAB} = 0.28m t_{SG} = 2.54m	AC: E = 2000MPa υ = 0.35 UAB: E = 310MPa υ = 0.45 SG: E = 50MPa υ = 0.4	AC: $k_1 = k_5$ = 2000MPa ; k_9 = 741MPa $k_2 = k_3 = k_4 = k_6 = k_7 = k_8 = k_{10} = k_{11} = k_{12} = 0$ $v_{pp} = v_{zp}$= 0.35 ; p_0= 1kPa UAB: $k_1 = k_5$ = 310MPa ; k_9 = 107MPa $k_2 = k_3 = k_4 = k_6 = k_7 = k_8 = k_{10} = k_{11} = k_{12} = 0$ $v_{pp} = v_{zp}$= 0.45 ; p_0= 1kPa SG: $k_1 = k_5$ = 50MPa ; k_9 = 17.9MPa $k_2 = k_3 = k_4 = k_6 = k_7 = k_8 = k_{10} = k_{11} = k_{12} = 0$ $v_{pp} = v_{zp}$= 0.4 ; p_0= 1kPa
Figure 5.3 (c)	Q = 103kPa R = 1.3m r = 0.127m t_{AC} = 0.1m t_{UAB} = 0.28m t_{SG} = 2.54m	AC: E = 2000MPa υ = 0.35 UAB: E_z= 310MPa E_p= 46.5MPa G^* = 108MPa υ_{pp} = 0.15 υ_{zp}= 0.45 SG: E = 50MPa υ = 0.4	AC: $k_1 = k_5$ = 2000MPa ; k_9 = 741MPa $k_2 = k_3 = k_4 = k_6 = k_7 = k_8 = k_{10} = k_{11} = k_{12} = 0$ $v_{pp} = v_{zp}$= 0.35 ; p_0= 1kPa UAB: k_1 = 310MPa ; k_5 = 46.5MPa ; k_9 = 108MPa $k_2 = k_3 = k_4 = k_6 = k_7 = k_8 = k_{10} = k_{11} = k_{12} = 0$ v_{pp}= 0.15 ; v_{zp}= 0.45 ; p_0= 1kPa SG: $k_1 = k_5$ = 50MPa ; k_9 = 17.9MPa $k_2 = k_3 = k_4 = k_6 = k_7 = k_8 = k_{10} = k_{11} = k_{12} = 0$ $v_{pp} = v_{zp}$= 0.4 ; p_0= 1kPa
Figure 5.4	$R = r$ = 0.0762m t = 0.304m	$E_R = E_R(p,q)$	k_1 = 32.8MPa ; k_5 = 32.8MPa ; k_9 = 12.3MPa $k_2 = k_6 = k_{10}$ = 0.5 $k_3 = k_7 = k_{11}$ = 0.9 $k_4 = k_8 = k_{12}$ =16 $v_{pp} = v_{zp}$= 0.33 p_0= 1kPa ; φ = 40° ; C = 6.89kPa

Table 5.3 Material properties and layer dimensions

Layer	Material Model
Asphalt Concrete (t_{AC} = 0.09m)	*Isotropic linear elastic* E = 1.7 GPa v = 0.35
Unbound Aggregate Base (t_{UAB} = 0.15m)	*Isotropic nonlinear elasto-plastic* $E_{Rz} = 200MPa \cdot \left(\frac{p}{1kPa}\right)^{0.2}\left[1-0.9\cdot\left(\frac{q}{q_f}\right)^4\right]$ $E_{Rp} = 200MPa \cdot \left(\frac{p}{1kPa}\right)^{0.2}\left[1-0.9\cdot\left(\frac{q}{q_f}\right)^4\right]$ $G^* = 76.9MPa \cdot \left(\frac{p}{1kPa}\right)^{0.2}\left[1-0.9\cdot\left(\frac{q}{q_f}\right)^4\right]$ v_{pp}= v_{zp}= 0.3 φ = 40° ; C = 1kPa
Cement Treated Base (t_{CTB} = 0.25m)	*Isotropic linear elastic* E = 13.7 GPa v = 0.2
Subgrade (t_{SG} = 2.54m)	*Isotropic linear elastic* E = 100 MPa v = 0.2

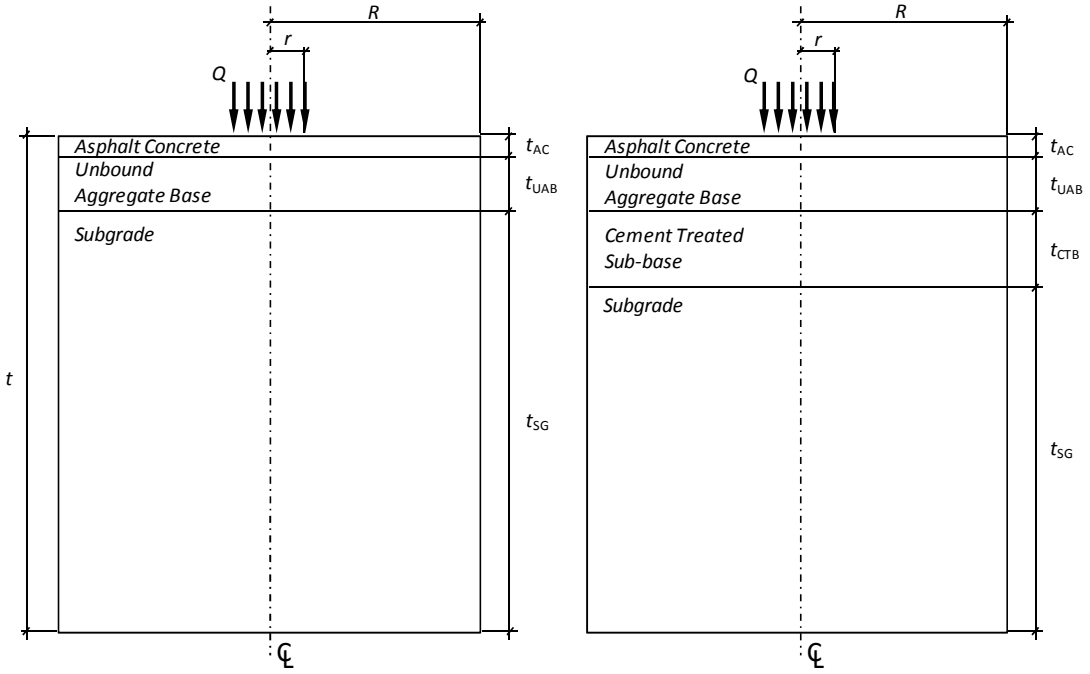

Figure 5.1 Conventional flexible pavement (a) and (b) inverted base pavement structures.

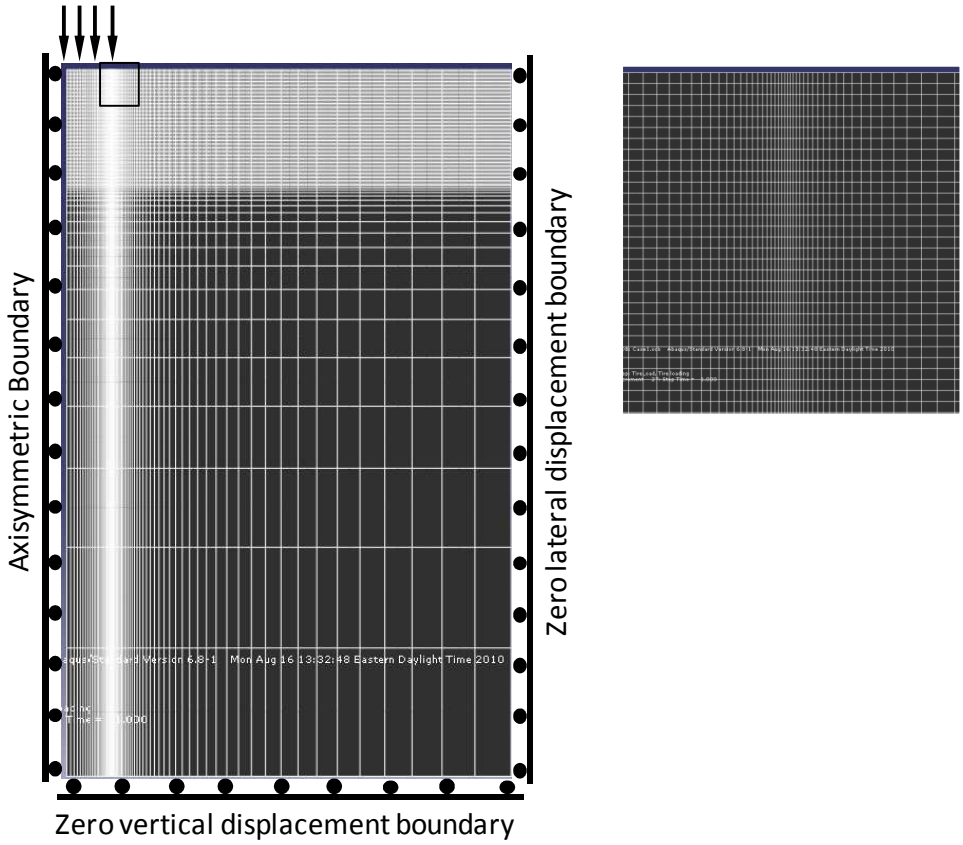

Figure 5.2 Meshed pavement section using edge biased seeding techniques. This method results in a non-uniform distribution of elements along the edge with density bias in the vicinity of steep gradient areas. The insert zooms in to the edge of the wheel load.

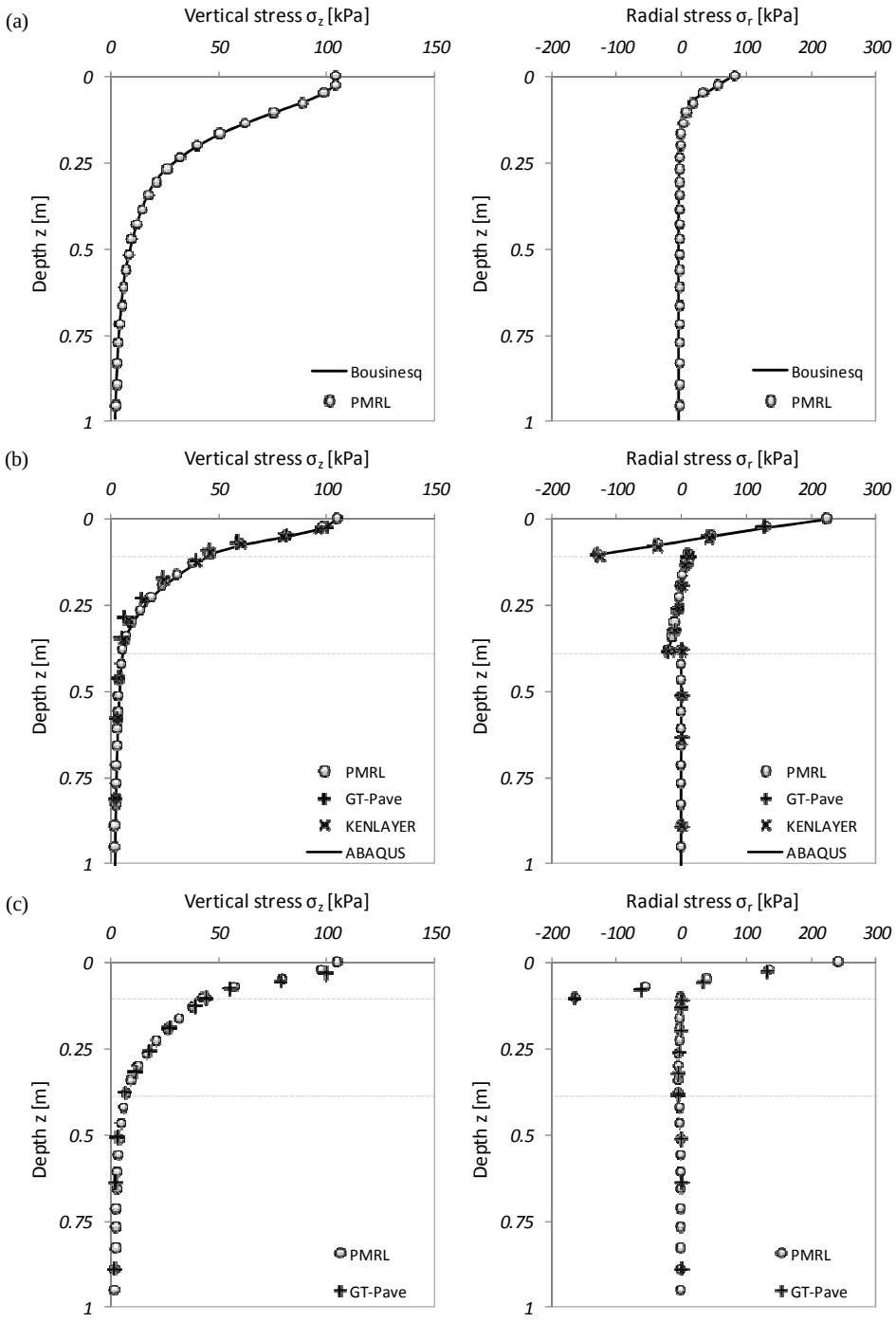

Figure 5.3 Model validation studies: (a) isotropic linear elastic half space subjected to a circular uniform load, (b) layered isotropic linear elastic solutions from available pavement analysis software, (c) layered cross-isotropic linear elastic base solutions from GT-Pave. Results presented for KENLAYER and GT-Pave were digitized from Tutumluer (1995).

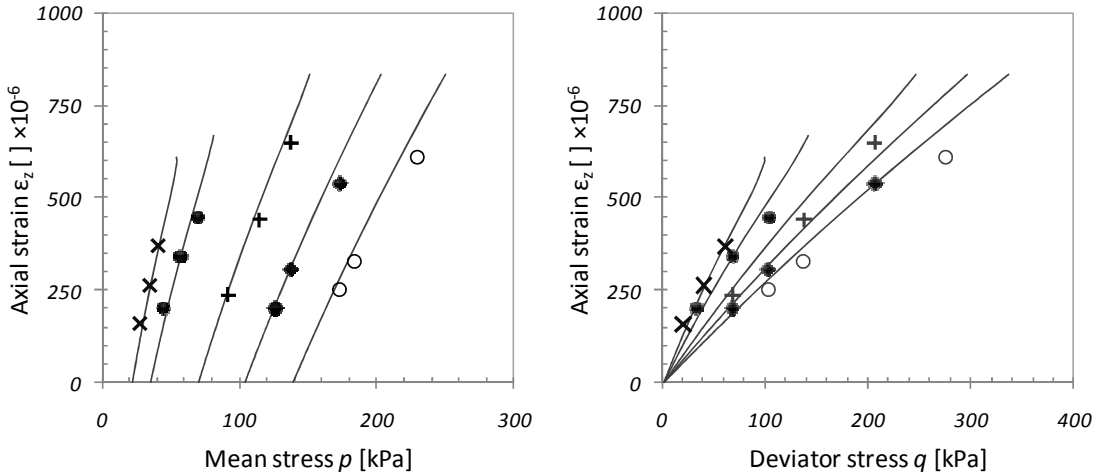

Figure 5.4 Non-linear elastic model validation using repeated load triaxial test results for crushed granite from Georgia (data in Tutumluer 1995).

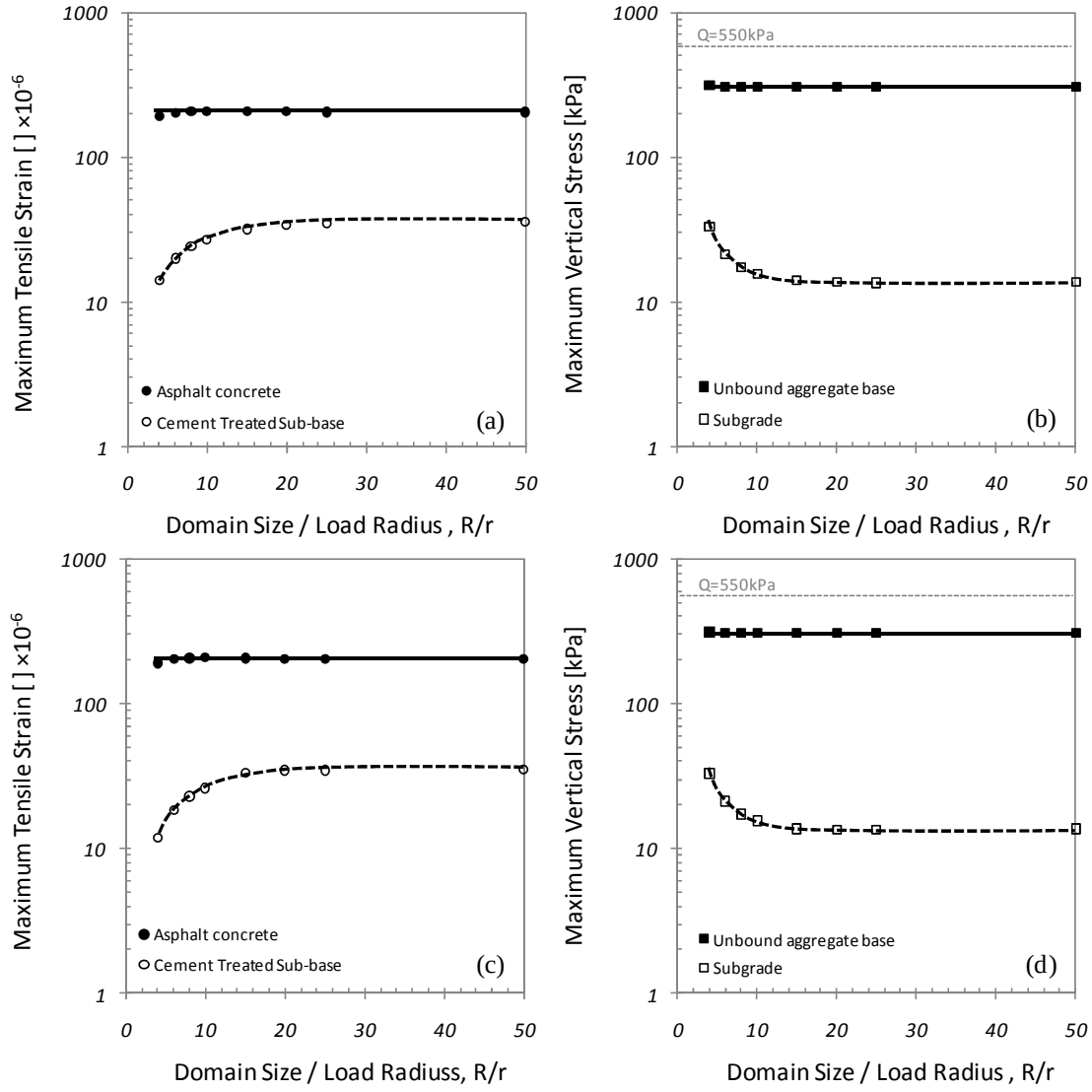

Figure 5.5 Effects of model domain size and choice of boundary conditions on critical pavement design parameters for an inverted base pavement structure: maximum tensile strains in the asphalt concrete ε_{AC} and cement-treated base ε_{CTB} layers (a) and (c), and maximum vertical stress on the unbound aggregate base σ_{UAB} and subgrade σ_{SG} layers (b) and (d). Zero lateral displacement boundaries are used along the edge of the model for all layers in (a) and (c), and along the unbound aggregate base and subgrade only in (b) and (d).

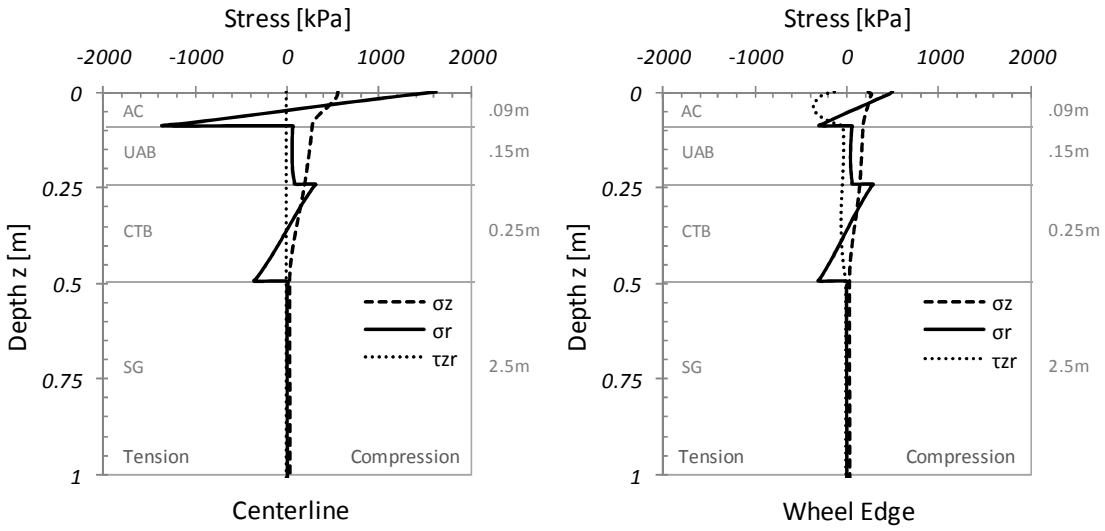

Figure 5.6 Vertical σ_z, radial σ_r, and shear τ_{zr} stress profiles as a function of depth in the modeled inverted base pavement section along the load centerline and the wheel edge for a 550kPa uniformly distributed load over a circular area of radius 0.15m.

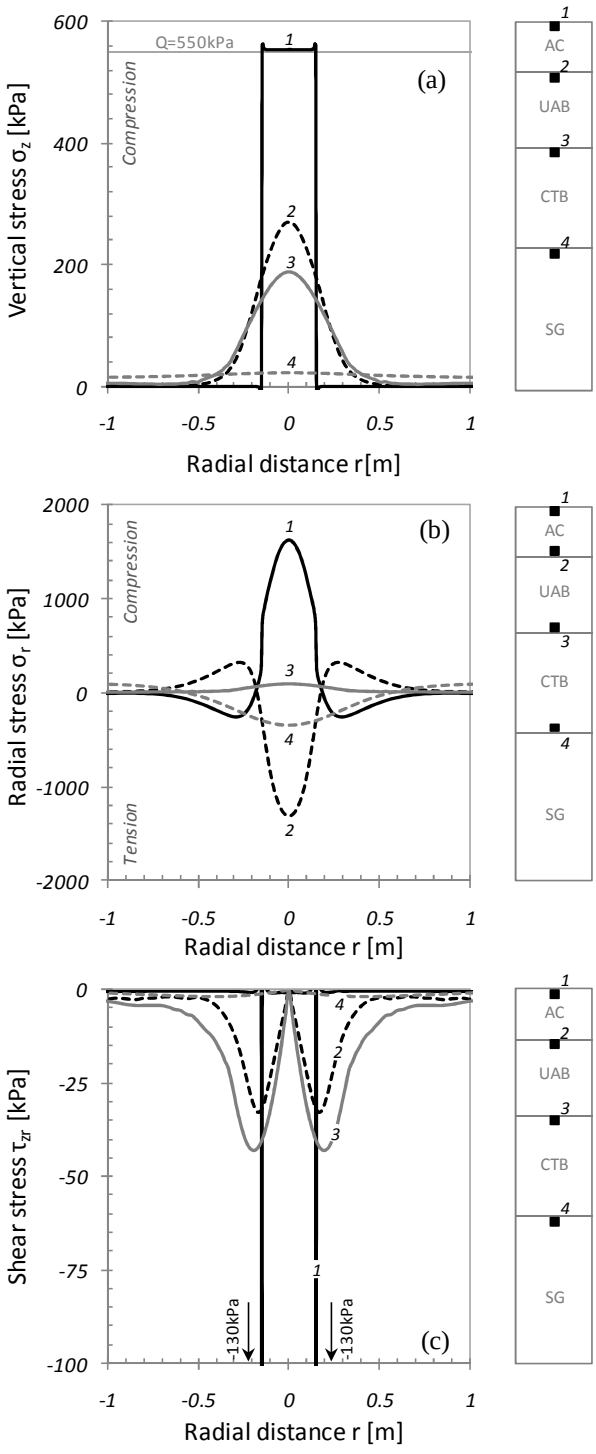

Figure 5.7 Radial profiles of (a) vertical, (b) radial, and (c) shear stresses at multiple locations within the inverted base pavement structure. Q = 550kPa, r = 0.15m, and R=10r.

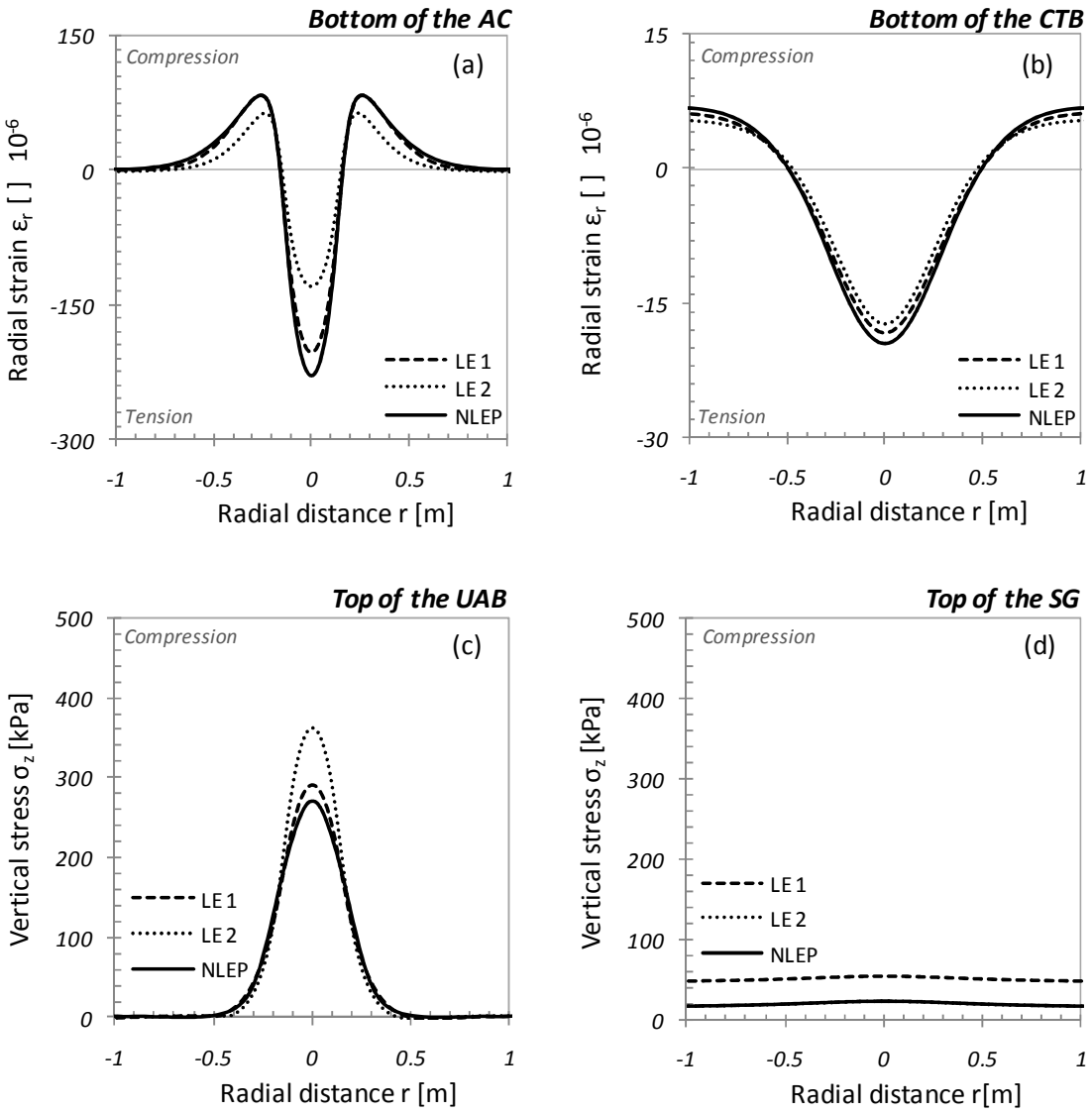

Figure 5.8 Comparison between inverted base pavement critical design parameter predictions from linear elastic and non-linear elasto-plastic unbound aggregate base models: (a) strains at the bottom of the asphalt concrete layer, (b) strains at the bottom of the cement treated base layer, (c) vertical stresses on top of the unbound aggregate base layer, and (d) vertical stresses on top of subgrade layer. Q = 550kPa, r = 0.15m, and R=10r.

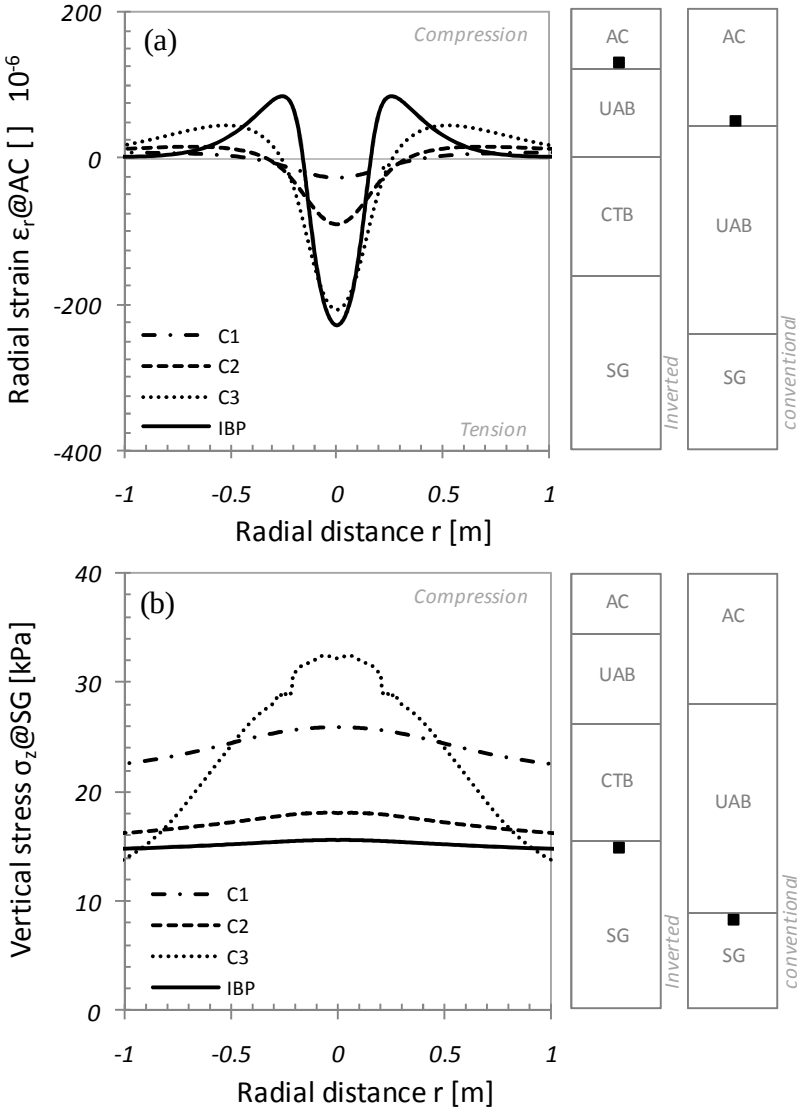

	t_{AC} [m]	t_{UAB} [m]	t_{CTB} [m]
C1	*0.46*	*0.30*	*0*
C2	*0.25*	*0.30*	*0*
C3	*0.15*	*0.30*	*0*
IBP	*0.09*	*0.15*	*0.25*

Figure 5.9 Mechanical response in terms of (a) tensile strains at the bottom of the asphalt concrete layer and (b) vertical stresses on the subgrade for the studied inverted base pavement and three conventional flexible pavement sections. Wheel load Q = 550kPa, contact area radius r = 0.15m, and domain size R=10r.

CHAPTER 6

RECOMMENDED PRELIMINARY GUIDELINES FOR DESIGN

6.1. Introduction

Inverted base pavements have been used as affordable and structurally competent pavement structures in South Africa since the 1950's (Horne et al. 1997; Rust et al. 1998; Beatty et al. 2002). The South African flexible pavement design emphasizes the importance of a good foundation, involve novel construction methods and careful material selection to achieve dense unbound aggregate layers that exhibit a remarkable ability to support the heaviest traffic loads under both dry and wet conditions (Horne et al. 1997). Cement-treated bases emerged to provide a suitable foundation for high quality densely compacted unbound aggregate bases throughout their service life (Jooste and Sampson 2005). While stabilized layers alone improve the structural capacity of the pavement they may cause reflective cracking, which accelerates pavement deterioration. Yet, a stone inter-layer can prevent the propagation of reflective cracks through strain dissipation within the unbound aggregate layer (Rasoulian et al. 2001).

This chapter starts with a comprehensive review of inverted base pavement research in the United States. Then, a parametric study based on the constitutive model selected in chapter 4 and the code developed in chapter 5 is performed to assess the mechanical performance of various inverted base pavement structures. Finally, we propose equivalent inverted base pavement structures for typical low, middle, and high volume flexible pavement designs based on simulation results.

6.2. Inverted Base Pavement Structures in the U.S.A.

6.2.1. U.S. Corps of Engineers (1970's)

The U.S. Corps of Engineers studied the behavior of the various layers in flexible pavement structures having lime-stabilized and cement-stabilized sub-bases (i.e., inverted base type structures). The objective of the study was to measure the mechanical response of full-scale pavement structures and to compare the results against predictions from layered elastic theory and other available constitutive models. Two inverted base pavement structures were investigated, both composed of a 0.09m asphalt concrete layer, a 0.15m crushed limestone base, a 0.38m stabilized clay sub-base, and a clay subgrade (CBR= 4). The structures were subjected to traffic under controlled conditions while monitoring displacements and stresses at key locations (Ahlvin et al. 1971; Barker et al. 1973; Grau 1973).

Linear elastic analyses failed to adequately predict the measured stresses and strains in different layers and the plastic subgrade deformation. The performance of the inverted pavement structures was found to be influenced by the stiffness and tensile strength of the cement-treated base. This study highlighted the importance of a comprehensive material characterization and numerical implementation through appropriate constitutive models. Furthermore, it urged the development of laboratory tests capable of simulating field conditions, and the introduction of non-linear models in numerical simulations (Barker et al. 1973).

6.2.2. Georgia Tech (1980's)

Twelve laboratory-scale instrumented pavement structures were cyclically loaded to failure under controlled environmental conditions. There were five conventional flexible pavements with crushed stone bases, five full depth asphalt sections, and two inverted base pavement structures. The two inverted pavements consisted of a 0.09m asphalt concrete layer, a 0.20m unbound aggregate layer (well graded granitic gneiss), and a 0.15m cement-treated base over a micaceous silty sand subgrade. The asphalt surface layer was a GDOT-B binder mixed with granitic gneiss, laid in 0.04m lifts. It was found that the cement-treated base facilitates compaction in inverted structures leading to denser unbound aggregate layers (Barksdale 1984).

The pavement sections were subjected to a 28.9kN cyclic load for the first 2×10^6 repetitions. The load was then increased to 33.4kN and cycled until the pavement structures failed. All sections were extensively instrumented with Bison-type strain sensors, small diaphragm pressure cells and linear LVDT's to monitor strains and stresses at key locations. It was found that the two inverted base pavement sections outperformed equivalent pavement structures in terms of lower resilient surface displacements, reduced transferred compressive-stress onto the subgrade and less tensile-radial-strain at the bottom of the asphalt concrete layer. The superior mechanical performance of the inverted pavement structures was also reflected in the number of load cycles to failure (3.6×10^6 and 4.4×10^6 cycles), which outlasted the best performing conventional section by 1×10^6 cycles (Barksdale 1984; Tutumluer and Barksdale 1995).

6.2.3. Route LA97 and Accelerated Pavement Testing - Louisiana (1990's)

The ability of inverted pavements to prevent reflective cracking was assessed in a full-scale low-volume rural highway section in Louisiana (1991-2001). The studied inverted base pavement structure consisted of a 0.09m asphalt concrete layer, a 0.10m crushed limestone base, and a 0.15m cement-treated base. The test section was subjected to periodic post-construction monitoring of pavement distress, ride roughness, surface rutting, and assessment of the structural capacity through non-destructive dynamic deflection. The performance of the inverted pavement section was compared to that of the rest of the road (conventional flexible pavement cement-treated base). The study concluded that the inverted base pavement outperformed the conventional design in terms of cracking density and severity after 10 years, and also offered a superior ride quality over the evaluation period (Rasoulian et al. 2001).

The superiority of the inverted base pavement was further confirmed with a complementary study in the first Louisiana accelerated pavement experiment (1995). The purpose of this study was to evaluate alternative soil-cement base courses with reduced reflective cracking. The inverted pavement structure carried 4.7 times more ESAL's than the conventional flexible pavement on a cement-stabilized-base, and outperformed the rest of the pavement structures studied in this project (Rasoulian et al. 2000).

6.2.4. Morgan County Quarry Access Road – Georgia (early 2000's)

Two inverted base pavement test sections were constructed in a quarry haul road in Morgan County, Georgia in 2001. The structures consist of a 0.08m asphalt concrete layer, a 0.15m crushed Georgia granite base, and a 0.20m cement-treated base. The Morgan County inverted pavement test sections were built to compare the effectiveness

of South African and Georgia compaction practices. Thus, emphasis was placed on the densification of the unbound aggregate base layer. The test sections have experienced uninterrupted high-volume heavy-truck traffic for 9 years. Surveys conducted in May 2008 after the section had serviced over 1.2 million ESALs in 7 years (75% of the designed service life), found no signs of distress or changes in ride quality (Lewis 2009).

6.2.5. LaGrange Georgia (2010's)

A full-scale field study was conducted in LaGrange, Georgia starting in 2009 (details in chapter 2). The inverted base pavement test section is a two-lane 1036m long stretch of the south LaGrange loop. It was designed to sustain an initial one-way annual average traffic of 7000 vehicles per day projected to grow to 11700 by the end of its service life. The structure consists of a 0.09m asphalt concrete layer, a 0.15m crushed Georgia granite base, and a 0.20m cement-treated base. The average specific surface and coefficient of uniformity of the subgrade indicate that its mechanical behavior is strongly influenced by electrical interactions and capillarity; therefore, it is susceptible to changes in water content and pore fluid chemistry. Off-site mixing, transport, spreading, and compaction of the cement-treated mix resulted in a homogeneously compacted cement-treated base. The 7-day cured cement-treated aggregate base withstood the compaction of the overlaying layers without cracking under the loading imposed by heavy equipment and construction operations. Digital image analysis confirmed particle-shape/compaction induced anisotropy in the as-built unbound aggregate base; however, the results of laboratory non-linear stiffness-stress response showed that stiffness anisotropy is primarily caused by the anisotropic state of stresses and that there is a unique stiffness-

stress relationship in the directions of principal stresses. The pavement was opened to traffic in April 2009. First performance data are expected in 2011.

6.2.6. Summary of Key Observations

- The cement-treated base in an inverted base pavement structure facilitates the compaction of the unbound aggregate base.
- The unbound aggregate base in an inverted base pavement structure prevents reflective cracking.
- Large fluctuations in traffic induced stress caused by the proximity of the unbound aggregate layer to the pavement surface requires the use of proper non-linear constitutive models for the analysis of inverted pavement structures.
- Both, the South African experience (40+ year) and the accumulating experience in the U.S.A. show that inverted base pavements may outperform conventional flexible pavement structures.

6.3. Inverted Base Pavements – Parametric Numerical Study

The design of flexible pavements is a two step process. First, stresses and strains induced by traffic load are computed for the different layers. Then, the pavement performance is verified based on mechanical analyses (e.g., failure) and the service life is estimated using empirical distress prediction models (e.g., fatigue). The most critical stresses and strains considered to assess performance are (1) the maximum tensile strain in the asphalt concrete layer ε_{AC}, (2) the maximum compressive stress on the unbound aggregate base σ_{UAB}, (3) the maximum tensile strain in the cement-treated base ε_{CTB}, and (4) the maximum compressive stress on the subgrade layer σ_{SG}. In this study, we explore

these four mechanical responses for different layer thickness, material properties, and choice of constitutive model.

The simulated inverted base pavement structure is depicted in figure 6.1. Following the recommendations of the guide for mechanistic-empirical design of new and rehabilitated pavement structures (ERES 2004) and findings reported in chapter 5, we model the load on the pavement structures as a 550kPa tire contact pressure spread over a circular area of radius r = 0.15m with a domain size R= 13r (refer to chapter 5). The pavement structure is modeled using a 3D-axisymmetric, edge-biased mesh with zero-lateral-displacement boundaries at the edge of the pavement, and zero-vertical-displacement at the foundation of the structure.

The constitutive models and material parameters used in all studies are summarized in table 6.1 (refer to chapter 4). The asphalt concrete layer, the cement-treated base and the subgrade were modeled as isotropic linear elastic materials. The unbound aggregate base was modeled as an isotropic non-linear elasto-plastic material. The parameters used to characterize the unbound aggregate base were selected based on the results of in-situ measurements, laboratory K_o test results and data reported in the literature for cyclic triaxial tests. The material properties for each layer are the same in all simulations.

6.3.1. Scope

The parametric study includes 6 series of numerical simulations. These are described next.

1. *Asphalt and unbound aggregate layer thickness*. The mechanical response of the inverted pavement structure is analyzed for changes in the thicknesses of the asphalt

concrete and unbound aggregate layers. A total of 16 cases were modeled, 4 asphalt concrete layer thicknesses (t_{AC} = 0.051m, 0.076m, 0.127m, and 0.203m) and 4 unbound aggregate base thicknesses (t_{UAB} = 0.101m, 0.152m, 0.203m, and 0.254m), all sitting on a t_{CTB} = 0.152m cement-treated base. The range of layer thicknesses was chosen based on constructability, cost effectiveness, and typical GDOT specifications (Lewis 2009).

2. *Unbound aggregate base: Quasi-linear response using the minimum stiffness*. The unbound aggregate base is modeled as a liner-elastic material. The selected elastic modulus corresponds to an unloaded in-situ stiffness measurement (reported in chapter 3).
3. *Unbound aggregate base: Quasi-linear response using the maximum stiffness*. Similar to the previous study but in this case, the selected elastic modulus is the maximum stiffness induced in the unbound aggregate base by the 550kPa tire contact pressure.
4. *Soft "hot" asphalt*. The stiffness of asphalt concrete changes as a function of temperature. In this study we explore changes in the response of inverted base pavement structures caused by a lower stiffness hot asphalt concrete.
5. *Stiff "cold" asphalt*. Similar to the previous case, we now explore the effect of higher stiffness cold asphalt on the mechanical response of inverted pavement structures.
6. *Thick cement-treated base*: This final set of simulations is designed to investigate the effect of the thickness of the cement-treated base t_{CTB} on the performance of the inverted base pavement structure.

6.4. Results

The 16 combinations of asphalt concrete and unbound aggregate base thicknesses t_{AC} and t_{UAB} are explored first. Then, we reduce the number of combinations and simulations required to explore the response of inverted base pavements to other variables by pre-selecting 4 layer thickness combinations: (A) t_{AC} = 0.203m and t_{UAB} = 0.101m, (B) t_{AC} = 0.051m and t_{UAB} = 0.101m, (C) t_{AC} = 0.051m and t_{UAB} = 0.254m, and (D) t_{AC} = 0.203m and t_{UAB} = 0.254m. The results are presented next for the eight parametric studies.

6.4.1. Asphalt and Unbound Aggregate Layer Thickness (Base Cases)

Results are summarized in figure 6.2. An increase in the thickness of the asphalt concrete layer leads to lower maximum tensile strain in the asphalt concrete layer ε_{AC}, lower maximum tensile strain in the cement-treated sub-base ε_{CTB}, lower maximum compressive stress on the unbound aggregate base σ_{UAB}, and lower maximum compressive stress on the subgrade σ_{SG}. Increasing the thickness of the unbound aggregate layer leads to higher maximum tensile strains in the asphalt concrete layer, lower maximum tensile strains in the cement-treated base, lower maximum compressive stress on the unbound aggregate base, and lower maximum compressive stress on the subgrade.

It follows that the combination of a thicker asphalt concrete layer and a thinner unbound aggregate base helps mitigate fatigue cracking in the bonded layers and rutting failure in the unbound aggregate layers.

6.4.2. Unbound Aggregate Base Quasi-Linear Response: Minimum Stiffness

All simulations using the non-linear model for the unbound aggregate base showed no tensile strains in the UAB. In this context and in an attempt to develop simplified design methods, we explore the possibility of representing the unbound aggregate base using a liner-elastic model with a Young's modulus equal to the minimum UAB stiffness measured under no traffic load. Results presented in figure 6.3 show that a thicker asphalt concrete layer reduces the maximum tensile strain in the cement-treated base and the maximum compressive stress in the unbound aggregate base.

6.4.3. Unbound Aggregate Base Quasi-Linear Response: Maximum Stiffness

The predictions made using a liner-elastic model with a Young's modulus equal to the maximum cyclic triaxial measured resilient modulus are presented in figure 6.4. Results confirm previous trends for the cases with highest unbound aggregate base stiffness.

6.4.4. Soft "Hot" Asphalt

Reducing the asphalt concrete layer stiffness results in an increase in the maximum tensile strain in the asphalt concrete layer and the cement-treated base (figure 6.5). There is also an increase in the maximum compressive stress in the unbound aggregate base, yet the stress in the subgrade remains similar to the base cases.

6.4.5. Stiff "Cold" Asphalt

The predicted performance of inverted pavement structures with a stiffer asphalt concrete are shown in figure 6.6 and show opposite trends to those noted for the soft "hot" asphalt case.

6.4.6. Thick Cement-Treated Base

Simulation results show that a thicker cement-treated base causes a pronounced reduction in the magnitude of the maximum tensile strain in the cement-treated layer (i.e., beam effect presented in figure 6.7). Differences with the base cases in terms of the maximum tensile strains in the asphalt concrete layer and the maximum compressive stress in the unbound aggregate base are negligible. The maximum compressive stress in the subgrade decreases as a result of the increase in the cement-treated base thickness.

6.5. Discussion – Preliminary Design Guidelines

The principal failure mechanisms in conventional flexible pavements are (1) fatigue failure of the asphalt concrete layer determined by the maximum imposed tensile strain ε_{AC}, (2) rutting of the unbound aggregate base associated to the maximum compressive stress σ_{UAB}, and (3) rutting of the subgrade due to the maximum compressive stress σ_{SG}. In addition, the tensile strain in the cement-treated base ε_{CTB} can lead to the failure of the CTB and the diminished performance of inverted base pavement structures. These observations allow us to compare the performance of multiple pavement structures in terms of the critical pavement response parameters ε_{AC}, σ_{UAB}, and σ_{SG}. Here, we explore the implications of the parametric study results on the design of inverted base pavement structures.

6.5.1. Fatigue Failure Design

The repetitive bending action under traffic loading causes the initiation of micro-cracks in areas subjected to tensile strains. The propagation, coalescence, and re-bonding of micro-cracks in the damage-zone control the growth and healing of cracks which in

turn determine the fatigue life of bounded layers (Kim 2008). In general, pavement structures with lower maximum tensile strain in the cemented layers can sustain a larger number of load cycles before failure.

Results from the parametric study show that lower maximum tensile strains in the asphalt concrete layer are attained by increasing the thickness of the asphalt concrete layer t_{AC}, reducing the thickness of the unbound aggregate base t_{UAB}, increasing the stiffness of the unbound aggregate base, or increasing the stiffness of the asphalt concrete mix. Note that simulations assume an equivalent continuum representation; however, as the unbound aggregate layer becomes thinner the continuum assumption no longer holds. Additionally, construction difficulties are expected for unbound aggregate bases thinner than 0.10m (Lewis 2009).

The maximum tensile strain in the cement-treated base is reduced by increasing the thickness of the asphalt concrete layer t_{AC}, the thickness of the unbound aggregate base t_{UAB}, or the thickness of the cement-treated layer itself t_{CTB}, as well as by increasing the asphalt concrete stiffness. Note that, decreasing the unbound aggregate base layer thickness increases the fatigue life of the asphalt concrete layer but decreases the fatigue life of the cement-treated base.

6.5.2. Rutting Failure Design

Rutting failure manifests itself through surface depressions in the wheel path. The plastic deformations are typically the result of densification experienced by the unbound aggregate layer under service traffic load triggered by inadequate compaction.

Rutting failure is associated to the maximum compressive stress in the unbound aggregate layers. Thus, pavement structures that exhibit lower maximum compressive

stress in the unbound aggregate layers can accommodate a larger number of loading cycles before failure. A lower value of the maximum compressive stress in the unbound aggregate base is obtained by increasing the thickness of the asphalt concrete layer or increasing the thickness of the unbound aggregate base.

The cement-treated layer in an inverted base pavement acts as stiff slab that reduces the maximum stress on the subgrade and its impact on surface rutting.

6.5.3. Shear Softening

The simulation results presented in figures 6.2 and 6.3 show that a linear elastic model with the minimum stiffness expected in the unbound aggregate base yields lower tensile strains in the asphalt concrete layer than the non-linear elastic unbound aggregate base model. The non-linear model can capture the evolution in stiffness as a function of the state of stress. An increase in the mean stress p produces a gain in stiffness; however, an increase in the shear stress relative to failure q/q_f leads to softening. In order to explore the effect of shear softening we vary the k_4-exponent (see table 6.1) between 4 and 32. The results presented in figure 6.8 show that the k_4-exponent has a strong effect in the predicted maximum tensile strain in the asphalt concrete layer. The effect is magnified in inverted pavement structures with thick unbound aggregate and thin asphalt concrete layers. These results highlight the importance of proper characterization of shear softening.

6.5.4. Cost Analysis – Equivalent Conventional Sections

Inverted base pavement structures must be cost effective in addition to having a satisfactory structural performance. Materials and construction costs increase with the thickness of every layer, specially the asphalt concrete layer. Clearly, while the fatigue

and rutting resistance of the pavement structure are improved by a thicker asphalt layer, the associated increase in cost limits the thickness of the asphalt layer.

Typical conventional flexible pavement structures for three types of traffic demands are extracted from the guide for mechanistic empirical design of new and rehabilitated pavement structures (ERES 2004). The first road type (C1) is a typical primary or secondary arterial route required to satisfy a traffic demand of 750000 trucks/buses, and consists of an asphalt concrete layer t_{AC} = 0.14m and an unbound aggregate base t_{UAB} = 0.30m. The second road (C2) is a typical primary or secondary collector or county road with a traffic demand of 250000 trucks/buses and it is designed with an asphalt concrete layer t_{AC} = 0.10m and an unbound aggregate base t_{UAB} = 0.25m. The third road (C3) is a typical local street or county road with a traffic demand of 50000 trucks/buses designed with an asphalt concrete layer t_{AC} = 0.05m and an unbound aggregate base t_{UAB} = 0.20m. These three structures are modeled using the domain size, mesh, loads, constitutive models, and material parameters used in the simulations of inverted base pavements in the parametric studies reported in section 6.4.1.

The critical pavement response parameters considered to compare pavement performance are the maximum tensile strain in the asphalt concrete layer ε_{AC} and the maximum compressive stress in the subgrade σ_{SG} (figure 6.9). The conventional flexible pavement structures are compared to two inverted base pavement structures. The first (IP1) consists of a t_{AC} = 0.05m asphalt concrete layer, a t_{UAB} = 0.25m unbound aggregate base, and a t_{CTB} = 0.15m cement-treated base. The second (IP2) has a t_{AC} = 0.05m asphalt concrete layer, a t_{UAB} = 0.10m unbound aggregate base, and a t_{CTB} = 0.15m cement-treated base.

The simulation results show that the inverted base pavement structures offer superior structural performance against both subgrade rutting and asphalt fatigue. IP1 offers a structural performance sufficient to accommodate the demand from primary or secondary arterial routes and is overdesigned for typical primary or secondary collectors, local streets, and county roads. IP2 exceeds the required structural capacity of the three typical road types studied both in rutting and fatigue.

The cost per layer in the bid for the LaGrange inverted base pavement project was: US \$390/m^3 for the asphalt concrete, US \$60/m^3 for the unbound aggregate base, and US \$130/m^3 for the cement-treated base. Using these values we can estimate the cost per kilometer of road based on the layer thicknesses used in the simulations: C1=263,000\$/km, C2=198,000\$/km, C3=116,000\$/km, IP1=200,000\$/km, and IP2=167,000\$/km. These results show that the inverted base pavement structure IP2 outperforms the three typical road conditions both in rutting and fatigue and can lead to 40% in initial cost savings over the flexible pavement design for typical primary or secondary arterial routes.

6.5.5. Analysis Limitations

The long term behavior of lightly cemented aggregates exhibits three distinctive stages: (1) pre-cracked phase, (2) the onset of fatigue cracking, and (3) advanced crushing (Theyse et al. 1996). During the pre-cracked phase, the layer behaves as a slab with horizontal plane dimensions larger than the layer thickness. The elastic modulus during this stage corresponds to that measured immediately after construction of the pavement structure. At the onset of fatigue cracking, the initial elastic modulus reduces rapidly as the layer is brakes down into large blocks. Finally, the layer reduces to an

equivalent granular layer in the advanced crushing state, with a marked non-linear stress-dependent behavior. The evolution in mechanical behavior of the cemented aggregate influences the response of the entire inverted pavement structure. The structural performance reported in this chapter reflects the properties of the as-built structure and does not consider its evolution in time under traffic. Deterioration of the pavement structural capacity is expected in both inverted and conventional flexible pavement structures. However the magnitude of the deterioration and its implications in serviceability must be assessed through appropriate distress prediction models which are not considered in our analysis.

The use of thin asphalt concrete layers can lead to the development of new failure mechanisms such as shear along the periphery of the loaded area. Such failure mechanisms need to be explored in more detail before attempting to extrapolate simulation results presented earlier to asphalt concrete layers thinner that t_{AC} = 0.05m. Similarly, the use of thin unbound aggregate layers should be studied in more detail to understand the implications of discrete behavior and potential constructability and serviceability issues.

6.6. Conclusions

The selection of parameters for the unbound aggregate base has a pronounced effect on the predicted mechanical response of inverted base pavement structures. As evidenced by the observed differences in the predicted critical performance parameters obtained from linear elastic and non-linear elastic material models.

The stiffness of the asphalt concrete layer has a strong influence on the predicted maximum tensile strain in the asphalt concrete layer and the cement-treated base, and the maximum compressive stress in the unbound aggregate base.

An increase in the thickness of the asphalt concrete layer leads to higher fatigue resistance in the asphalt concrete layer, and the cement-treated base. Thicker asphalt layers also reduce the magnitude of the maximum compressive stress in the unbound aggregate base, which is associated to rutting. However, a comparison between the mechanical performance of typical conventional flexible pavements and inverted base pavement structures show that thin asphalt layers offer sufficient structural capacity in inverted pavement structures.

The fatigue life of the asphalt concrete layer is inversely proportional to the thickness of the unbound aggregate layer.

The maximum tensile strain in the cement-treated base can be reduced by increasing the asphalt concrete layer thickness, increasing the unbound aggregate base thickness, and/or increasing the cement-treated base thickness.

Accurate characterization of shear softening of unbound aggregates is very important in the analysis of inverted base pavements. The selection of k_4-exponent has a strong effect on the prediction of the maximum tensile strain in the asphalt concrete layer.

Competing mechanical demands for the various layer thicknesses must be considered together with cost per layer. In this context inverted pavements emerge as technically adequate and economically advantageous structures.

Results show that an inverted base pavement structure can exceed the required structural capacity of three typical road types studied both in rutting and fatigue while

saving up to 40% in the initial cost over the flexible pavement design for typical primary or secondary arterial routes.

Table 6.1 Material models and parameters used

Study	Asphalt concrete	Unbound aggregate base	Cement-treated base	Subgrade
Base case	Linear elastic E=4140MPa v= 0.35	Non-linear elastic: k_1 = 200MPa ; k_2 = 0.2; k_3 = 0.9; k_4 = 4; v= 0.3	Linear elastic E= 13800MPa v= 0.25	Linear elastic E= 100MPa v= 0.2
Minimum-stiffness	Linear elastic E=4140MPa v= 0.35	Linear elastic: E=230MPa v= 0.3	Linear elastic E= 13800MPa v= 0.25	Linear elastic E= 100MPa v= 0.2
Maximum-stiffness	Linear elastic E=4140MPa v= 0.35	Linear elastic: E=500MPa v= 0.3	Linear elastic E= 13800MPa v= 0.25	Linear elastic E= 100MPa v= 0.2
Hot-asphalt	Linear elastic E=2070MPa v= 0.35	Non-linear elastic: k_1 = 200MPa ; k_2 = 0.2; k_3 = 0.9; k_4 = 4; v= 0.3	Linear elastic E= 13800MPa v= 0.25	Linear elastic E= 100MPa v= 0.2
Cold-asphalt	Linear elastic E=12400MPa v= 0.35	Non-linear elastic: k_1 = 200MPa ; k_2 = 0.2; k_3 = 0.9; k_4 = 4; v= 0.3	Linear elastic E= 13800MPa v= 0.25	Linear elastic E= 100MPa v= 0.2
Thick cement-treated base	Linear elastic E=4140MPa v= 0.35	Non-linear elastic: k_1 = 200MPa ; k_2 = 0.2; k_3 = 0.9; k_4 = 4; v= 0.3	Linear elastic E= 13800MPa v= 0.25	Linear elastic E= 100MPa v= 0.2

$$E_R = k_1\left(\frac{p}{p_0}\right)^{k_2}\left[1-k_3\left(\frac{q}{q_f}\right)^{k_4}\right]$$

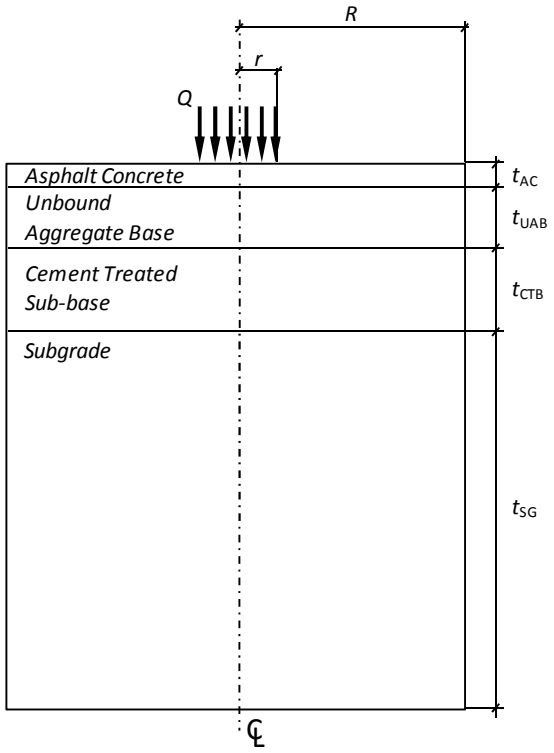

Figure 6.1 Inverted base pavement geometry

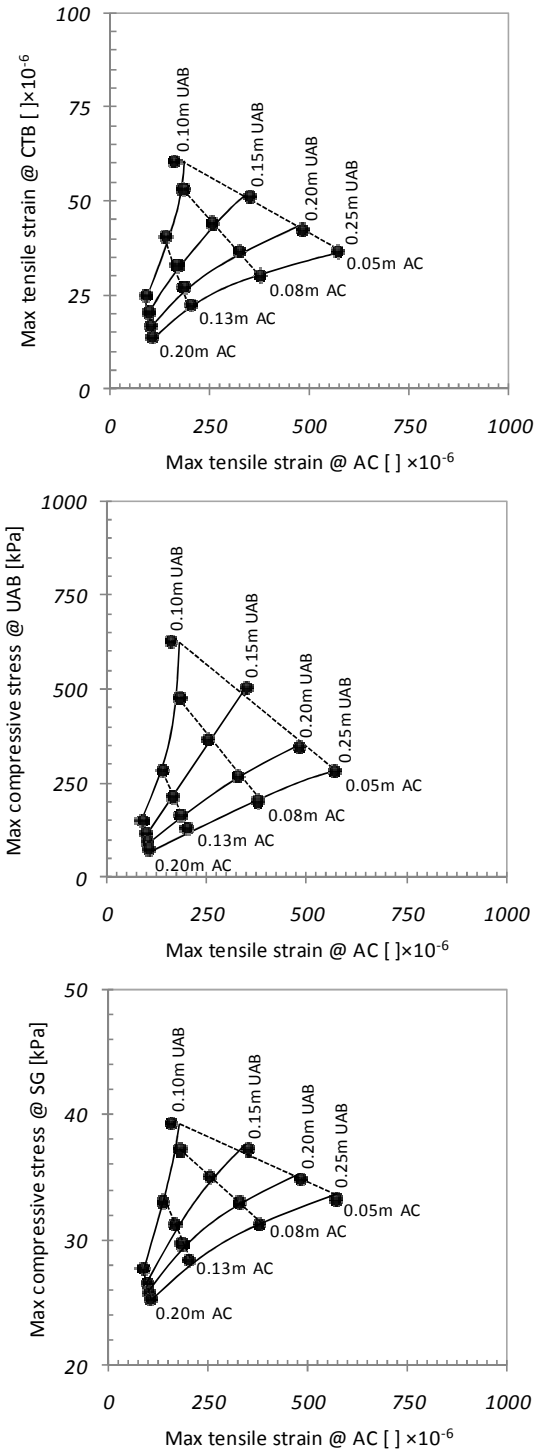

Figure 6.2 The effect of asphalt concrete thickness t_{AC} and unbound aggregate base thickness t_{UAB} (asphalt and unbound aggregate layer thickness - base cases). Markers show simulated AC/UAB thickness combinations.

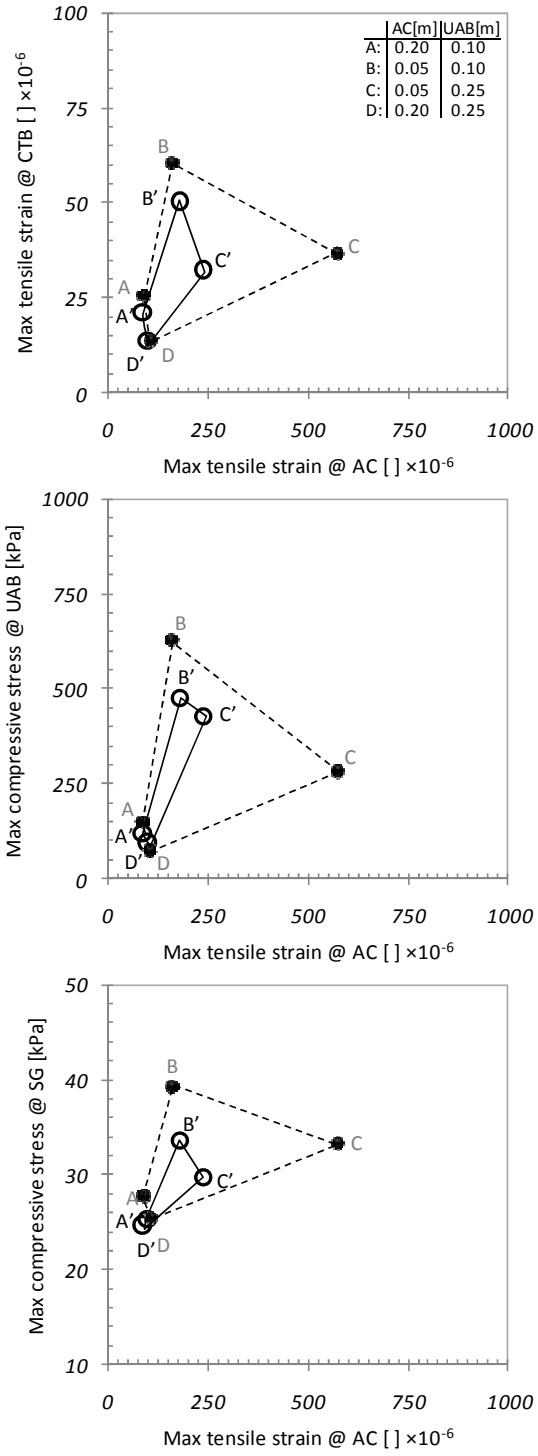

Figure 6.3 The effect of unloaded linear elastic stiffness assumption (unbound aggregate base quasi-linear response: minimum stiffness case). Markers show simulated AC/UAB thickness combinations and dashed lines show base cases results for comparison.

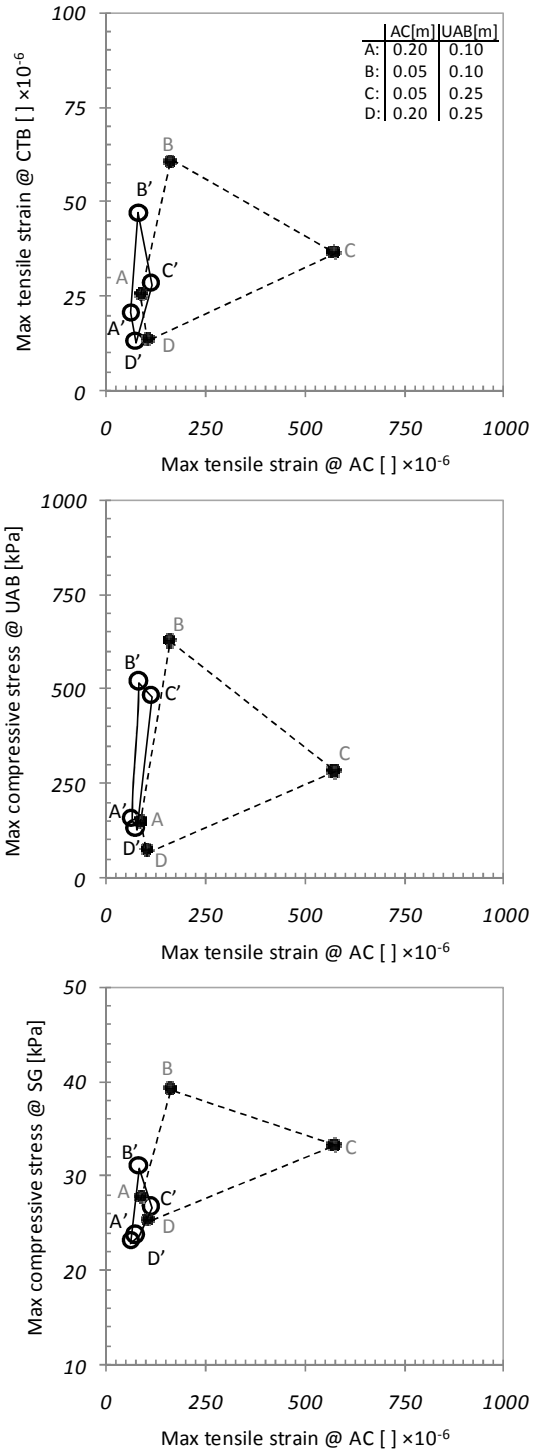

Figure 6.4 The effect of loaded linear elastic stiffness assumption (unbound aggregate base quasi-linear response: maximum stiffness case). Markers show simulated AC/UAB thickness combinations and dashed lines show base cases results for comparison.

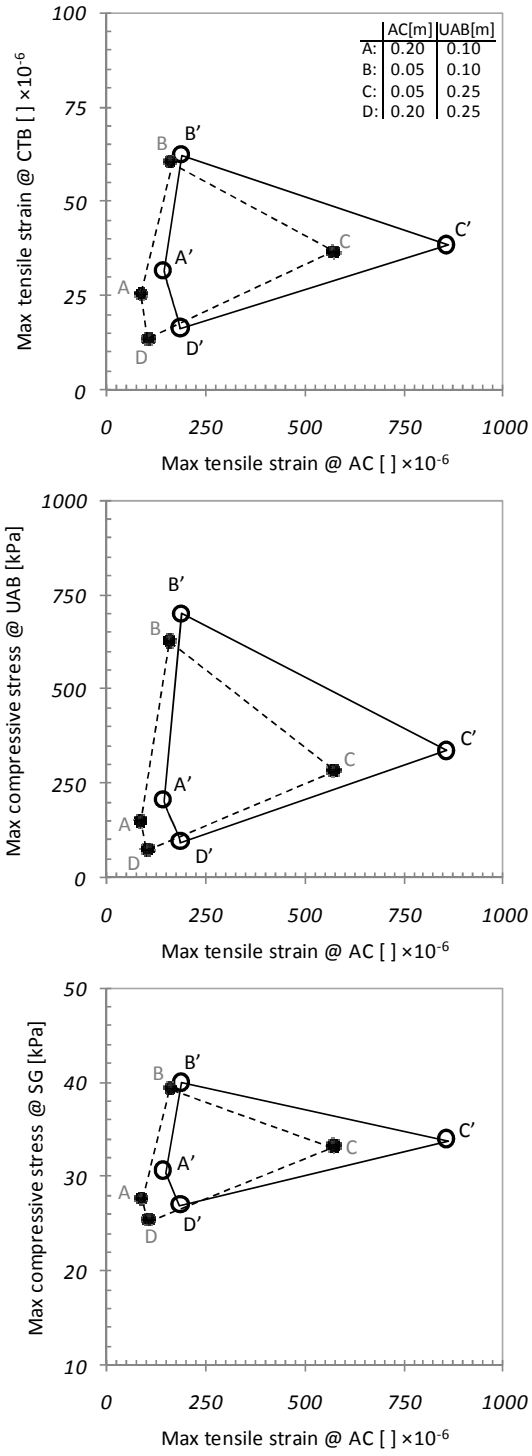

Figure 6.5 The effect of lower asphalt concrete stiffness (soft "hot" asphalt case). Markers show simulated AC/UAB thickness combinations and dashed lines show base cases results for comparison.

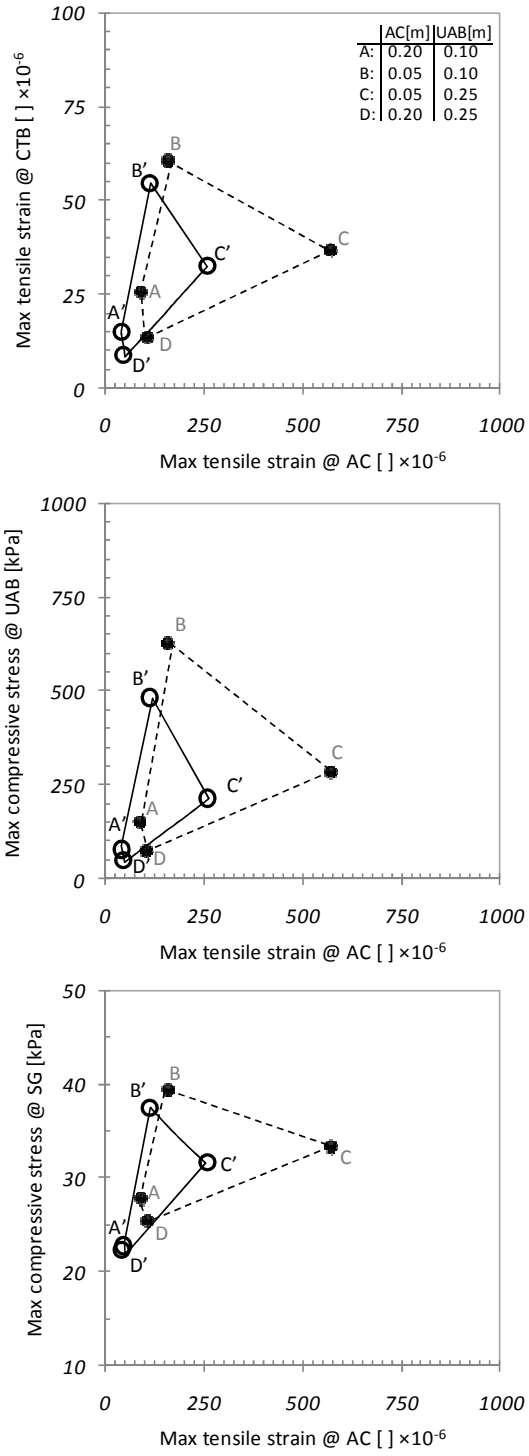

Figure 6.6 The effect of higher asphalt concrete stiffness (stiff "cold" asphalt case). Markers show simulated AC/UAB thickness combinations and dashed lines show base cases results for comparison.

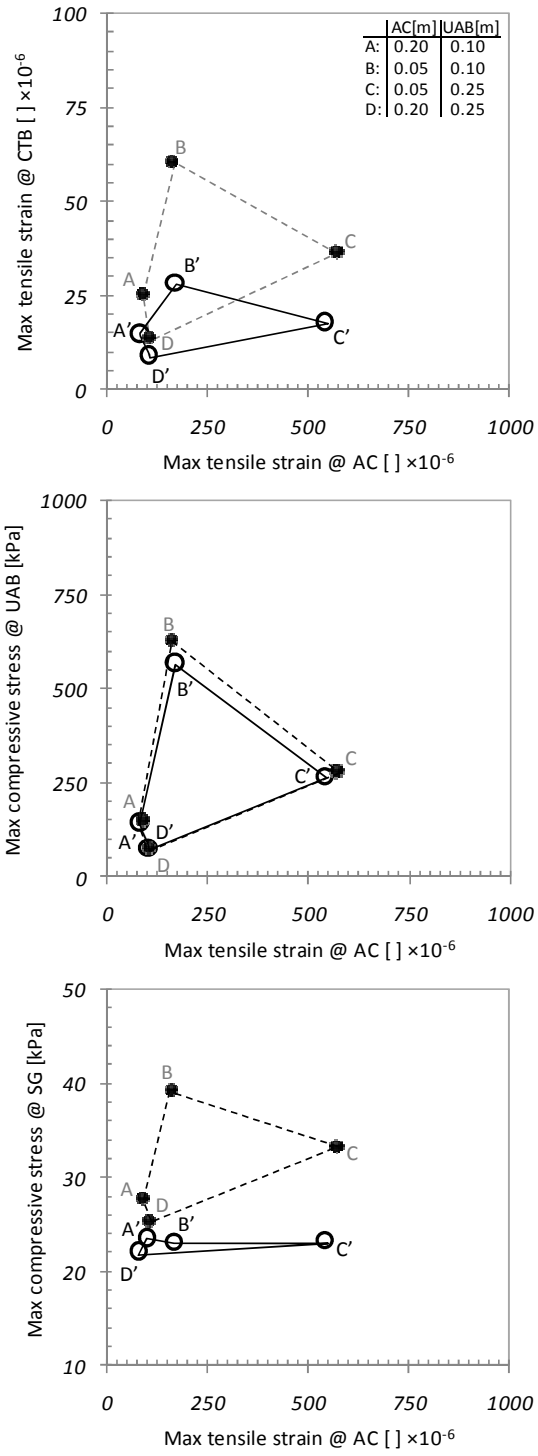

Figure 6.7 The effect of thicker cement-treated base (thick cement-treated sub-base case). Markers show simulated AC/UAB thickness combinations and dashed lines show base cases results for comparison.

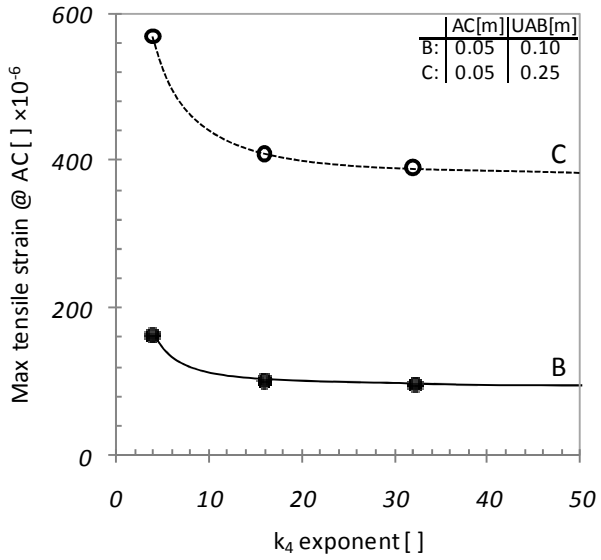

Figure 6.8 Effect of the shear softening term on the predicted maximum tensile strains in the asphalt concrete layer.

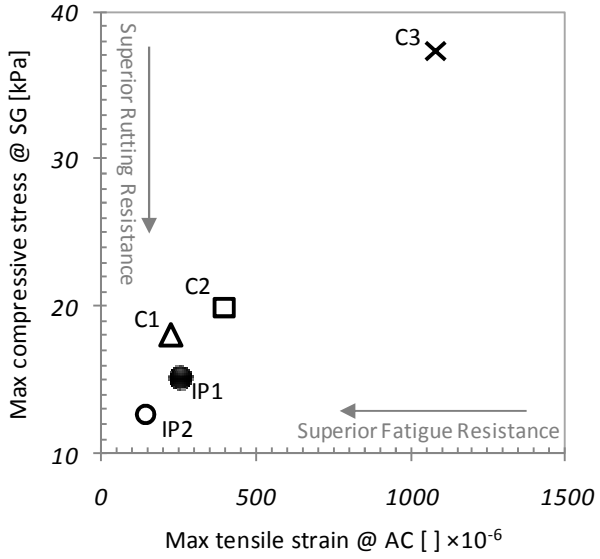

Figure 6.9 Comparison of critical pavement response parameters for three typical conventional flexible pavement structures (C1, C2, and C3) and two inverted base pavement structures (IP1 and IP2).

CHAPTER 7

CONCLUSIONS AND RECOMMENDATIONS FOR FURTHER WORK

This research was conducted to advance the understanding of inverted base pavements and to develop preliminary guidelines for their mechanistic design. Results highlight the critical role of the non-linear unbound aggregate behavior. Thus, new laboratory and field characterization methods were developed to facilitate the inversion of material parameters relevant to the state of stress and boundary conditions expected in inverted pavements. The main conclusions and recommendations for further work follow.

7.1. Conclusions

The key findings obtained from this study are:

- Construction equipment, procedures and quality control protocols used in the construction of conventional pavements can also be used to build inverted pavement structures. The off-site mixing, transport, spreading, and compaction of the cement treated mix resulted in a homogeneously compacted base. The 7-day cured cement-treated aggregate base can withstand the compaction of the overlaying layers without fracturing.
- The stress-dependent stiffness of unbound aggregate layers determines the performance of inverted base pavement structures. Therefore, an accurate characterization of the stiffness-stress response is critical for inverted pavement simulation and design. Available laboratory protocols must be modified to reproduce

the in-situ stress levels imposed on unbound aggregate bases in inverted pavements. Similarly, available in-situ measurements fail to gather sufficient information to extract the constitutive parameters required to appropriately model the stress-dependent stiffness of unbound aggregate bases.

- The unbound aggregate layer in an inverted pavement structure is confined between the stiff asphalt concrete layer and the cement treated base. The highest load condition under the wheel resembles a zero-lateral-strain loading configuration. Thus, a laboratory K_o test was prototyped for the laboratory characterization of the stiffness-stress response of unbound aggregate materials based on the concept of stiffness tomography using P-waves.
- Laboratory P-wave velocity measurements in the vertical and horizontal directions collapse onto a unique trend for a single set of parameters.
- The concept of P-wave stiffness tomography was also applied in-situ to characterize the as-built unbound aggregate base. The test has been successfully used to measure the in-situ stiffness-stress response of an existing inverted pavement structure.
- Material models reported in the literature developed using existing laboratory test protocols may under-predict the in-situ stress-dependent stiffness of the unbound aggregate base. Stiffness-stress parameters recovered using P-wave propagation in sediments under zero-lateral-strain loading yield better predictions of in-situ performance.
- Basic concepts in information theory, a comprehensive review of the resilient behavior of unbound aggregates, and physical understanding of granular materials guided the selection of a robust numerical model capable of reproducing the non-

linear resilient response of unbound aggregate layers under loading. A physically constrained optimization approach must be used to invert for the constitutive model parameters. The method is based on the analysis of error surfaces within physically acceptable ranges of each parameter.

- The selection of parameters for the unbound aggregate base has a pronounced effect on the predicted mechanical response of inverted base pavement structures. As evidenced by the observed differences in the predicted critical performance parameters obtained from linear elastic and non-linear elastic material models.
- Accurate characterization of shear softening of unbound aggregates is very important in the analysis of inverted base pavements. The selection of k_4-exponent has a strong effect on the prediction of the maximum tensile strain in the asphalt concrete layer.
- The choice of domain size and boundary conditions in numerical models of inverted base pavements affects the prediction of the maximum compressive stress on the subgrade and the maximum tensile strain in the cement treated base. Mechanical performance predictions based on large domain sizes *(R/r* >20) prevent boundary effects but overestimate the fatigue resistance of the cement treated base and the asphalt concrete layer.
- The characteristic stiffness profile in inverted pavements leads to the absence of tensile stresses in the unbound aggregate base regardless of the material model assigned to the unbound aggregate base (i.e., linear or non-linear). However, critical design parameters derived from linear elastic analyses differ considerably from predictions base on non-linear elasto-plastic analyses and may not yield conservative results.

- Simulation results show that the maximum vertical compressive stress in the subgrade of an inverted pavement is lower than the predicted value for a conventional flexible pavement section with similar fatigue resistance.
- The as-built unbound aggregate base in an inverted base pavement and a conventional flexible pavement may exhibit different stiffness-stress resilient response as a result of construction differences related to the underlying layer.
- The stiffness of the asphalt concrete layer has a strong influence on the predicted maximum tensile strain in the asphalt concrete layer and the cement-treated base, and the maximum compressive stress in the unbound aggregate base.
- An increase in the thickness of the asphalt concrete layer leads to higher fatigue resistance in the asphalt concrete layer, and the cement-treated base. Thicker asphalt layers also reduce the magnitude of the maximum compressive stress in the unbound aggregate base, which is associated to rutting. However, a comparison between the mechanical performance of typical conventional flexible pavements and inverted base pavement structures show that thin asphalt layers offer sufficient structural capacity in inverted pavement structures.
- The fatigue life of the asphalt concrete layer is inversely proportional to the thickness of the unbound aggregate layer.
- The maximum tensile strain in the cement-treated base can be reduced by increasing the asphalt concrete layer thickness, increasing the unbound aggregate base thickness, and/or increasing the cement-treated base thickness.

- Competing mechanical demands for the various layer thicknesses must be considered together with cost per layer. In this context inverted pavements emerge as technically adequate and economically advantageous structures.
- Results show that an inverted base pavement structure can exceed the required structural capacity of three typical road types studied both in rutting and fatigue while saving up to 40% in the initial cost over the flexible pavement design for typical primary or secondary arterial routes.

7.2. Recommendations for Future Work

7.2.1. Long Term Behavior of the Cement-Treated Base

The long-term behavior of cemented-treated bases evolves from a pre-cracked phase, through the onset of fatigue cracking, towards an advanced crushing stage. The elastic properties of the cement-treated base are greatly affected by the progressive deterioration of the layer which in turn affects the response of the entire inverted pavement structure. The structural performance reported in this study reflects the properties of the as-built structure and does not consider its evolution in time. Further work is required to characterize the long-term response of the cement-treated base and to incorporate its evolution in the numerical analysis of inverted base pavement structures.

7.2.2. Emergent Failure Modes and Discrete Element Model

The use of thin asphalt concrete layers can lead to the development of new failure mechanisms, such as shear fatigue along the periphery of the loaded area. Alternative failure mechanisms need to be explored in more detail before attempting to extrapolate

the simulation results to asphalt concrete layers thinner that 0.05m. Similarly, the use of thin unbound aggregate layers should be studied in more detail to understand the implications of discrete aggregate dominated behavior, potential construction difficulties, and serviceability issues. The use of unbound aggregate base materials with maximum particle-size larger than 0.025m in thin unbound aggregate layers requires different numerical tools such as the discrete element method.

7.2.3. Interface Behavior

Future numerical developments should introduce interlayer shear behavior. Shear induced by tire break and acceleration may cause sliding at the interface between the asphalt layer and the unbound aggregate.

REFERENCES

Abbas, A. R., A. T. Papagiannakis and E. A. Masad (2004). "Linear and Nonlinear Viscoelastic Analysis of the Microstructure of Asphalt Concretes." Journal of Materials in Civil Engineering 16(2): 133-139.

Adu-Osei, A. (2000). Characterization of Unbound Granular Layers in Flexible Pavements. Civil Engineering. College Station, TX, Texas A&M University. PhD: 236.

Adu-Osei, A., D. N. Little and R. L. Lytton (2001a). "Cross-Anisotropic Characterization of Unbound Granular Materials." Transportation Research Record.(1757): 82-91.

Adu-Osei, A., D. N. Little and R. L. Lytton (2001b). Structural Characteristics of Unbound Aggregate Bases to Meet AASHTO 2002 Design Requirements. Arlington, VA, Aggregates Foundation for Technology, Research, and Education.

Ahlvin, R. G., W. J. Turnbull, J. P. Sale and A. A. Maxwell (1971). Multiple-Wheel Heavy Gear Load Pavement Tests. Vicksburg, Mississippi, U.S. Army Corps of Engineers. I: 216.

Allen, J. J. and M. R. Thompson (1974). "Resilient Response of Granular Materials Subjected to Time Dependent Lateral Stresses." Transportation Research Record.(510): 173-182.

Andrei, D. (1999). Development of a Harmonized Test Protocol for the Resilient Modulus of Unbound Materials Used in Pavement Design. Department of Civil and Environmental Engineering. College Park, Maryland, University of Maryland. M.S.

Balbo, J. T. (1997). High Quality Cement Treated Crushed Stones for Concrete Pavement Bases. 6th Purdue Conference on Concrete Pavement. Indianapolis.

Barker, W. R., W. N. Brabston and F. C. Townsend (1973). An Investigation of the Structural Properties of Stabilized Layers in Flexible Pavement Systems. Vicksburg, Mississippi, U.S. Army Corps of Engineers. 165.

Barksdale, R. D. (1984). "Performance of Crushed-Stone Base Courses." Transportation Research Record.(954): 78-87.

Barksdale, R. D., S. F. Brown and F. Chan (1989). Potential Benefits of Geosynthetics in Flexible Pavements - Supplement. Washington D.C., NCHRP: 268.

Barksdale, R. D. and S. Y. Itani (1989). "Influence of Aggregate Shape on Base Behavior." Transportation Research Record.(1227): 173-182.

Beatty, T. L., D. C. Jackson, D. A. Dawood, R. A. Ford, J. S. Moulthrop, G. D. Taylor, F. L. Danchetz, D. A. Blanck, J. M. Fay, D. S. Keough, L. M. Rodriguez, M. D. Voth and Z. L. Webb (2002). Pavement Preservation Technology in France, South Africa, and Australia. Alexandria, VA, Office of International Programs, Federal Highway Administration, U.S. Department of Transportation, and the American Association of State Highway and Transportation Officials 56.

Brown, S. F. and J. W. Pappin (1981). "Analysis of Pavements with Granular Bases." Transportation Research Record.(810): 17-23.

Brown, S. F. and J. W. Pappin (1985). "Modeling of Granular Materials in Pavements." Transportation Research Record.(1022): 45-51.

Brown, S. F. and P. S. Pell (1967). An Experimental Investigation of the Stresses, Strains and Deflections in a Layered Pavement Structure Subjected to Dynamic Loads. 2nd International Conference on the Structural Design of Asphalt Pavements, Ann Arbor, Michigan.

Brunton, J. M. and J. R. De Almeida (1992). "Modeling Material Nonlinearity in a Pavement Backcalculation Procedure." Transportation Research Record.(1377): 99-106.

Chen, D.-H., M. Zaman, J. Laguros and A. Soltani (1995). "Assessment of Computer Programs for Analysis of Flexible Pavement Structure." Transportation Research Record.(1482): 123-133.

Cho, G.-C., J. Dodds and J. C. Santamarina (2006). "Particle Shape Effects on Packing Density, Stiffness, and Strength: Natural and Crushed Sands." Journal of Geotechnical and Geoenvironmental Engineering 132(5): 591-602.

Cho, Y.-H., B. McCullough and J. Weissmann (1996). "Considerations on Finite-Element Method Application in Pavement Structural Analysis." Transportation Research Record.(1539): 96-101.

Christensen, B. J., R. T. Coverdale, R. A. Olson, S. J. Ford, E. J. Garboczi, H. M. Jennings and T. O. Mason (1994). "Impedance Spectroscopy of Hydrating Cement-Eased Materials - Measurement, Interpretation, and Application." Journal of the American Ceramic Society 77(11): 2789-2804.

Crockford, W. W., L. J. Bendana, W. S. Yang, S. K. Rhee and S. P. Senadheera (1990). Modeling Stress and Strain States in Pavement Structures Incorporating Thick Granular Layers. College Station, TX, The Texas Transportation Institute: 57-71.

Dawson, A. R., N. H. Thom and J. L. Paute (1996). “Mechanical Characteristics of Unbound Granular Materials as a Function of Condition.” Flexible Pavements, Proc Eur. Symp. Euroflex 1993, Rotterdam, The Netherlands, Balkema.

Elliott, R. P. and D. Lourdesnathan (1989). "Improved Characterization Model for Granular Bases." Transportation Research Record.(1227): 128-133.

ERES (2004). Guide for Mechanistic-Empirical Design of New and Rehabilitated Pavement Structures : Final Report. Washington, D.C., National Cooperative Highway Research Program, Transportation Research Board, National Research Council.

Fam, M. A. and J. C. Santamarina (1996). "Study of Clay-Cement Slurries with Mechanical and Electromagnetic Waves." Journal of Geotechnical Engineering 122(5): 365-373.

FHWA Federal Highway Administration (2009, 01-11-08). "Highway Statistic Series." Retrieved 07-22-09, 2009, from http://www.fhwa.dot.gov/policy/ohim/hs06/htm/hm20.htm.

George, K. P. and W. Uddin (2000). Subgrade Characterization for Highway Pavement Design. Jackson, MS, Mississippi Department of Transportation Research Division: 245.

Grau, R. W. (1973). Evaluation of Structural Layers in Flexible Pavement. Vicksburg, Mississippi, U.S. Army Corps of Engineers: 138.

Hardin, B. O. and G. E. Blandford (1989). "Elasticity of Particulate Materials." Journal of Geotechnical Engineering 115(6): 788-805.

Harichandran, R. S., M.-S. Yeh and G. Y. Baladi (1990). "Mich-Pave: A Nonlinear Finite Element Program for the Analysis of Flexible Pavements." Transportation Research Record.(1286): 123-131.

Hicks, R. G. (1970). Factors Influencing the Resilient Properties of Granular Materials. Institute of Transportation and Traffic Engineering. Berkeley, California, University of California PhD: 502.

Hicks, R. G. and C. L. Monismith (1971). "Factors Influencing the Resilient Response of Granular Materials." Highway Research Record.(345): 15-31.

Hjelmstad, K. D. and E. Taciroglu (2000). "Analysis and Implementation of Resilient Modulus Models for Granular Solids." Journal of Engineering Mechanics 126(8): 821-830.

Horne, D., G. Belancio, S. A. Carradine, S. Gaj, J. Hallin, N. Jackson, C. Jordan, D. Lucas and R. Zink (1997). South African Pavement and Other Highway Technologies and Practices, Federal Highway Administration U.S. Department of Transportation: 84.

Huurman, M. (1996). "Development of Traffic Induced Permanent Strain in Concrete Block Pavements." Heron 41(1): 29-52.

Johnson, T. C., R. L. Berg and A. DiMillio (1986). "Frost Action Predictive Techniques: An Overview of Research Results." Transportation Research Record.(1089): 147-161.

Jooste, F. J. and L. Sampson (2005). The Economic Benefits of Hvs Development Work on G1 Base Pavement. Lynn East, Department of Public Transport, Roads and Works Gauteng Provincial Government.

Jorenby, B. N. and R. G. Hicks (1986). "Base Course Contamination Limits." Transportation Research Record.(1095): 86-101.

Kim, M. (2007). “Three-Dimensional Finite Element Analysis of Flexible Pavements Considering Nonlinear Pavement Foundation Behavior.” Civil Engineering. Urbana, Illinois, University of Illinois at Urbana-Champaign. Ph.D.: 234.

Kim, M., E. Tutumluer and J. Kwon (2009). "Nonlinear Pavement Foundation Modeling for Three-Dimensional Finite-Element Analysis of Flexible Pavements." International Journal of Geomechanics 9(5): 195-208.

Kim, S.-H., D. N. Little and E. Masad (2005). “Simple Methods to Estimate Inherent and Stress-Induced Anisotropy of Aggregate Base.” Transportation Research Record.(1913): 24-31.

Kim, S. H. (2004). Determination of Aggregate Physical Properties and Its Effect on Cross-Anisotropic Behavior of Unbound Aggregate Materials Civil Engineering. College Station, TX, Texas A&M University. PhD: 223.

Kim, Y. R. (2008). Modeling of Asphalt Concrete. New York; London, McGraw-Hill Professional.

Kim, Y. R., S. Underwood, G. R. Chehab, J. S. Daniel, H. J. Lee and T. Y. Yun (2008). Vepcd Modeling of Asphalt Concrete with Growing Damage. Modeling of Asphalt Concrete. Y. R. Kim. New York; London, McGraw-Hill Professional.

Kolisoja, P. (1997). Resilient Deformation Characteristics of Granular Materials. Tampere, Finland, Tampere University of Technology. PhD.

Konrad, J.-M. (2006). "The Use of Tangent Stiffness to Characterize the Resilient Response of Unbound Crushed Aggregates." Canadian geotechnical journal 43(11): 1117-1130.

Kopperman, S. E., K. H. Stokoe and D. P. Knox (1982). Effect of State of Stress on Velocity of Low Amplitude Compression Waves Propagating Along Principal Stress Directions in Dry Sand. Austin, Civil Engineering Department, University of Texas.

Lekarp, F., U. Isacsson and A. Dawson (2000). "State of the Art. I: Resilient Response of Unbound Aggregates." Journal of Transportation Engineering 126(1): 66-75.

Lewis, D. E. (2009). Inverted Pavement Loading Data - Lafarge Quarry at Morgan County. Atlanta, GA.

Lytton, R. L. (1995). Foundations and Pavements on Unsaturated Soils. 1st Foundations and Pavements on Unsaturated Soils, Paris.

McCarter, W. J. (1996). "Monitoring the Influence of Water and Ionic Ingress on Cover-Zone Concrete Subjected to Repeated Absorption." Cement Concrete and Aggregates 18(1): 55-63.

McCarter, W. J., H. Ezirim and M. Emerson (1996). "Properties of Concrete in the Cover Zone: Water Penetration, Sorptivity and Ionic Ingress." Magazine of Concrete Research 48(176): 149-156.

Monfore, G. E. (1968). "Electrical Resistivity of Concrete." Journal of the PCA Research and Development Laboratories 10(2): 35-&.

Monismith, C. L., H. B. Seed, F. G. Mitry and C. K. Chan (1967). Prediction of Pavement Deflections from Laboratory Tests. 2nd International Conference on the Structural Design of Asphalt Pavements, Ann Arbor, Michigan.

Morgan, J. R. (1966). The Response of Granular Materials to Repeated Loading. 3rd Australian Road Research Board Conference Sydney.

Nataatmadja, A. (1992). Resilient Modulus of Granular Materials under Repeated Loading. 7th International Conference on Asphalt Pavements, Nottingham University, U.K.

Nataatmadja, A. and A. K. Parkin (1989). "Characterization of Granular Materials for Pavements." Canadian Geotechnical Journal 26(4): 725-730.

Nazarian, S., M. Baker and K. Crain (1995). "Use of Seismic Pavement Analyzer in Pavement Evaluation." Transportation Research Record.(1505): 1-8.

Oldecop, L. A. and E. E. Alonso (2003). "Suction Effects on Rockfill Compressibility." Geotechnique 53(2): 289–292.

Park, S.-W. and R. L. Lytton (2004). "Effect of Stress-Dependent Modulus and Poisson's Ratio on Structural Responses in Thin Asphalt Pavements." Journal of Transportation Engineering 130(3): 387-394.

Pennington, D. S., D. F. T. Nash and M. L. Lings (1997). "Anisotropy of Shear Stiffness in Gault Clay." Geotechnique 47(3): 391-398.

Pezo, R. F. (1993). A General Method of Reporting Resilient Modulus Tests of Soils - a Pavement Engineer's Point of View. 72nd Annual Meeting of the Transportation Research Board.

Puppala, A. J. (2008). Estimating Stiffness of Subgrade and Unbound Materials for Pavement Design - a Synthesis of Highway Practice. Washington, D.C., Transportation Research Board: 129.

Raad, L. and J. L. Figueroa (1980). "Load Response of Transportation Support Systems." American Society of Civil Engineers, Transportation Engineering Journal 106(Compendex): 111-128.

Rada, G. and M. W. Witczak (1981). "Comprehensive Evaluation of Laboratory Resilient Moduli Results for Granular Material." Transportation Research Record.(810): 23-33.

Rahim, A. M. and K. P. George (2005). "Models to Estimate Subgrade Resilient Modulus for Pavement Design." International Journal of Pavement Engineering 6(2): 89-96.

Rajabipour, F. and J. Weiss (2007). "Electrical Conductivity of Drying Cement Paste." Materials and Structures 40(10): 1143-1160.

Rasoulian, M., B. Becnel and G. Keel (2000). "Stone Interlayer Pavement Design." Transportation Research Record.(1709): 60-68.

Rasoulian, M., H. Titi, M. Martinez, B. Becnel and G. Keel (2001). Long Term Performance of Stone Interlayer Pavement. Baton Rouge LA, Louisiana Transportation Research Center: 29.

Revil, A. and P. W. J. Glover (1997). "Theory of Ionic-Surface Electrical Conduction in Porous Media." Physical Review B 55(3): 1757.

Richardson, D. N. and S. M. Lusher (2008). Determination of Creep Compliance and Tensile Strength of Hot Mix Asphalt for Wearing Courses in Missouri Jefferson City, MO: 75.

Robinson, R. G. (1974). Measurement of the Elastic Properties of Granular Materials Using a Resonance Method, Transport and Road Research Laboratory Supplementary Report No. 111UC.

Rust, F. C., J. P. Mahoney and J. B. Sorenson (1998). An International View of Pavement Engineering. Bearing Capacity of Roads and Airfields. Trondheim, Norway.

Santamarina, J. C. and D. Fratta (2005). Discrete Signals and Inverse Problems : An Introduction for Engineers and Scientists. Hoboken, NJ, Wiley.

Santamarina, J. C., K. A. Klein and M. A. Fam (2001). Soils and Waves. New York, John Wiley & Sons, Ltd.

Santamarina, J. C., K. A. Klein, Y. H. Wang and E. Prencke (2002). "Specific Surface: Determination and Relevance." Canadian Geotechnical Journal 39(1): 233–241.

Seed, H. B., F. G. Mitry, C. L. Monismith and C. K. Chan (1967). Prediction of Fexible Pavement Deflections from Laboratory Repeated Load Tests, National Cooperative Highway Research Program.

Shifley, L. H. and C. L. Monismith (1968). Test Road to Determine the Influence of Subgrade Characteristics on the Transient Deflections of Aphalt Concrete Pavements Berkeley, CA, Materials and Research Department Division of Highways State of California: 127.

Simulia (2007). ABAQUS Version 6.7: User Subroutines Reference Manual.

Smith, W. S. and K. Nair (1973). Development of Procedures for Characterization of Untreated Granular Base Coarse and Asphalt-Treated Base Course Materials. Washington, D.C., Federal Highway Administration: 221.

Sukumaran, B., N. Chamala, M. Willis, J. Davis, S. Jurewicz and V. Kyatham (2004). Three Dimensional Finite Element Modeling of Flexible Pavements, FAA Worldwide Airport Technology Transfer Conference, Atlantic City, New Jersey.

Terrell, R. G. (2002). Measuring Directional Stiffness in Pavement Base Material. Civil Engineering. Austin, TX, University of Texas at Austin. Master of Science in Engineering: 133.

Terrell, R. G., B. R. Cox, K. H. Stokoe Ii, J. J. Allen and D. Lewis (2003). "Field Evaluation of the Stiffness of Unbound Aggregate Base Layers in Inverted Flexible Pavements." Transportation Research Record.(1837): 50-60.

Theyse, H., M. De Beer and F. Rust (1996). "Overview of South African Mechanistic Pavement Design Method." Transportation Research Record.(1539): 6-17.

Thom, N. H. and S. F. Brown (1987). Effect of Moisture on the Structural Performance of a Crushed-Limestone Road Base. Transportation Research Record.(1121): 50-56.

Thom, N. H. and S. F. Brown (1988). "The Effect of Grading and Density on the Mechanical Properties of a Crushed Dolomitic Limestone." 14th Australian Road Research Board Conference.

Titi, H., M. Rasoulian, M. Martinez, B. Becnel and G. Keel (2003). "Long-Term Performance of Stone Interlayer Pavement." Journal of Transportation Engineering 129(2): 118-126.

Trollope, E. H., I. K. Lee and J. Morris (1962). Stresses and Deformation in Two-Layer Pavement Structures under Slow Repeated Loading. 1st Australian Road Research Board Conference.

Tutumluer, E. (1995). Predicting Behavior of Flexible Pavements with Granular Bases. School of Civil and Environmental Engineering. Atlanta, GA, Georgia Institute of Technology. PhD: 321.

Tutumluer, E. and R. D. Barksdale (1995). "Inverted Flexible Pavement Response and Performance." Transportation Research Record.(1482): 102-110.

Tutumluer, E., D. N. Little and S. H. Kim (2003). A Validated Model for Predicting Field Performance of Aggregate Base Courses. 82nd Annual Meeting of the Transportation Research Board. Washington, DC: 27.

Tutumluer, E. and U. Seyhan (2003). Charaterization of Cross-Anisotropic Aggregate Base Behavior from Stress Path Tests. Recent Advances in Material Characterization and Modeling of Pavement Systems E. Tutumluer, Y. M. Najjar and E. Masad. Reston, Virginia, American Society of Civil Engineers. 123: 18-34.

Tutumluer, E. and M. R. Thompson (1997). "Anisotropic Modelling of Granular Bases in Flexible Pavements." Transportation Research Record.(1577): 18-26.

Underwood, S., A. Heidari, M. Guddati and Y. Kim (2005). "Experimental Investigation of Anisotropy in Asphalt Concrete." Transportation Research Record.(1929): 238-247.

Uzan, J. (1985). "Characterization of Granular Material." Transportation Research Record.(1022) 52-59.

Uzan, J. (2005). "Viscoelastic--Viscoplastic Model with Damage for Asphalt Concrete." Journal of Materials in Civil Engineering 17(5): 528-534.

Van Niekerk, A. A., A. A. A. Molenaar and L. J. M. Houben (2002). “Effect of Material Quality and Compaction on the Mechanical Behaviour of Base Course Materials and Pavement Performance.” 6th International Conference on Bearing Capacity of Roads, Railways and Airfields, Lisbon, Portugal.

Vuong, B. (1992). "Influence of Density and Moisture Content on Dynamic Stress-Strain Behaviour of a Low Plasticity Crushed Rock." Road and Transport Research 1(2): 88-100.

Wang, K., K. J. Cable and Z. Ge (2003). “Investigation into Pavement Curing Materials, Application Techniques, and Assessment Methods.” Mid-Continent Transportation Research Symposium Ames, Iowa, Iowa State University.

Witczak, M. W. (2004). "Laboratory Determination of Resilient Modulus for Flexible Pavement Design." National Cooperative Highway Research Program Research Results Digest(285): 48.

Zaman, M., D.-H. Chen and J. Laguros (1994). "Resilient Moduli of Granular Materials." Journal of Transportation Engineering 120(6): 967-988.